UNIVERSITY OF SOUTHAMPTON

# Metasurfaces: Coherent Control of Light in Two Dimensions

by

Maria Papaioannou

A thesis submitted for the
degree of Doctor of Philosophy

in the
Faculty of Physical Sciences and Engineering
Optoelectronics Research Centre

January 2018

UNIVERSITY OF SOUTHAMPTON

ABSTRACT

Faculty of Physical Sciences and Engineering

OPTOELECTRONICS RESEARCH CENTRE

Doctor of Philosophy

# METASURFACES: COHERENT CONTROL OF LIGHT IN TWO DIMENSIONS

by Maria Papaioannou

In this thesis, control of light with light without nonlinearity in plasmonic metasurfaces is extended from zero to two spatial dimensions enabling a range of novel applications. In particular:

- For the first time, **all-optical logical operations between two-dimensional light distributions** are demonstrated based on coherent absorption and coherent transparency of a plasmonic metasurface. XOR, XNOR, AND and OR operations are performed between coherent optical signals of 785 nm wavelength and applied to separate spatially multiplexed optical channels.

- **Qualitative and quantitative pattern recognition and image analysis** are performed for the first time based on the coherent interaction of wavefronts on an absorbing plasmonic metasurface within a hardware-based system at 790 nm wavelength.

- **All-optical control of focusing of light** is realized by superimposing Fresnel zone patterns on an absorbing metasurface using coherent light for the first time. Switching of focal intensity, depth, diameter and distance and effective replacement of a lens by an aperture are accomplished by optical phase modulation at 790 nm wavelength without moving parts.

- The first **imaging interferometer** for spatially resolved control of absorption of light with light in plasmonic metasurfaces was built for this thesis. Using coherent light, two spatial intensity distributions (inputs) are imaged on a free-standing gold metasurface and their interaction (output) is monitored by an imaging detector. Measurements show that the system's spatial resolution is about 900 nm.

Two-dimensional control of light with light on plasmonic metasurfaces is in principle compatible with quantum regime intensities and 100 THz bandwidth. Therefore, the presented scheme could provide efficient all-optical wavefront manipulation, computing, imaging and focusing components for future coherent photonic devices and networks.

Dedicated to my grandmother Eleni.

*"Nevertheless - who knows -*
*the point at which someone hopelessly resists,*
*may be where human history begins,*
*and as we say, the human beauty..."*
Yannis Ritsos

# Table of Contents

**Abstract** iii

**Table of Contents** vii

**List of Figures** ix

**List of Tables** xi

**Declaration of Authorship** xiii

**Acknowledgements** xv

**Abbreviations** xvii

**1 Introduction** 1
- 1.1 Coherent control of light-matter interactions . . . 1
- 1.2 Coherent control of light with light in metasurfaces . . . 4
  - 1.2.1 Metamaterials and metasurfaces . . . 4
  - 1.2.2 Coherent control of the expression of metasurface functionalities 8
- 1.3 Motivation for coherent control of light with light in two dimensions with metasurfaces . . . 11
- 1.4 Outline of this thesis . . . 12

**2 Theory and methods of coherent control of light with light** 15
- 2.1 Mathematical description of coherent control of the expression of thin film absorption . . . 15
- 2.2 Numerical modelling of coherent perfect absorption . . . 20
  - 2.2.1 A metasurface for coherent perfect absorption . . . 21
  - 2.2.2 Metasurface response under spatially varying illumination . . . 30
- 2.3 Fabrication of metamaterials and masks . . . 37
  - 2.3.1 Metasurface nanofabrication and characterization . . . 37
  - 2.3.2 Mask fabrication . . . 40
- 2.4 Optical imaging interferometer for two-dimensional coherent control of absorption of light . . . 44
- 2.5 Summary . . . 47

**3 All-optical logic and demultiplexing based on coherent perfect absorption** **49**
3.1 Introduction . . . 49
3.2 All-optical logical operations in two dimensions . . . 51
3.3 Towards multichannel logic for telecommunications . . . 58
3.3.1 Logical operations between intensity- and phase-modulated channels 59
3.3.2 Logic and demultiplexing with spatially multiplexed channels . . 61
3.4 Summary . . . 67

**4 All-optical image processing and pattern recognition** **69**
4.1 Introduction . . . 69
4.2 All-optical image processing . . . 71
4.3 Set operations between images . . . 73
4.4 Pattern recognition . . . 75
4.5 Image analysis . . . 79
4.6 Study on the spatial resolution of the experimental optical imaging interferometer . . . 82
4.7 Summary . . . 90

**5 All-optical dynamic focusing of light with a plasmonic metasurface** **93**
5.1 Introduction . . . 93
5.2 Theoretical description of all-optical dynamic focusing based on two-dimensional coherent control of light with light . . . 95
5.3 Demonstration of all-optical dynamic focusing functionalities . . . 98
5.3.1 All-optical setup for coherent control of focusing properties . . . 98
5.3.2 Control of focal intensity . . . 100
5.3.3 Control of focal depth and diameter . . . 103
5.3.4 Theoretical description of continuous control over focal properties 106
5.3.5 Effective switching between a lens and a diffracting aperture . . 107
5.3.6 Theoretical description of all-optical tuning of the focal distance 112
5.4 Summary . . . 116

**6 Conclusions** **119**
6.1 Summary . . . 119
6.2 Outlook . . . 121

**A Ideal thin absorber** **125**

**B Publications and awards** **127**
B.1 Journal publications . . . 127
B.2 Conference contributions . . . 127
B.3 Awards . . . 129

**Bibliography** **131**

# List of Figures


1.1 Spatiotemporal coherent control with pulse shaping. . . . . 2
1.2 Interferometric coherent control of light with light. . . . . 3
1.3 Split ring resonator metamaterial. . . . . 5
1.4 Three-dimensional and two-dimensional metamaterials. . . . . 6
1.5 Reconfigurable metadevices. . . . . 8
1.6 Thin film translation between anti-nodes and nodes of a standing wave. 9
1.7 Coherent control of the expression of metasurface functionalities. . . . . 10

2.1 Four-port device representation of coherent control of thin films. . . . . 18
2.2 Asymmetrically Split Ring metamaterial. . . . . 22
2.3 Computational model for the study of Asymmetrically Split Ring samples. 24
2.4 Free-standing Asymmetrically Split Ring gold sample design. . . . . 25
2.5 Asymmetrically Split Ring gold sample design on silica substrate. . . . . 27
2.6 Asymmetrically Split Ring gold sample design on $Si_3N_4$ substrate. . . . 28
2.7 Comparison of coherent control responses for Asymmetrically split ring samples on different substrates . . . . . 29
2.8 Spatially addressable coherent control concept. . . . . 30
2.9 Computational model for spatially addressable coherent control. . . . . 32
2.10 Asymmetrically Split Ring array under uniform single beam excitation. 33
2.11 Asymmetrically Split Ring array under spatially varying excitation: Excitation transition boundary line parallel to the array's symmetry axis. . 35
2.12 Asymmetrically Split Ring array under spatially varying excitation: Excitation transition boundary line perpendicular to the array's symmetry axis. . . . . 36
2.13 Fabrication process for free-standing gold Asymmetrically Split Ring arrays. 37
2.14 Fabricated free-standing gold Asymmetrically Split Ring metasurface. . 40
2.15 Binary intensity masks fabricated by mechanical milling. . . . . 41
2.16 Binary intensity masks fabricated with photo-lithography. . . . . 42
2.17 Optical setup for two-dimensional coherent control. . . . . 44
2.18 Metasurface sample mounting assembly. . . . . 45

3.1 Interaction of coherent beams on lossless and lossy beamsplitters. . . . . 52
3.2 Two-dimensional control of absorption of light with light. . . . . 53
3.3 Binary intensity mask designs for all-optical coherent Boolean logic demonstrations. . . . . 56
3.4 Two-dimensional all-optical coherent logical operations. . . . . 57
3.5 Binary intensity masks for spatially multiplexed channel signals. . . . . 62
3.6 Coherent logic with the central channel. . . . . 64

3.7 All-optical multichannel logic operations. . . . . 65

4.1 Coherent image processing. . . . . 72
4.2 All-optical metasurface-based pattern recognition concept. . . . . 75
4.3 Photolithography-fabricated binary masks for pattern recognition. . . . 76
4.4 Qualitative all-optical pattern recognition. . . . . 78
4.5 Quantitative all-optical pattern recognition. . . . . 79
4.6 Photolithography-fabricated binary Arctic and Greenland ice extent evolution masks for the period of 1982 to 2012. . . . . 80
4.7 Image analysis of Arctic and Greenland ice extent evolution from 1982 to 2012. . . . . 81
4.8 Comparison of theoretical and experimental image analysis of Arctic and Greenland ice extent evolution from 1982 to 2012. . . . . 83
4.9 Photolithography-fabricated masks for measuring spatial resolution. . . 85
4.10 Spatial resolution of the system for metasurface illumination by a single beam. . . . . 87
4.11 Spatial resolution of the system for simultaneous metasurface illumination by two coherent beams. . . . . 89

5.1 Dynamic optical focusing with a metamaterial absorber. . . . . 94
5.2 Fresnel zone plate designs for dynamic control of optical focusing. . . . . 97
5.3 Coherent control of optical focusing. . . . . 99
5.4 Simulation results for controlling focal intensity. . . . . 101
5.5 Experimental results for controlling focal intensity. . . . . 102
5.6 Focal depth and diameter for identical Fresnel zone plate patterns. . . . 103
5.7 Simulation results for controlling focal depth and diameter. . . . . 104
5.8 Experimental results for controlling focal depth and diameter. . . . . 105
5.9 Focal depth and diameter for different Fresnel zone plate patterns. . . . 106
5.10 Simulated phase-dependence of focal properties. . . . . 107
5.11 Simulation results for turning a focusing zone plate into a diffracting aperture. . . . . 108
5.12 Experimental results for turning a focusing zone plate into a diffracting aperture. . . . . 109
5.13 Focal depth and diameter for inverted zone plate patterns. . . . . 110
5.14 From a focusing zone plate to a diffracting aperture or darkness. . . . . 111
5.15 Fresnel zone plate designs for control of the focal distance. . . . . 112
5.16 Simulation results for controlling the focal distance. . . . . 113
5.17 Focal depth and diameter for different zone plate patterns targeting tuning of the focal distance. . . . . 114

A.1 Field symmetry after scattering by a thin film . . . . . 125

# List of Tables


3.1 Logical operation A AND B. . . . . 54
3.2 Logical operation A XOR B. . . . . 54
3.3 Logical operation A OR B. . . . . 55
3.4 Logical operations between equal intensity phase-modulated data streams A and B. . . . . 60
3.5 Logical operations between in-phase intensity-modulated data streams. . 61

4.1 Set operations between images A and B based on photodetector measurements. . . . . 74

5.1 Fresnel zone plate design radii. . . . . 98
5.2 Beam B Fresnel zone plate design radii for control of the focal distance. 113

# Declaration of Authorship

I, MARIA PAPAIOANNOU, declare that this thesis titled, 'Metasurfaces: Coherent Control of Light in Two Dimensions' and the work presented in it are my own. I confirm that:

- This work was done wholly or mainly while in candidature for a research degree at this University.
- Where any part of this thesis has previously been submitted for a degree or any other qualification at this University or any other institution, this has been clearly stated.
- Where I have consulted the published work of others, this is always clearly attributed.
- Where I have quoted from the work of others, the source is always given. With the exception of such quotations, this thesis is entirely my own work.
- I have acknowledged all main sources of help.
- Where the thesis is based on work done by myself jointly with others, I have made clear exactly what was done by others and what I have contributed myself.

Signed:

Date:

# Acknowledgements

I would like to thank my supervisors Prof. Nikolay I. Zheludev and Dr. Eric Plum for their guidance, help and our useful scientific discussions through the course of my PhD. I would also like to thank Dr. Edward T. F. Rogers for his valuable advice on experimental procedures and Dr. João Valente for the free-standing gold metasurface sample fabrication. I am also grateful to Dr. Traianos Yioultsis who believed in me and inspired me to pursue a research career. My scientific achievements and the completion of my PhD thesis would not have been possible without the love and encouragement of my family and especially Anna, Simos, Konstantina and Ilias. I would like to address a special "thank you" to my friends Eleni, Eirini and Maria for their unconditional love and support even when we were miles apart and to Zoi Bakrinioti, Dr. Maria Kourasi, Nikos Aspiotis, Dr. Evangelos Atmatzakis, Dr. Ioannis Katis, Dr. João Valente, Dr. Papagiotis Botsinis, Stan Vassilev, Dr. Ioannis Zeimpekis and Dr. Grigoris Zisis, my friends in Southampton with whom I shared all the bright and dark moments of the extraordinary PhD life. Finally, I would like to especially thank my loving partner, Nikos, for holding my hand and keeping me going.

# Abbreviations

| | |
|---|---|
| **2D** | Two-Dimensional |
| **CPA** | Coherent Perfect Absorption |
| **3D** | Three-Dimensional |
| **ASR** | Asymmetrically Split Ring |
| **FEM** | Finite Element Method |
| **FWHM** | Full Width at Half Maximum |
| **FOM** | Figure Of Merit |
| **NA** | Numerical Aperture |
| **FIB** | Focused Ion Beam |
| **RIE** | Reactive Ion Etching |
| **SEM** | Scanning Electron Microscope |
| **CW** | Continuous Wave |
| **VLC** | Variable Liquid Crystal |
| **HWP** | Half Wave Plate |
| **CCD** | Charge Coupled Device |
| **LED** | Light Emitting Diode |

# Chapter 1

# Introduction

## 1.1 Coherent control of light-matter interactions

Current information technology largely relies on optical transfer and electronic processing of data and therefore requires repeated electro-optical signal conversion. All-optical signal processing could circumvent the complexity, speed and power shortcomings of electro-optical signal conversion and deliver major breakthroughs for photonics technology. To that end, ultrafast and energy efficient control of light-matter interactions is the fundamental requirement for controlling a light beam with another beam of light. Initially, the concept of coherent control of light-matter interactions was introduced as a way to manipulate molecular systems and develop spectroscopy and microscopy techniques by the means of tailored constructive and destructive quantum-mechanical interferences that compose a desired state [1–7].

To date, several different routes have been followed to the realization of light-by-light control. Numerous approaches were based on the enhancement and exploitation of nonlinear effects and their excitation with intense laser sources [8–10]. However, the energy-demanding nature of these techniques cannot provide an answer to the ever increasing demand for energy-efficient devices and their overall performance is highly dependent on the speed of the nonlinearity involved in the system. Over the last decade, researchers have focused on the exploration of coherent light-matter interactions in media that are structured on a sub-wavelength scale as a way to overcome these deficiencies and to coherently control light in a more efficient way.

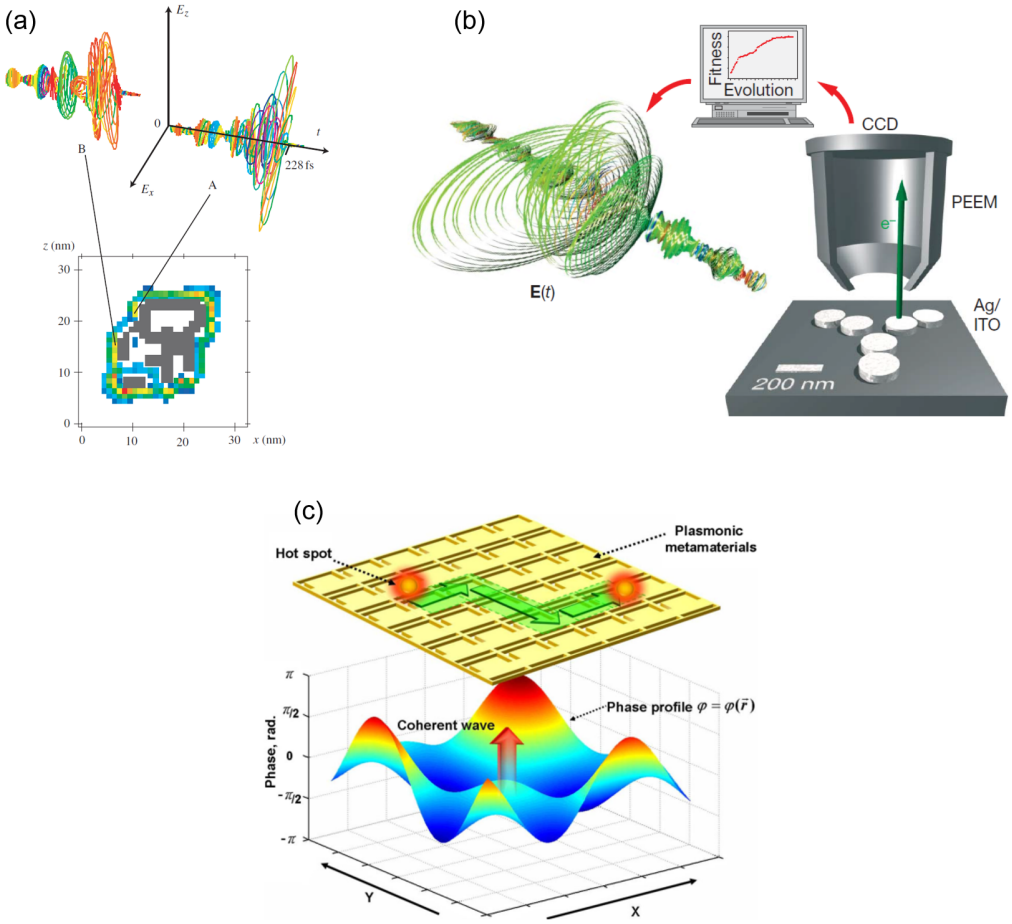


**Figure 1.1: Spatiotemporal coherent control with pulse shaping.** (**a**) Shaping of excitation waveforms in the far-field (top A and B) impose the localized field intensity map (bottom - colourscale) in a plasmonic nanosystem (bottom - gray), [11]. (**b**) Sub-wavelength dynamic localization of electromagnetic intensity on a planar nanostructure is achieved by iteratively optimized polarization shaping of ultrashort pulses, [12]. (**c**) Phase-modulated light beam profile exciting hot spot localization in a metamaterial array, [13].

Nanoplasmonics is the fastest optics platform, hence the most eligible candidate for hosting all-optical processes. However, light manipulation and focusing at the nano-scale is a persistent challenge in nanophotonics technology since conventional focusing is governed by the diffraction limit. In most cases, the establishment of the desired energy distribution at the nano-scale requires high-accuracy spatiotemporal coherent control of the external stimulus. As proposed in [11, 12, 14, 15], controllable variation of the spatio-temporal distribution of polarization and/or phase across the wavefront of a coherent incident beam creates different quantum pathways of the excitation which interfere on

the nano-scale sample plane. Usually, the spectral composition and the pulse shape of the excitation comprise the tuning parameters in this scenario, see Fig. 1.1 a and b. Similar techniques have been employed in [13, 16–18] for engineering the distribution of light hot spots along a two-dimensional (2D) array of plasmonic unit cells. In particular, tailoring the far-field spatial profile of a coherent continuous beam affects the inter-meta-molecular coherent interactions and results in precisely controllable localization of hot spots, see Fig. 1.1 c.

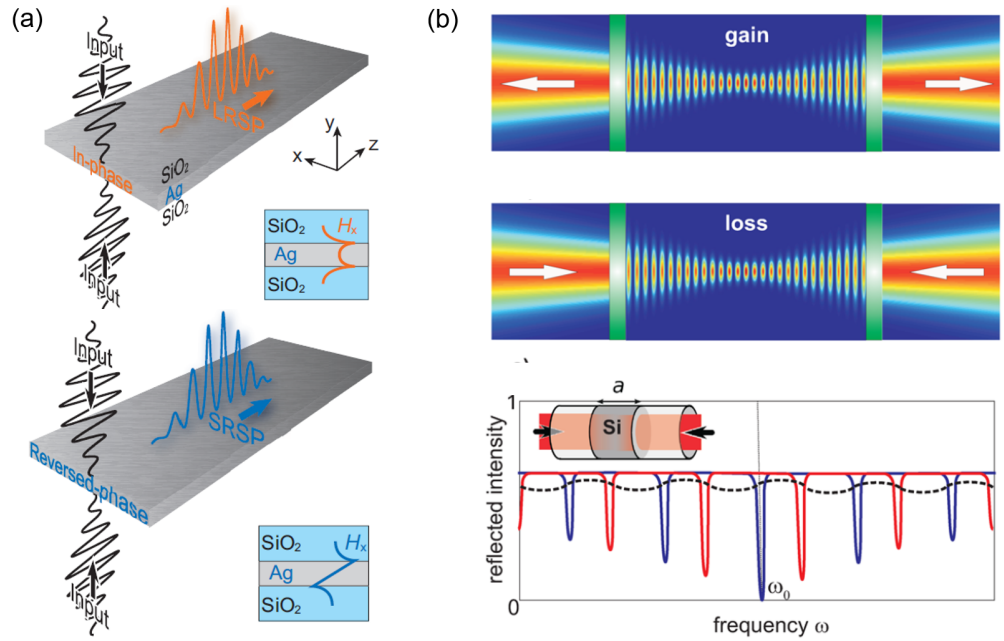


**Figure 1.2: Interferometric coherent control of light with light.** (**a**) Mode selection between long- and short-range surface plasmon polaritons depending on the relative phase difference of the incident beams, [19]. (**b**) Laser oscillator (top): a gain medium embedded in an optical cavity emits outgoing coherent waves with defined phase and spatial pattern at frequency $\omega_0$. Coherent perfect absorber (middle): when the gain medium is replaced by an absorber, incoming waves with a certain phase and spatial pattern are fully absorbed. Bottom: Typical behaviour of the total intensity reflection coefficient versus frequency in a simple two-port photonic device, comprising a slab of lossy material (like Si) of thickness $\alpha$ embedded in a fibre or waveguide (inset), excited at the two input sides. Red and blue lines show the spectral reflection curves for coherent input waves with controlled phase difference $\Delta\varphi$ ($\Delta\varphi = 0$, blue curve; $\Delta\varphi = \pi$, red curve). The dashed black line depicts the spectral reflection curve for incoherent input waves, [20].

Coherent control may also be employed in an interferometric configuration to achieve a broad range of intriguing phenomena. In recent theoretical and experimental studies, coherent counter-propagating beams have been employed to control the mode coupling

in a dielectric waveguide with plasmonic nanostructures [21] and the selectivity between long- and short-range surface plasmon modes with variable excitation efficiency [19], see Fig. 1.2 a. In the same context, Coherent Perfect Absorption (CPA), also referred to as time-reversed lasing, has been demonstrated in the configuration of two counter-propagating beams impinging on a silicon cavity, as described in Fig. 1.2 b. In particular, when the gain medium of a laser cavity is replaced by an equivalent absorbing medium and the incoming coherent waves comprise the time-reversed outgoing optical fields of a laser mode, the total input energy is perfectly absorbed, [20, 22–24]. Several groups have conducted further investigation of the CPA principle with implementations employing different absorbers across the electromagnetic spectrum like the ones presented in [25–27]. The fundamental principle adopted throughout the research explorations of this thesis lies in this area.

## 1.2 Coherent control of light with light in metasurfaces

Amongst the interferometric coherent control approaches lies the discipline of coherent control of light with light without nonlinearity via the modulation of the expression of metasurface functionalities [28]. Coherent control of light with light in metasurfaces brings the flexibility of nonlinearity-free coherent control together with the diverse capabilities of metamaterial structures and is the underpinning principle of all theoretical studies and experimental demonstrations in this thesis.

### 1.2.1 Metamaterials and metasurfaces

For almost two decades in the limelight, the field of metamaterials has made significant contributions to the evolution of microwave and photonics technology. Metamaterials are best defined as artificial media with unusual properties resulting from structuring on a size-scale smaller than the wavelength of the external stimulus [29]. Hence, the sub-wavelength scale building blocks are scatter-free and the metamaterial structure is perceived by the impinging wave as an effectively homogeneous medium that can be macroscopically described by the effective electromagnetic parameters of permittivity and permeability. The metamaterial building block, so called meta-molecule, can be properly tailored in size, shape and constituent materials and therefore constitutes the tuning parameter which gives rise to extraordinary functionalities not readily attainable

in natural materials. Their exotic properties fuelled the inspiration for the term meta-materials which is etymologically resolved as meta-materials, where meta- (= $\mu\epsilon\tau\acute{\alpha}$) is the Greek word standing for beyond (i.e. beyond-materials).

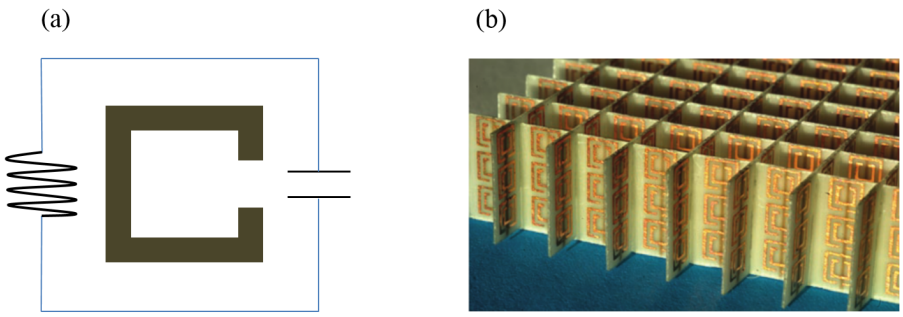


**Figure 1.3: Split ring resonator metamaterial.** (**a**) Equivalent LC circuit. (**b**) Negative index metamaterial formed by split ring resonators and wires [30].

In a more elaborate description, meta-molecules comprise sub-wavelength scale resonating unit cells, most frequently arranged in crystal-like ensembles, i.e. metamaterials. The overall performance of the resulting medium is dominated by the meta-molecule's resonator response. At microwave frequencies, the building block structure can be conceived as an equivalent LC circuit. For instance, the split ring resonator which was used to construct the first negative refractive index metamaterial [30, 31] shown in Fig. 1.3 b, is associated with an inductance (L) and a capacitance (C) corresponding to the loop and the gap part of the design, respectively. Thus, the resonant frequency is given by the formula $\omega = \frac{1}{\sqrt{LC}}$. Moreover, geometric resonances are enabled when wire components of the unit cell design have lengths equal to a multiple of $\lambda/2$, where $\lambda$ is the wavelength of light. Therefore, variations of the unit cell geometry parameters and constituent materials [32], as well as the coupling to neighbouring meta-molecules [33] are translated into tuning mechanisms for the metamaterial design. This approach holds up to near-infrared frequencies. When entering the visible part of the spectrum, induced currents are replaced by plasmons (i.e. collective oscillations of the electron density) [34], which requires more elaborate metamaterial design.

Historically, the occurrence of extraordinary medium response was predicted by Veselago in 1968 [35] under the hypothesis of a substance with simultaneous negative permeability and permittivity that results in negative refraction. However, it was not

until 1999 that the existence of such media became realistic, when Pendry et al. described an array of split ring resonators exhibiting negative permeability associated with the system's magnetic resonance [36]. A combination of split ring resonators with arrays of metallic rods that were previously proven to exhibit negative permittivity [37, 38] materialized Veselago's prediction of such a medium [39]. Such media gave rise to the field of metamaterials as we know it today and in early research attempts resulted in the demonstration of the 'perfect lens' that beats the diffraction limit [40, 41] and transformation optics metamaterials for bending light around corners [41, 42], which are undoubtedly two of the most prestigious demonstrations to date.

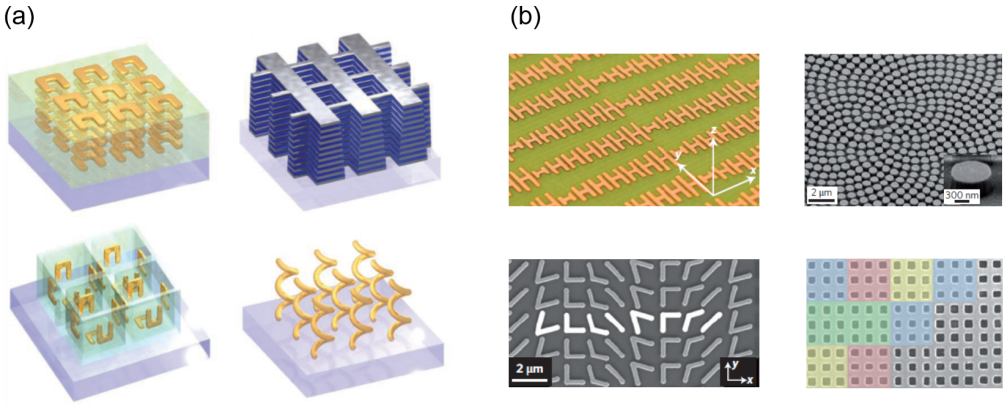


**Figure 1.4: Three-dimensional and two-dimensional metamaterials.** (**a**) Truly 3D split ring resonator (top and bottom left), fishnet (top right) and chiral (bottom right) nanostructures [43]. (**b**) Planar (2D) metamaterials: gradient metasurfaces (top and bottom left) and metasurface holograms (top and bottom right) [44].

In principle, metamaterials can be engineered to cover a vast range of applications across the electromagnetic spectrum. Following the improvement of fabrication techniques, metamaterial structure designs were properly tailored to meet the sub-wavelength size requirement at visible wavelenghts [45, 46], while taking into account the large losses of metals at optical frequencies [47–49].

Ever since, various implementations of metamaterial concepts were presented either in the form of three-dimensional (3D) bulk configurations [43] or as planar metamaterials of deep sub-wavelength thickness, also known as metasurfaces or 2D metamaterials

[44, 50], see Fig. 1.4. Chiral metamaterials have paved another way to negative refraction and led to numerous fascinating properties, such as giant optical activity and directionally asymmetric transmission [51–53]. Moreover, symmetry breaking approaches to the famous split ring resonator structure have introduced trapped-mode resonances [54] leading to extrinsic-chirality-induced optical activity [55, 56], the metamaterial analogue of electromagnetically induced transparency [57, 58] and the metamaterial version of a lasing spaser for coherent radiation generation [59]. Epsilon-near-zero metamaterials permit light to propagate through them without accumulating phase [60]. Following the expression of the generalized version of Snell's law, phase discontinuities along the interface between two media impose light bending [61, 62]. This discovery inspired the realization of gradient metasurfaces for broadband highly-efficient anomalous reflectors [63], polarization beam splitters and polarisation-independent beam-steering components [64]. Phase discontinuities on metasurfaces were also exploited to translate propagating waves to surface waves [65] as well as to create flat focusing mirrors [66], lenses [67, 68], holograms [69] and wavefront shaping platforms [70–72]. Metasurfaces have also provided the ultrathin and chip-compatible analogue of bulk metamaterials with hyperbolic dispersion [50], invisibility [73], enhanced light-matter interactions [74], perfect absorption [75] and wave-vector selectivity [76]. It should be noted that for both 3D and 2D metamaterials, the hindering parameter for efficient designs is the loss of metals at visible and telecommunications wavelengths. Several research groups have focused on searching better candidate materials for metasurface and metamaterial designs [77–80].

Despite their fascinating nature and potential, metamaterial and metasurface properties are normally static since they are usually designed to operate in a specific wavelength regime delivering a particular functionality. This limitation has given rise to the broad research area of tunable and switchable metamaterials which have led to the establishment of metadevices (i.e. metamaterial-based devices) that respond to thermal, electric, magnetic or optical control signals which induce changes in their optical properties [84]. In recent years, a range of diverse realizations of metadevices has been reported based on different types of reconfiguration mechanisms. Structural reconfiguration of the shape and/or arrangement of meta-molecules enables tunable electromagnetic responses [81, 85–90]. Hybridization of metamaterials with semiconductors [91, 92], ferroelectrics [93], graphene [94, 95], superconductors [96, 97], phase change materials [82, 98–101] or

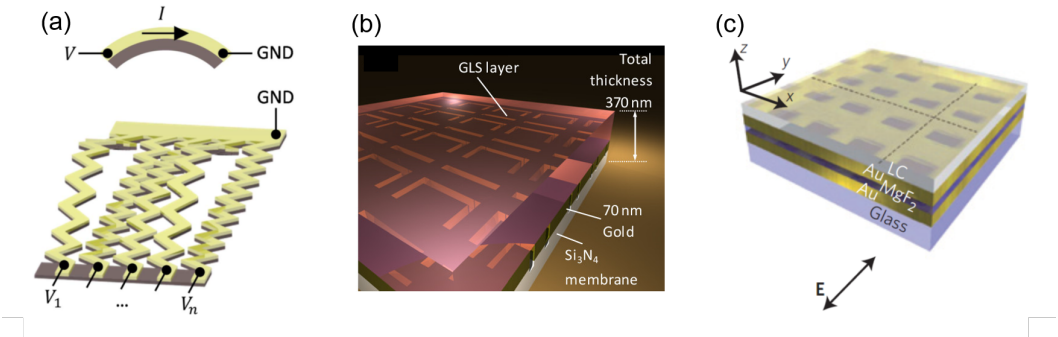


**Figure 1.5: Reconfigurable metadevices.** (**a**) Random-access electrothermal actuation of individually reconfigurable nanowires (artist's impression) [81]. (**b**) Artistic impression of a metamaterial-chalcogenide hybrid device. The metamaterial absorption resonance is spectrally tuned by electro-optical switching between amorphous and crystalline chalcogenide forms [82]. (**c**) Photonic fishnet metamaterials (artist's impression) infiltrated with nematic liquid crystal. Optical properties are tuned by an electric field [83].

liquid crystals [83, 102] reinforces dynamical tuning via induced changes in the properties of the medium accompanying the metamaterial and its interaction with the metamaterial, hence altering the metadevice functionality, see Fig. 1.5.

In the hunt of ultrafast energy-efficient and compact systems, metamaterials, metasurfaces and metadevices are amongst the candidates that could revolutionize telecommunications and photonics networks.

### 1.2.2 Coherent control of the expression of metasurface functionalities

The concept of coherent control of the expression of metasurface functionalities was born as the mechanism that merges all-optical coherent control schemes with the diverse potential of metasurfaces to provide a vast range of functionalities that can be dynamically switched with light.

The interaction of two coherent co-polarized counter-propagating waves of arbitrarily low power on a film of sub-wavelength thickness can provide ultrafast control over the sample's excitation without nonlinearity [28]. Under the condition of deep sub-wavelength thickness, a film solely interacts with the electric field of a normally incident plane wave because its interaction with the magnetic field is prohibited by the fact that in-plane magnetic dipole modes are not supported in truly planar structures. This allows control over the expression of the film's functionality from complete suppression to

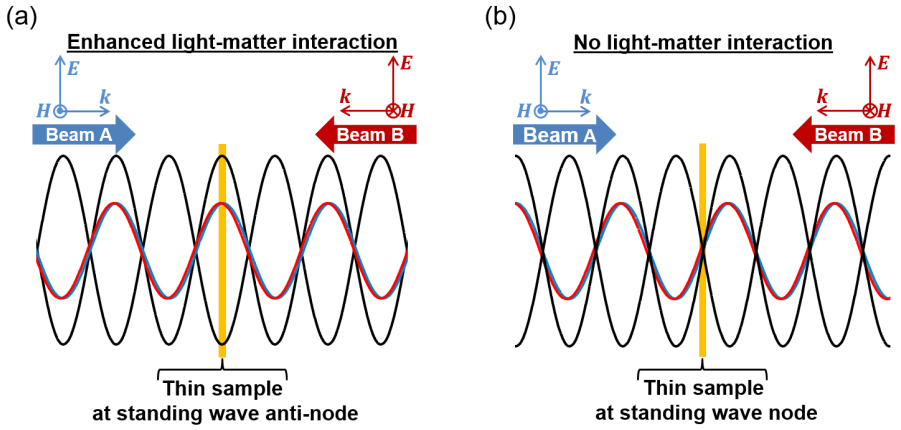


**Figure 1.6: Thin film translation between (a) anti-nodes and (b) nodes of a standing wave** that is formed by the counter-propagating beams A and B. The relative phase difference between the two beams at the thin film position is 0 in **a** and $\pi$ in **b**. In both figures the black lines represent the electric field envelope of the standing wave.

enhancement. The light-matter interaction is controlled by effective translation of the sample between electric nodes (suppressed functionality expression) and anti-nodes (enhanced functionality expression) of the standing wave formed by the counter-propagating coherent waves, see Fig. 1.6.

Light-with-light coherent control of thin films is a simple, yet rather intriguing platform that can host all sorts of functionalities and can lead to numerous applications. Since metasurfaces (i.e. planar or 2D metamaterials of deep sub-wavelength thickness that may be approximated by a single layer) have enabled the design of almost arbitrary landscapes of static optical properties, dynamic temporal and spatial control over metasurface properties has become the next big challenge. Coherent control of the expression of thin film properties, as defined here, paves the way for further exploration of metasurface functionalities based on their dynamic all-optical reconfiguration in a standing wave.

Recently, experimental and theoretical work based on this principle has successfully employed a metasurface which absorbs 50% of a travelling wave. In the coherent energy standing wave regime, where two co-polarized coherent counter-propagating beams illuminate the sample, the metasurface absorption can be modulated from 0% (*coherent perfect transparency*) to 100% (*coherent perfect absorption*) of incident light at standing wave electric field nodes and anti-nodes, respectively [27, 28, 106]. The

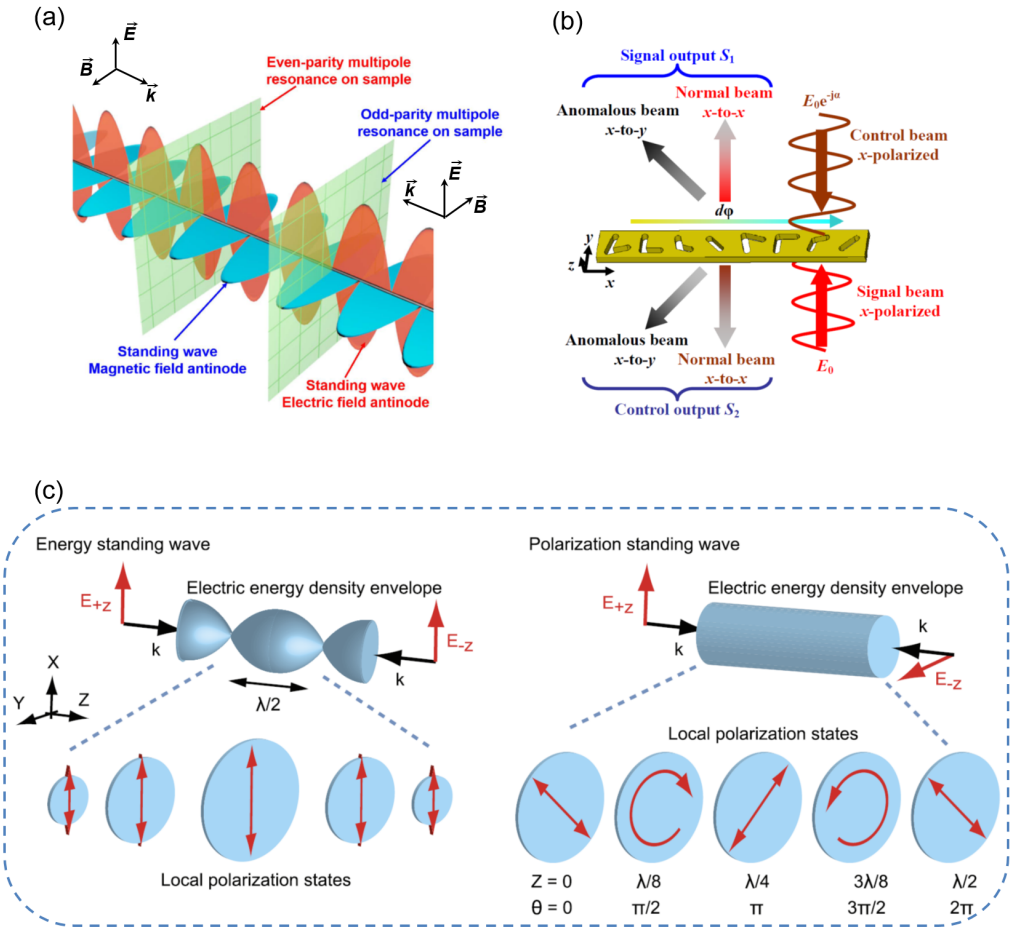


**Figure 1.7: Coherent control of the expression of metasurface functionalities.** (**a**) Coherent excitation of different resonance modes through selective coupling to even and odd parity multipoles via excitation of symmetric metamaterial modes at electric field anti-nodes and anti-symmetric modes at magnetic field anti-nodes, respectively [103]. (**b**) Schematic illustration of coherent control of a V-shaped slot antenna metasurface using coherent signal and control $x$-polarized beams with a phase difference $\alpha$ which controls the efficiency of normal and anomalous transmission [104]. (**c**) Energy (left) and polarization standing wave (right) schematics showing in each case the envelope of electric energy density and the evolution of the local polarization state. The standing waves are formed by two counter-propagating co-linearly (left) and orthogonally polarized (right) waves [105].

all-optical processing potential of this paradigm inspired further research on the energy and speed limitations of the technique. In particular, coherent control of metasurface absorption was experimentally proven to be compatible with quantum regime intensities [107] and operable with up to 100 THz modulation bandwidth [108, 109]. The femtosecond-second-scale response time of plasmonic metamaterials under the coherent control scheme is similar to the response time of ultrafast nonlinear optical processes

such as the optical Kerr effect or two photon absorption which are however associated with a decreased magnitude of nonlinearity [110]. Consequently, coherent control of metasurface absorption, which does not rely on intrinsic material nonlinearities, is an inherently ultra-fast, energy-efficient, all-optical technique. The principle underpins all theoretical and experimental demonstrations of this thesis and will by described in detail in Chapter 2.

Apart from absorption, the expression of any other metasurface functionality can be coherently controlled in the standing wave regime. Coherent excitation-selective spectroscopy exploits the separate excitation of metasurface electric and magnetic dipole resonances as well as hidden high-order photonic excitations at different standing wave positions which cannot be achieved in the travelling wave regime where different resonances are simultaneously excited [103, 111], see Fig. 1.7 a. For gradient metasurfaces where reflected and transmitted waves follow the modified Snell's law, coherent control has facilitated the control over energy distribution between normal and anomalous output beams by controlling the intensity or phase of one of the coherent input beams [104], see Fig. 1.7 b. Manifestations of optical activity and optical anisotropy [112, 113] in planar metamaterials can also be continously controlled by effectively varying the sample's position relative to the standing wave. Further possibilities are opened, if an ultrathin anisotropic metasurface is translated across a polarisation standing wave created by two counter-propagating coherent waves of orthogonal polarizations [105]. In a polarization standing wave, energy densities are constant whereas local polarization oscillates along the wave axis and absorption of an anisotropic sample depends on both its position and orientation within the polarization standing wave, see Fig. 1.7 c.

## 1.3 Motivation for coherent control of light with light in two dimensions with metasurfaces

The ever increasing demand for all-optical data processing has introduced the need for efficient control of light with light. However, the conventional way of achieving such functionality requires power consuming nonlinearities in the visible and near-infrared part of the spectrum. As described in the previous section, incorporating nano-scale thickness metamaterials into an environment of coherent light interactions allows the

modulation of light with light without nonlinearity. Thus, ultra-fast linear light-by-light modulation on absorptive plasmonic metasurfaces can be achieved with arbitrarily low intensities. This thesis focuses on exploiting this phenomenon in order to further investigate and explore the all-optical processing functionalities that can be achieved on this basis.

In an effort to take advantage of the inherent parallelism of photonics, a major goal is to illustrate the ability to excite a plasmonic metamaterial structure in a spatially addressable manner under the coherent control scheme in a proof-of-principle experiment. In particular, a spatially modulated wavefront of one beam can constructively or destructively interfere with a coherent counter-propagating beam on a metamaterial, thus resulting in a spatially distributed total enhancement or elimination of Joule losses, respectively. This expansion of coherent control of metasurface absorption from 0 to 2 spatial dimensions can provide a platform for all-optical, ultrafast and energy-efficient green solutions for parallel information and data processing in coherent future telecommunications and photonic networks.

Following a detailed theoretical study of the underpinning principle and the employed metasurface functionality, the main goal is to create an experimental platform for two-dimensional coherent control of light with light on metasurfaces. This enables proof-of-principle demonstrations of all-optical logical operations, optical channel demultiplexing, image processing, pattern recognition and dynamic focusing. As opposed to previous established solutions in each of these applications, the proposed technique is free from slow and energy-hungry nonlinearities and does not depend on expensive and computationally intense algorithms and post-processing schemes. It can therefore comprise a prime candidate solution in the hunt for ultrafast and energy efficient solutions for the next era of coherent photonic technologies.

## 1.4 Outline of this thesis

In Chapter 2, the theory and experimental methods of coherent control of metasurface absorption will be presented. In particular, a mathematical description of the approach will be provided and followed by numerical modelling methods and results for sample design as well as for metasurface behaviour under spatially varying illumination. Regarding experimental methods, the fabrication techniques used for the metasurface

and the two-dimensional profile masks will be described along with the optical imaging interferometer that was built to demonstrate two-dimensional coherent control.

Chapter 3 introduces all-optical logic based on coherent perfect absorption by demonstrating a set of all-optical logical functions in two dimensions (XOR, XNOR, AND, OR). Subsequently, the method will be translated into a metamaterial-based multichannel logic element performing logical functions between intensity- and phase-modulated channels as well as a spatial demultiplexing scheme for coherent telecommunications systems.

In Chapter 4, the all-optical computation capability of the experimental platform will be shifted towards all-optical image processing via a formalism of set operations between images which leads to the demonstration of all-optical hardware-based image processing, image and pattern recognition and analysis free from heavy computational post-processing schemes.

The diversity of potential applications of two-dimentional light-by-light coherent control will be further expanded in Chapter 5, where all-optical dynamic focusing of light will be presented. Specifically, the attainable all-optical functionalities of controlling the focal intensity, depth and diameter of a lens as well as the effective switching between a lens and a clear aperture without moving parts will be theoretically analysed and experimentally demonstrated. Additionally, continuous control over the properties of the focal spot (intensity depth and diameter) and dynamic switching of the focal distance will be theoretically presented.

Finally, in Chapter 6 the main conclusions of this work will be derived and the contributions of two-dimensional coherent control to the field of metadevices and photonics will be outlined. Lastly, future outlook, prospect and ideas for this project will also be discussed.

# Chapter 2

# Theory and methods of coherent control of light with light

The objective of this project is to evolve the research on dynamic control of the expression of metasurface functionalities within a coherent light-by-light control environment. The ambition towards this direction is to demonstrate the ability to spatially address a metasurface that has already been proven to provide for 0 - 100% absorption when coherently controlled under spatially uniform excitation. This chapter establishes the fundamental theory of coherent control of thin film absorption and presents a theoretical study on the most suitable meta-molecule design with respect to the overall coherent response of the metasurface under spatially uniform coherent illumination. Subsequently, the performance of the most suitable design is theoretically investigated under spatially addressable (non-uniform) coherent illumination. A complete description of techniques and methods for the experimental realization of two-dimensional coherent control is also presented here.

## 2.1 Mathematical description of coherent control of the expression of thin film absorption

In the configuration of Fig. 1.6 describing coherent control of a functional thin film, two co-linearly polarized coherent counter-propagating beams A and B establish a standing wave. The interaction of the thin sample with light depends on the sample's position within the standing wave. This light-matter interaction can be generally described by

the Hamiltonian in the first-order spatial dispersion approximation [114]:

$$H_{int} = \frac{1}{c}\hat{\boldsymbol{d}}\frac{\partial\vec{\boldsymbol{A}}}{\partial t} - \frac{1}{c}(\frac{d\hat{q}^{il}}{dt} - ce_{ilk}\hat{\boldsymbol{m}}^{k})\nabla_{l}\vec{\boldsymbol{A}}_{i} \tag{2.1}$$

In this equation $i, l, k$ are the Cartesian coordinates and $e_{ilk}$ the Levi-Civita permutation symbol for three dimensions. $\vec{\boldsymbol{A}}$ is the vector potential of the electromagnetic field, $\hat{\boldsymbol{d}}, \hat{\boldsymbol{q}}, \hat{\boldsymbol{m}}$ represent the electric dipole, electric quadrupole and magnetic dipole moments, respectively, $c$ is the speed of light and $t$ represents time [114]. Assuming $y$-polarized coherent counter-propagating beams A and B of frequency $\omega$ and equal amplitudes propagating along the $z$-axis, the vector-potential, the magnetic and electric field vectors of the established standing wave are given by:

$$\vec{\boldsymbol{A}} = A_{y}\hat{\boldsymbol{y}} = A_{0}(sin(kz - \omega t) - sin(kz + \omega t))\hat{\boldsymbol{y}}, \tag{2.2}$$

$$\vec{\boldsymbol{B}} = \nabla \times \vec{\boldsymbol{A}} = \frac{\partial A_{y}}{\partial z}\hat{\boldsymbol{x}} = \text{-}2kA_{0}sin(kz)sin(\omega t)\hat{\boldsymbol{x}}, \tag{2.3}$$

$$\vec{\boldsymbol{E}} = \frac{\partial\vec{\boldsymbol{A}}}{\partial t} = -\frac{\partial A_{y}}{\partial t}\hat{\boldsymbol{y}} = 2\omega A_{0}cos(kz)cos(\omega t)\hat{\boldsymbol{y}}, \tag{2.4}$$

where $A_0$ is the amplitude of the vector potential and $k$ the wave number. Substituting Eq. 2.2 to Eq. 2.1 yields

$$H_{int} = -2kA_{0}[\hat{\boldsymbol{d}}cos(kz)cos(\omega t) - (\frac{1}{c}\frac{d\hat{q}^{yz}}{dt} - \hat{\boldsymbol{m}}^{x})sin(kz)sin(\omega t)] \tag{2.5}$$

This Hamiltonian provides a detailed description of the interaction of the standing wave with the thin sample assuming negligible contribution from higher order multipoles. Specifically, for the sample positioned at standing wave electric nodes (minima of the electric field) shown in Fig. 1.6 b, where $cos(kz) = 0$, the light-matter interaction is restricted to the electric quadrupole and magnetic dipole interactions with the energy stored in the magnetic field maxima. On the contrary, at standing wave magnetic nodes (electric field anti-nodes shown in Fig. 1.6 a), where $sin(kz) = 0$, solely the electric dipole interaction is possible. Therefore, in order to perform a full analytical description of the limiting cases of Fig. 1.6, one should calculate the individual electric dipole, electric quadrupole and magnetic dipole mode contributions to the response of the sample that is to be employed in the coherent control configuration.

However, for the purposes of this thesis, only single layer samples of deep sub-wavelength thickness are considered. The in-plane electric quadrupole and magnetic dipole modes of Eq. 2.5 are not supported in truly planar structures when excited at normal incidence. Therefore, the contribution of these modes in the case of a film of non-zero, yet deep sub-wavelength thickness, is minuscule compared to the effects arising from coupling to the electric dipole excitation. So, the second term of Eq. 2.5 can be eliminated from this analysis for simplification purposes, while always keeping in mind that in the case of electric nodes, this term will be minuscule but non-zero. Consequently, the simplified Hamiltonian for samples of deep sub-wavelength thickness reads:

$$H_{int} = -2kA_0\hat{\boldsymbol{d}}cos(kz)cos(\omega t) \tag{2.6}$$

Having explored the nature of the thin film excitation, the standing wave description is derived based on the electric field of input beams A and B in Fig. 1.6. In the coherent control configuration in energy standing waves, the coherent counter-propagating input beams are co-linearly polarized and normally incident to the film (assuming $y$-polarization and employing complex conjugate notation for this description):

$$\overrightarrow{\boldsymbol{E_A}} = E_A e^{-i(\omega t - kz - \Delta\varphi)}\hat{\boldsymbol{y}} \qquad \text{and} \qquad \overrightarrow{\boldsymbol{E_B}} = E_B e^{-i(\omega t + kz)}\hat{\boldsymbol{y}} \tag{2.7}$$

where $E_A$, $E_B$ stand for the amplitude of the electric field for each beam and $\Delta\varphi$ is the relative beam phase difference which throughout this work is prescribed by varying the phase of beam A. The real-valued electric fields of beam A and B are given by the real parts of $\overrightarrow{\boldsymbol{E_A}}$ and $\overrightarrow{\boldsymbol{E_B}}$. On a certain plane across the standing wave, say $z = 0$, the time-averaged energy density stored in the electric field $\vec{\boldsymbol{E}} = \overrightarrow{\boldsymbol{E_A}} + \overrightarrow{\boldsymbol{E_B}}$ of the standing wave reads:

$$\begin{gathered}\frac{\epsilon_o}{2}\langle\vec{\boldsymbol{E}}\vec{\boldsymbol{E}}^*\rangle = \frac{\epsilon_o}{2}\langle(\overrightarrow{\boldsymbol{E_A}} + \overrightarrow{\boldsymbol{E_B}})(\overrightarrow{\boldsymbol{E_A}} + \overrightarrow{\boldsymbol{E_B}})^*\rangle = \\ \frac{\epsilon_o}{2T}Re\{\int_0^T \overrightarrow{\boldsymbol{E_A}}\overrightarrow{\boldsymbol{E_A}}^* dt + \int_0^T \overrightarrow{\boldsymbol{E_B}}\overrightarrow{\boldsymbol{E_B}}^* dt + 2\int_0^T \overrightarrow{\boldsymbol{E_A}}\overrightarrow{\boldsymbol{E_B}}^* dt)\} = \\ \frac{\epsilon_o}{2}({E_A}^2 + {E_B}^2 + 2E_A E_B cos(\Delta\varphi))\end{gathered} \tag{2.8}$$

where $\epsilon_o$ is the permittivity of free space and $T$ is the period of the oscillating field.

In order to investigate what happens across the standing wave electric nodes and anti-nodes and how the film functionality comes into play, it is instructive to consider

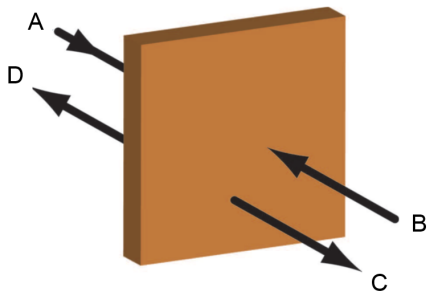


**Figure 2.1: Four-port device representation of coherent control of thin films.** A thin film (brown) is illuminated by two coherent counter-propagating beams A and B. Beams C and D are the two resulting output beams, [106, 115].

the thin film coherent control scheme as a four-port device which describes the system taking into account both excitation beams and thin film properties [106, 115].

This is illustrated in Fig. 2.1 with two input beams A and B, two output beams C and D and a thin film. Assuming no phase advance is accumulated within the film due to its vanishing thickness, it can be considered that the film scatters equally in the forward and backward direction. Additionally, assuming that the film is illuminated by an eigenpolarization, it may be described by a single complex scattering amplitude $s(\lambda)$ that is wavelength dependent. For a single incident beam, say $\overrightarrow{\boldsymbol{E_A}}$, the reflected field is given by $s(\lambda)\overrightarrow{\boldsymbol{E_A}}$ and the transmitted field is given by the superposition of scattered and incident waves $(s(\lambda)+1)\overrightarrow{\boldsymbol{E_A}}$. It is therefore evident that the output beams C and D are related to the input beams A and B via the scattering matrix expression [115]:

$$\begin{bmatrix} \overrightarrow{\boldsymbol{E_D}} \\ \overrightarrow{\boldsymbol{E_C}} \end{bmatrix} = \begin{bmatrix} s(\lambda) & s(\lambda)+1 \\ s(\lambda)+1 & s(\lambda) \end{bmatrix} \begin{bmatrix} \overrightarrow{\boldsymbol{E_A}} \\ \overrightarrow{\boldsymbol{E_B}} \end{bmatrix} \tag{2.9}$$

where $\overrightarrow{\boldsymbol{E_A}}$ and $\overrightarrow{\boldsymbol{E_B}}$ are given by Eq. 2.7. For single beam illumination conditions ($E_A = 0$ or $E_B = 0$), Eq. 2.9 still holds and correctly describes the thin film response. For simultaneous excitation by the coherent counter-propagating and normally incident beams A and B, the per output channel intensity can by extracted by $I = \vec{\boldsymbol{E}}\vec{\boldsymbol{E}}^*$ and Eq. 2.9:

$$\begin{aligned} I_D &= \overrightarrow{\boldsymbol{E_D}}\overrightarrow{\boldsymbol{E_D}}^* = |s(\lambda)|^2|\overrightarrow{\boldsymbol{E_A}}|^2 + |s(\lambda)+1|^2|\overrightarrow{\boldsymbol{E_B}}|^2 + 2\mathrm{Re}\big\{(s(\lambda)+1)s^*(\lambda)\overrightarrow{\boldsymbol{E_A}}\overrightarrow{\boldsymbol{E_B}}^*\big\} \\ &= |s(\lambda)|^2 {E_A}^2 + |s(\lambda)+1|^2 {E_B}^2 + 2\mathrm{Re}\big\{(s(\lambda)+1)s^*(\lambda)\big\}E_A E_B cos(\Delta\varphi) \end{aligned} \tag{2.10}$$

$$I_C = \overrightarrow{\boldsymbol{E_C}}\overrightarrow{\boldsymbol{E_C}}^* = |s(\lambda)+1|^2|\overrightarrow{\boldsymbol{E_A}}|^2 + |s(\lambda)|^2|\overrightarrow{\boldsymbol{E_B}}|^2 + 2\mathrm{Re}\big\{(s(\lambda)+1)s^*(\lambda)\overrightarrow{\boldsymbol{E_A}}^*\overrightarrow{\boldsymbol{E_B}}\big\}$$
$$= |s(\lambda)+1|^2 {E_A}^2 + |s(\lambda)|^2 {E_B}^2 + 2\mathrm{Re}\big\{(s(\lambda)+1)s^*(\lambda)\big\}E_A E_B cos(\Delta\varphi) \tag{2.11}$$

For $\Delta\varphi = (2N+1)\pi$ and $E_A = E_B = E_0$, which corresponds to placing the thin film at a standing wave node formed by counter-propagating anti-phase input beams of equal amplitudes, Eqs. 2.9 - 2.11 yield:

$$\overrightarrow{\boldsymbol{E_D}} = \overrightarrow{\boldsymbol{E_B}}, \qquad \overrightarrow{\boldsymbol{E_C}} = \overrightarrow{\boldsymbol{E_A}} \qquad \text{and} \qquad I_D = I_C = {E_0}^2 \tag{2.12}$$

The simple result of Eq. 2.12 has a rather fascinating physical meaning for the theory of coherent control of the functionalities of vanishingly thin films which arises from the restriction to electric light-matter interaction in films of deep sub-wavelength thickness. The resulting effect is called *coherent perfect transparency*. In particular, under the aforementioned conditions, a thin film that may be approximated by a single layer — regardless of its optical functionality and without any dependence on its scattering characteristics ($s(\lambda)$) — will be effectively switched off and therefore completely transparent to the impinging light at electric field nodes of the standing wave. *Coherent perfect transparency* constitutes an important state of coherent control because it enables effective all-optical elimination of any planar thin film functionality (e.g. absorption, refraction, optical activity) solely based on the substantially sub-wavelength thickness of the sample and simple interference effects.

On the contrary, at standing wave anti-nodes where $\Delta\varphi = 2N\pi$ and for equal input amplitudes $E_A = E_B = E_0$, Eqs. 2.9 - 2.11 reduce to:

$$\overrightarrow{\boldsymbol{E_D}} = \overrightarrow{\boldsymbol{E_C}} = (2s(\lambda)+1)E_0 \qquad \text{and} \qquad I_D = I_C = |2s(\lambda)+1|^2 {E_0}^2 \tag{2.13}$$

Eq. 2.13 describes the wavelength-dependent light-matter interaction as a function of the film's scattering coefficient at standing wave electric field anti-nodes for equal input amplitudes. Close observation of Eq. 2.13 reveals another intriguing state of the four-port device which occurs when $s(\lambda) = -0.5$ and results in:

$$\overrightarrow{\boldsymbol{E_D}} = \overrightarrow{\boldsymbol{E_C}} = 0 \qquad \text{and} \qquad I_D = I_C = 0 \tag{2.14}$$

This is the condition of *coherent perfect absorption* under which the total input light

intensity is absorbed by the thin film. Interestingly, $s(\lambda) = -0.5$ corresponds to the maximum achievable absorption level in a vanishingly thin film [116, 117] and along with the condition of equal scattering in the forward and backward directions provides the description of the *ideal thin absorber*, see Appendix A. Thus, for an *ideal thin absorber* employed in the coherent control configuration described above, the level of absorption in the system can be tuned all-optically from 0% to 100%, i.e. between *coherent perfect transparency* and *coherent perfect absorption*, respectively.

Following the mathematical description of coherent control of *ideal thin absorbers*, which is the physical mechanism underpinning all demonstrations throughout this thesis, the characteristics and specifications of such a system should be underlined. Firstly, careful observation of Eq. 2.9 reveals that the four-port device is inherently nonlinear, since varying the amplitude of a single input does not imply equal scaling of the output port amplitudes. This counter-intuitive result suggests that despite the linear response of the thin film, nonlinearity is still accessible through the coherent control configuration. More importantly, such nonlinear behaviour is free from slow and energy demanding nonlinearities of nonlinear materials. In particular, the bandwidth of coherent control of absorption in thin films has been proven to solely depend on the de-phasing speed of the film's absorption mechanism [108, 109] and therefore 10s of THz bandwidth can be achieved. Lastly, coherent control of absorption does not depend on one photon modulating another and is therefore compatible with arbitrarily low intensities, down to the single photon regime [107]. These characteristics make coherent control of thin film absorption a powerful tool for ultrafast, energy-efficient, all-optical modulation for future coherent photonic networks and its potential applications will be explored throughout this thesis.

## 2.2 Numerical modelling of coherent perfect absorption

Following the theoretical description of coherent control of thin films and the definition of the *ideal thin absorber*, this section is focused on the selection and design of the appropriate sample that will serve as a suitable *ideal thin absorber* for spatially uniform and spatially addressable coherent control of absorption in the near-infrared, where the experiments of this project will be conducted.

### 2.2.1 A metasurface for coherent perfect absorption

An absorber of deep sub-wavelength thickness for coherent perfect absorption should ideally exhibit the maximum possible level of 50% travelling wave absorption and symmetric splitting of the remaining energy between reflected and transmitted beams, see Appendix A. This cannot be met by conventional unstructured metallic thin films, which tend to be highly transparent or highly reflective. This renders metasurfaces a unique option for creating *ideal thin absorbers* that can be tuned and optimized to operate in any required wavelength range. Although metasurfaces are designed and employed as *ideal thin absorbers* for the purposes of this thesis, they can in principle be engineered to deliver any other property, such as refraction, birefringence, optical activity, as explained in Chapter 1.

The Asymmetrically Split Ring (ASR) geometry has been chosen as the metamaterial building block for the realization of the *ideal thin absorber* in this thesis. This structure was chosen because it supports excitation modes that result in an absorption resonance accompanied by equal transmission and reflection coefficients that can be translated throughout the electromagnetic spectrum [32]. Moreover, it was successfully employed in the initial demonstration of coherent perfect absorption with metamaterials [28]. The structure can be realized either as metallic ASRs fabricated on a dielectric substrate, see inset of Fig. 2.2 a, or as a complementary structure of ASR slits perforated in a metal film, inset of Fig. 2.2 c. For such structures, symmetry breaking was proven to excite a Fano-type resonance [54, 118–120] within a narrow frequency range, see Fig. 2.2 a, where the external stimulus induces anti-symmetric currents along the arcs of the split-ring (II) as shown in Fig. 2.2 b. This excitation mode creates an array of magnetic dipoles oscillating perpendicular to the metamaterial plane, which cannot couple directly to free space as magnetic dipoles cannot radiate in their oscillation direction and as destructive interference prevents the array of sub-wavelength periodicity from radiating in any other direction. This sharp resonance is accompanied by the other two resonances (I, III) depicted in Fig. 2.2 b arising from in-phase current oscillations along the arcs of the split-rings. This overall response is also pronounced as a broad resonance in the absorption spectrum, Fig. 2.2 a (bottom). A similar response is obtained in the optical part of the spectrum, where the geometry of the ASR is downscaled for the visible or near-infrared, see Fig. 2.2 c - d. It should be noted that the optical spectral behaviour of complementary structures (i.e. ASRs realized as metallic wires or as slits),

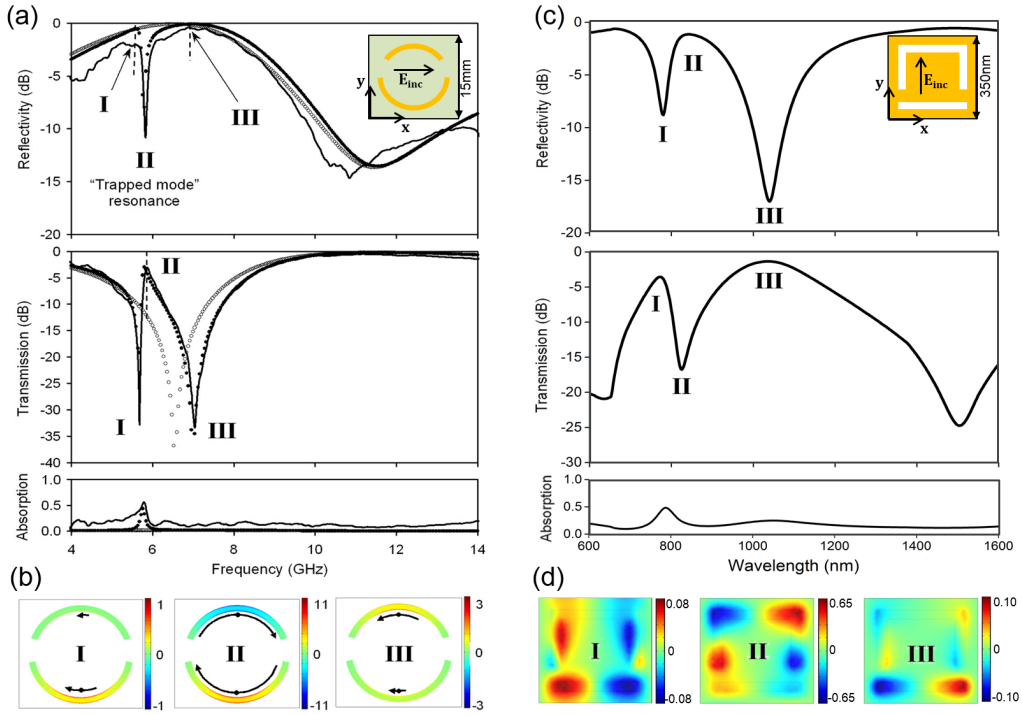


**Figure 2.2: Asymmetrically Split Ring metamaterial.** (**a**) Normal incidence spectra: experiment (solid line) and theory (filled circles) at microwave frequencies for an array of metallic asymmetrically split rings, theory for symmetrically split rings (empty circles). (**b**) $x$-component of the instantaneous current distribution corresponding to resonant features in panel **a**. (**c**) Simulated normal incidence visible to near-infrared spectral response for asymmetric split ring apertures in a gold film. (**d**) Simulated normalized $H_z$ component of the field distribution at resonant wavelengths of panel **c**. [54].

as the ones depicted in the insets of Fig. 2.2 a and c, corresponds to complementary reflectivity and transmittance responses. In complementary structures underpinned by Babinet's principle [121], different polarizations are used in order to excite modes corresponding to complementary spectral features [122]. In the metallic ASR structure, as explained in [54], the incident light must be polarized perpendicular to the structure's line of symmetry for the trapped-mode resonance to be excited. Therefore, in the case of the ASR slit structure, the incident polarization must coincide with the symmetry axis of the structure. As a result, the trapped-modes are best captured in different field components, see Fig. 2.2 b and d.

Based on the detailed description of the ASR metamaterial modes, the requirements for the realization of an *ideal thin absorber* and the targeted wavelength for the experimental demonstrations of this thesis, the theoretical study targeted the design and

optimization of an ASR array perforated in a thin gold film. As will be explained below, it is essential to create a sample that is fully symmetric in the direction of propagation of the counter-propagating beams in the coherent control environment. Therefore, the complementary ASR array is a better choice for this case as it does not require a substrate and can be realized by slits in a metal film. Gold is noble metal that has relatively low dissipation factor and good electrical properties at the near-infrared and is therefore one of the best plasmonic metals. Moreover, it has been widely used for the fabrication of plasmonic metamaterials because it is easy to handle experimentally. Therefore, the ASR structures are designed and fabricated in gold.

A dedicated theoretical study has been performed to determine the proper ASR sample specifications and to test the resulting metamaterial in a coherent control environment. The metamaterial's geometrical parameters were tuned in order to place the absorption resonance at the wavelength of interest, i.e. 785 nm based on the CW laser employed in the experimental setup, and to achieve the 50% single-beam absorption peak as required for optimal performance. In this study of the gold ASR metasurface design, the size of the unit cell, the gold thickness and the slit width were adjusted systematically and several substrates were considered. In the first step of the design, the unit cell of the free-standing gold ASR array described in [28] was scaled down to achieve an absorption resonance at 785 nm. Subsequently, the gold thickness was tuned in steps of 5 nm in order to find the optimum thickness that provides the maximum absorption and is still deeply sub-wavelength. In the last step of the tuning of the absorption resonance, the slit width was varied in order to attain the 50% absorption resonance at 785 nm under the fabrication restrictions imposed by the focused ion beam milling process (i.e. a slit width smaller than 30 nm is difficult to achieve). The use of substrates was also considered since it is significantly easier to fabricate substrate-supported ASR structures and similar tuning steps were followed for the design of the optimum structure for each substrate.

The spectral and coherent control simulations were conducted via the Comsol Multiphysics Finite Element Method (FEM) 3D solver. The 3D model that was employed throughout simulation and design analysis consisted of the metasurface unit cell design sitting between two 2-wavelength-long air blocks (of unit cell sized footprint) on the top and bottom of the unit cell structure, see Fig. 2.3. Periodic boundary conditions were prescribed in all lateral unit cell and air block surfaces for the simulation of an

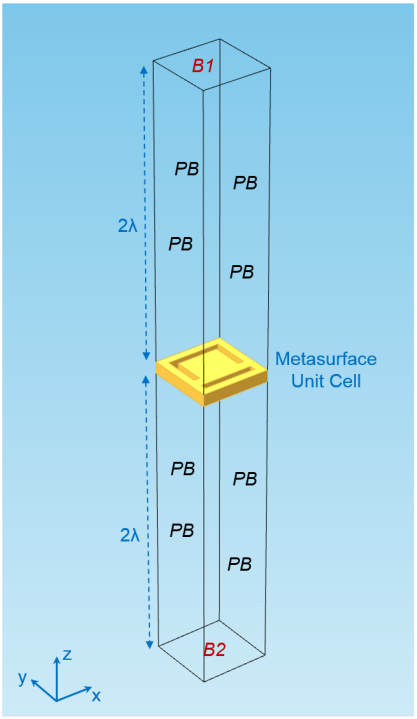


**Figure 2.3: Computational model for the study of ASR samples.** 3D COMSOL model for a free-standing gold ASR unit cell design positioned between 2-$\lambda$-long air blocks. The excitation is applied on surface boundaries B1 and B2. Periodic boundary (PB) conditions are applied to all lateral unit cell and air block boundaries for the simulation of an infinite array.

infinite metamaterial array. Normal incidence plane wave excitation of electric polarization parallel to the ASR symmetry axis ($y$-axis for all models) as well as the variation of the relative beam phase difference ($\Delta\varphi$) for the purposes of coherent control simulations were applied on the end surface boundaries of the 3D model (B1 and B2) for all following cases. In all coherent control simulations the normally incident co-polarized plane wave excitations (beams A and B) applied on both end surface boundaries have equal amplitudes. Fig. 2.3 corresponds to the modelling of a free-standing gold ASR array. However, additional geometry blocks of appropriate thickness were added on the bottom of the metasurface unit cell for the modelling of metasurface arrays supported by a substrate. In all cases, the excitation boundaries (A and B) were two wavelengths away from each side of the metasurface unit cell.

The ideally symmetric case (no substrate on either side) is to be realized by an ASR periodic array perforated in a free-standing gold film, for which the design parameters are captured in Fig. 2.4 a. For single beam illumination, an absorption peak of 48.4%

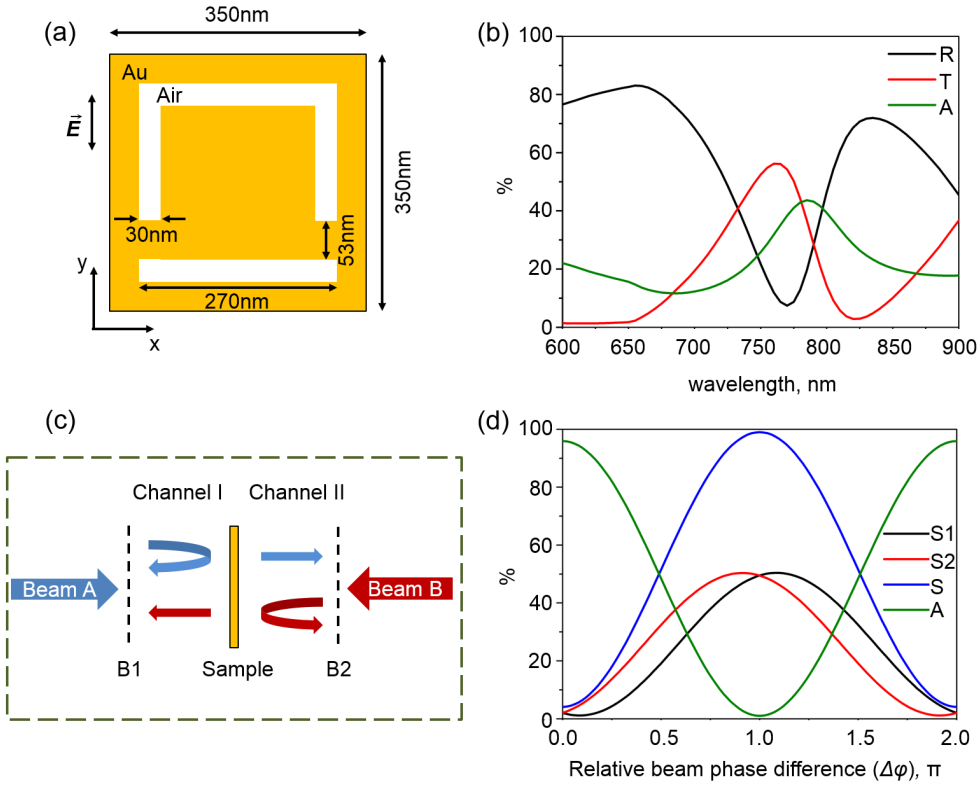


**Figure 2.4: Free-standing ASR gold sample design.** (**a**) Geometry of the metasurface unit cell. The gold thickness is 60 nm. (**b**) Reflection (R), transmission (T) and absorption (A) of the metamaterial for normal incidence illumination with a single beam. (**c**) Light-by-light coherent control configuration. (**d**) Light-by-light modulated output intensities as a function of the relative beam phase difference $\Delta\varphi$: $S_1$ - Output intensity integrated along $B_1$. $S_2$ - Output intensity integrated along $B_2$, $S$ - combined output intensity, $A$ - total absorption. $S_1$, $S_2$, $S$ and $A$ are normalized to the total input intensity.

was achieved for a 60 nm thick gold sample at 785 nm wavelength, Fig. 2.4 b. It is noted that the metasurface thickness corresponds to $\lambda/13$ at the design wavelength, which is in accordance to the theoretical requirement of deep sub-wavelength thickness. The quality factor $Q$ of this absorption resonance, defined as the resonance frequency divided by the resonance's Full Width Half Maximum (FWHM), equals 13. This is a typical value for ASR metasurfaces operating in the visible to near-infrared spectral range.

The same model was used to simulate the metamaterial's response under illumination by two coherent co-polarized counter-propagating plane waves A and B at normal incidence, when the phase of excitation beam A and thus the relative beam phase difference at the metamaterial position ($\Delta\varphi$) varies from 0 to $2\pi$. As depicted in Fig. 2.4 c, the non-absorbed output power in this model is distributed over Channels I and II. In

Channel I, the integral of the output power $S_1$ along boundary $B_1$ is composed of the reflected beam A and the transmitted beam B. Similarly, $S_2$ accounts for the transmitted beam A and the reflected beam B integrated along $B_2$. Moreover, the range over which the total output intensity $S = S_1 + S_2$ or total absorption $A = 1 - S$ fluctuate can be defined as the Figure Of Merit (FOM) in this coherent control approach. For the free-standing sample the FOM is derived from Fig. 2.4 d, where $A$ spreads over 1-95.6%, hence the FOM equals 94.6%. The somewhat reduced range of total absorption modulation with respect to the ideal case described in the theoretical analysis of the Section 2.1 arises from the finite sample thickness which results in non-zero coupling of the sample modes with the magnetic field, hence non-zero minimum absorption. Moreover, the absorption peak of the single beam spectrum being slightly lower than the ideal 50% (48.4%) results in less than 100% maximum total absorption. The extensive parametric simulations conducted for the unit cell design proved that obtaining a 50% absorption peak can be quite challenging at the wavelength of interest. Nonetheless, the final modulation range remains very close to the ideal limits.

It is noted that maxima and minima of $S_1$ and $S_2$ are observed for slightly different relative phase differences of the impinging beams in Fig. 2.4 d. This phase shift results from the imperfect performance of the simulated structure and $S_1$ and $S_2$ would coincide for an ideal thin absorber as explained below. For the symmetric case of Fig. 2.4 c, both beam A and B are polarized parallel to the ASR symmetry axis (i.e. $y$-axis for the employed Comsol model orientation), their amplitudes are equal to $E_0$ and the sample reflectivity and transmissivity in terms of fields are $r(\lambda) = s(\lambda)$ and $t(\lambda) = s(\lambda) + 1$ for either side of illumination. Hence, the total scattered fields of Eq. 2.9 can be alternatively written as:

$$\begin{bmatrix} \overrightarrow{\boldsymbol{E_D}} \\ \overrightarrow{\boldsymbol{E_C}} \end{bmatrix} = \begin{bmatrix} r(\lambda) & t(\lambda) \\ t(\lambda) & r(\lambda) \end{bmatrix} \begin{bmatrix} E_0 e^{-i(\omega t - \Delta\varphi)} \hat{\boldsymbol{y}} \\ E_0 e^{-i(\omega t)} \hat{\boldsymbol{y}} \end{bmatrix} \tag{2.15}$$

at a certain plane across the standing wave, say $z = 0$. This field form imposes that for $\Delta\varphi = N\pi$, the per channel output intensities will be equal, $I_D = I_C$, and therefore $S_1 = S_2$, independently of the nature of the complex transmission $t(\lambda)$ and reflection $r(\lambda)$ coefficients.

However, based on Eq. 2.15, except for trivial cases of $t(\lambda) = 0$ or $r(\lambda) = 0$, for arbitrary relative beam phase differences (excluding $\Delta\varphi = N\pi$), the channel output intensities can only be equal if the complex scattering coefficient is real and therefore

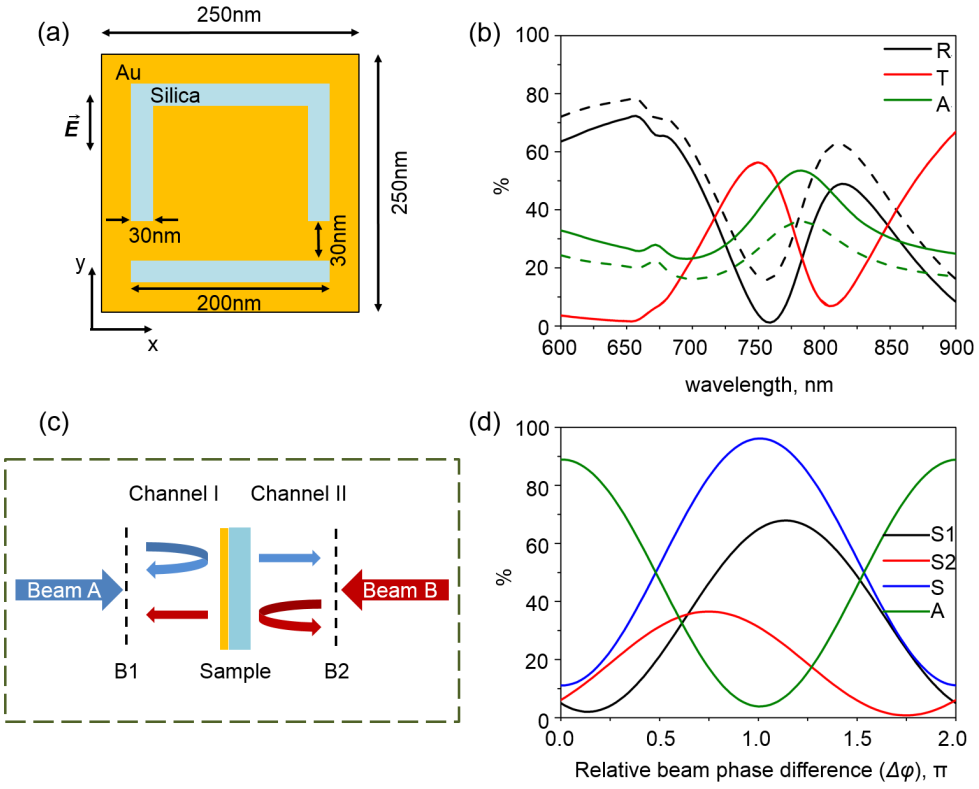


**Figure 2.5: ASR gold sample design on silica substrate.** (**a**) Geometry of the metasurface unit cell. The gold thickness is 50 nm. Silica thickness is 170 $\mu$m. (**b**) Reflection (R), transmission (T) and absorption (A) of the metamaterial for normal incidence illumination with a single beam impinging on silica (solid lines) and on Au (dashed lines). (**c**) Light-by-light coherent control configuration. (**d**) Light-by-light modulated output intensities as a function of the relative beam phase difference $\Delta\varphi$: $S_1$ - Output intensity integrated along $B_1$. $S_2$ - Output intensity integrated along $B_2$, $S$ - combined output intensity, $A$ - total absorption. $S_1$, $S_2$, $S$ and $A$ are normalized to the total input intensity.

the complex transmission and reflection coefficients are both real. Hence, in the case of non-zero imaginary part of the complex reflection and transmission coefficients, the per channel output intensity will be different for phase differences that are not multiples of $\pi$. This physically corresponds to any deviation from the *ideal thin absorber*, which may be introduced by the non-zero sample thickness and less than 50% absorption level and results in the symmetry of the system to be translated to a symmetry between channel output intensities in terms of the relative phase difference which can be described as:

$$S_1(\pi - \Delta\varphi) = S_2(\pi + \Delta\varphi) \tag{2.16}$$

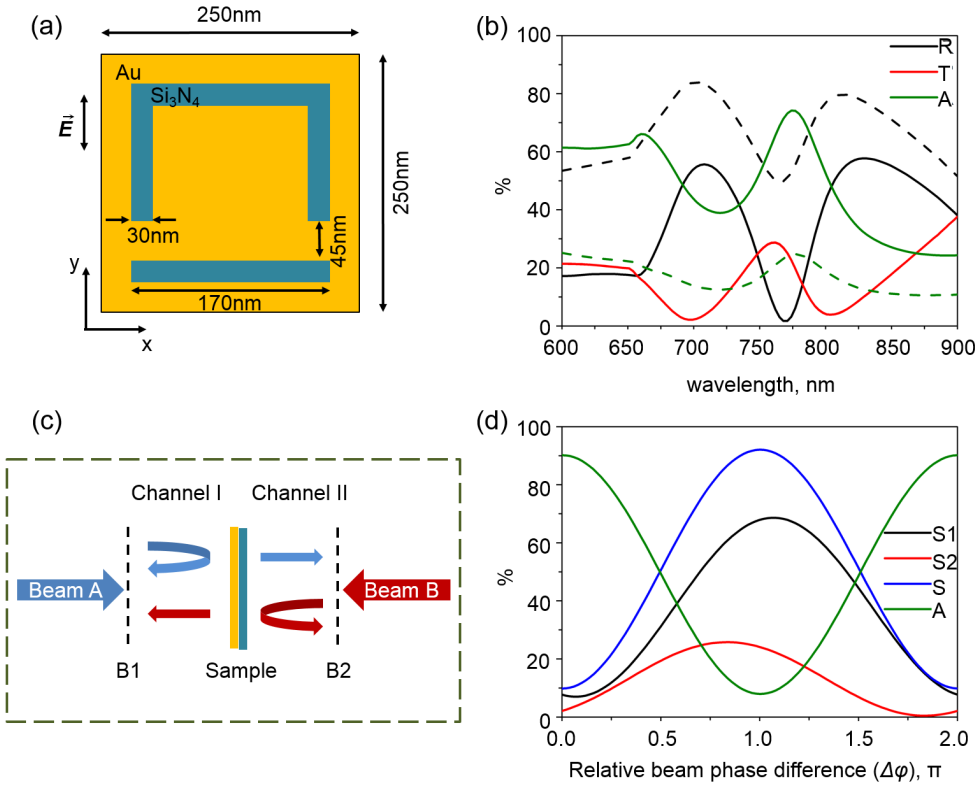


**Figure 2.6: ASR gold sample design on $Si_3N_4$ substrate.** (**a**) Geometry of the metasurface unit cell. The gold thickness is 50 nm. $Si_3N_4$ thickness is 50 nm. (**b**) Reflection (R), transmission (T) and absorption (A) of the metamaterial for normal incidence illumination with a single beam impinging on $Si_3N_4$ (solid lines) and on Au (dashed lines). (**c**) Light-by-light coherent control configuration. (**d**) Light-by-light modulated output intensities as a function of the relative beam phase difference ($\Delta\varphi$): $S_1$ - Output intensity integrated along $B_1$. $S_2$ - Output intensity integrated along $B_2$, $S$ - combined output intensity, $A$ - total absorption. $S_1$, $S_2$, $S$ and $A$ are normalized to the total input intensity.

Thus, this analysis explains all features depicted in Fig. 2.4 d. In practice, it is remarkably easier to fabricate a sample supported by a silica or $Si_3N_4$ substrate. Therefore, the previous simulations have been repeated for these cases in order to have a complete library of possible designs for future fabrications. As denoted in Fig. 2.5 b, for a 50 nm thick gold sample on a silica cover slip of 170 $\mu$m thickness (realized by adjusting the refractive index of the bottom air block in Fig. 2.3), the single beam reflection and absorption spectra differ for the two directions of incidence (A: 53.5%/35.9% for light impinging on the silica/Au side of the sample) due to the asymmetry introduced by the substrate along the propagation axis. Therefore, the light-by-light control configuration (Fig. 2.5 c) reveals an asymmetry in the modulation of the two output channels. In

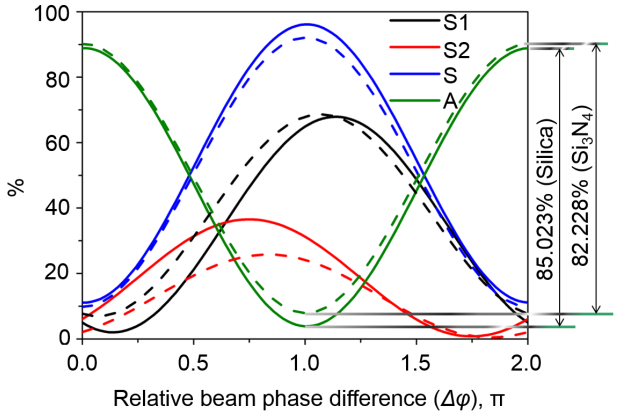


**Figure 2.7: Comparison of coherent control responses** for ASR samples on silica and $Si_3N_4$ substrates. Silica (solid lines), $Si_3N_4$ (dashed lines). The graph is composed of Fig. 2.5 and Fig. 2.6 results.

particular, the total intensity of the incident beams is unevenly distributed between the two output channels. As a result, maxima and minima of the total absorption lie within a range of 3.9-88.9% (FOM=85%) of the total input intensity. Similar yet more pronounced asymmetries in the optical characteristics are observed for an optimized 50 nm gold ASR sample on a 50 nm thick $Si_3N_4$ membrane (realized by adding a 50 nm-thick block of appropriate refractive index in the bottom of the metasurface unit cell in Fig. 2.3), see Fig. 2.6.

Finally, Fig. 2.7 reveals the minuscule difference between the on-silica and the on-$Si_3N_4$ samples in terms of total absorption. The FOM differs only by about 3%. At the same time, a less pronounced difference between the separate output channels is observed in the case of silica substrate.

In conclusion, an optimised library of possible samples has been created for the implementation of an ASR metamaterial for coherent control of absorption of light by light. Feasible samples can be fabricated on silica or $Si_3N_4$ substrates without introducing dramatic deterioration (10% FOM deterioration) of the coherent control behaviour with respect to the ideal symmetric case. In the following section, the response of the ASR free-standing gold sample will be investigated under the spatially addressable coherent control scheme.

### 2.2.2 Metasurface response under spatially varying illumination

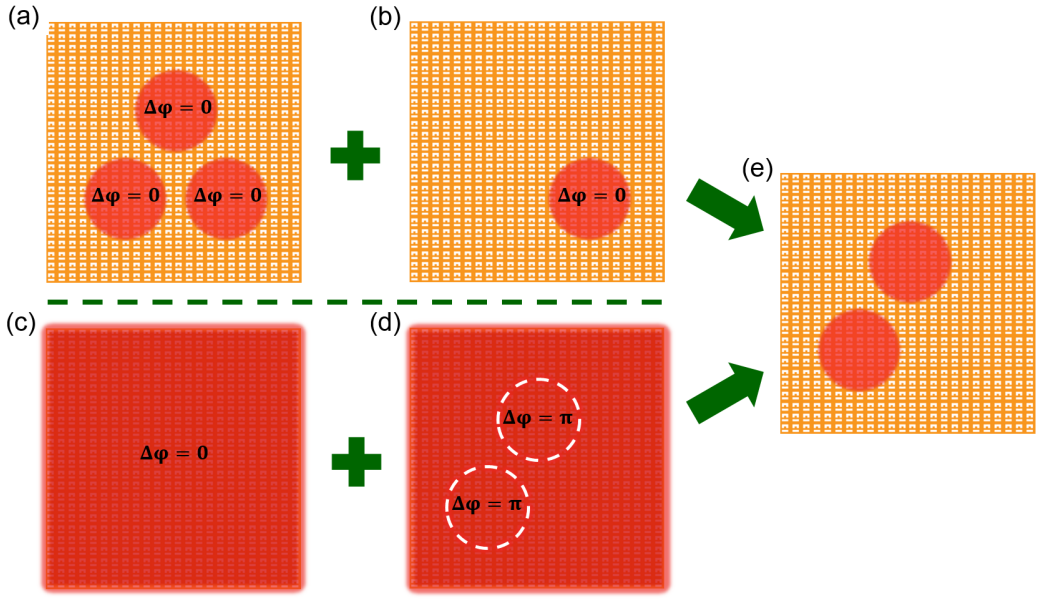


**Figure 2.8: Spatially addressable coherent control concept.** Coherent perfect absorber illuminated by a structured intensity profile of either beam A (**a**) or beam B (**b**) or instead a uniform intensity profile with structured phase of either beam A (**c**) or beam B (**d**). Simultaneous coherent illumination of the metasurface by either patterns **a** and **b** or patterns **c** and **d** yield the same pattern (**e**), except for a difference in intensity subject to single beam reflection, transmission and absorption levels which is not depicted in this conceptual figure.

The coherent control platform as discussed so far leads to modulation of light with light where temporal control is accessed through the translation of the standing wave position with respect to the thin film. A whole new level of functionality would be achieved by simultaneous control over the expression of sample properties in space. Such a possibility would demonstrate a fully dynamic all-optical process. This can be achieved by applying spatially varying intensity and/or phase profiles to the counter-propagating coherent wavefronts. For instance, as illustrated in Fig. 2.8 a, the ASR array can be illuminated with an image which is encoded in the intensity profile of beam A. In order to coherently absorb only the bottom right circle of this image on the metasurface, the intensity profile of the counter-propagating coherent beam B needs to be properly tailored as depicted in Fig. 2.8 b for in-phase beams A and B. The interaction of these two profiles results in the deletion (*coherent perfect absorption*) of this part of beam A, as depicted in Fig. 2.8 e. A similar outcome can be attained for the case of a uniform phase and intensity profile for

beam A (Fig. 2.8 c) and a prescribed spatially varying phase profile (uniform intensity across wavefront) for beam B (Fig. 2.8 d), so that *coherent perfect absorption* occurs only on the metasurface area which beams A and B reach in phase.

The spatially addressable approach raises the question of how accurately a phase or intensity non-uniformity can be resolved by the metasurface. In other words, how sharp are the transitions that can be achieved between metasurface areas where the spatially varying illuminating profiles are supposed to exhibit maximum and zero absorption? Is the inter-meta-molecular coupling within the array a limiting factor in this system? The full computational analysis of this problem would require modelling of a large metamaterial array which would be excited by spatially varying wavefronts. Unfortunately, such simulation demands excessive computational resources (memory and time). Therefore, rows and columns of meta-molecules will be modelled seperately to investigate the array performance under spatially addressable coherent control.

The computational analysis focuses on the construction of a model that best describes an ASR metasurface area, within which the excitation of coherent absorption passes from maximum to zero (i.e. the counter-propagating wavefront profiles should form a standing wave anti-node and node in adjacent areas of the array). In order to decrease the necessary number of degrees of freedom for the FEM 3D analysis with Comsol, two main axes of possible spatial transitions between maximum and minimum absorption are considered with respect to the array orientation. In this way, the array size must be constrained to finite size only along the excitation transition axis, in order to apply the excitation profile, while periodic boundary conditions can be maintained in the other direction, see Fig. 2.9 a and b. This simplification leads to a considerably reduced model size. The specifics of the model are presented in Fig. 2.9 c.

The chosen finite size of the array corresponds to 12 meta-molecules, see Fig. 2.9 a and b. This is the minimum number of meta-molecules needed to maintain the spectral response and avoid the spectral collapse of resonances that occurs for small array sizes in any direction, [123]. In Fig. 2.9 d, the calculated spectral response of the $12 \times \infty$ array is plotted on top of the infinite array spectrum and validates the spectral consistency of both semi-finite (dots) and infinite models (continuous line).

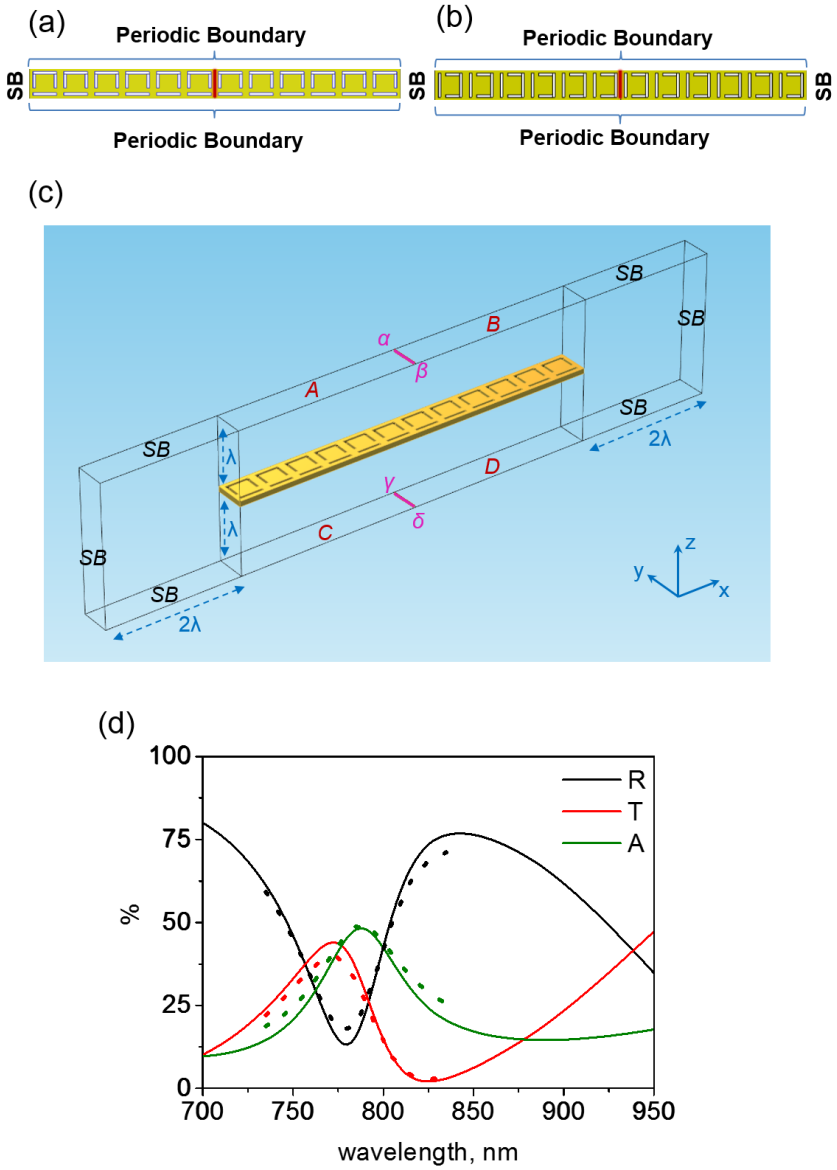


**Figure 2.9: Computational model for spatially addressable coherent control.** The response of $12 \times \infty$ gold ASR aperture arrays oriented as illustrated in (**a**) and (**b**) is simulated by applying periodic boundary conditions to the top and bottom boundaries of these horizontally finite arrays. The pink line annotates the transition between areas excited by different illumination phase and/or intensity profiles. (**c**) 3D model for array **a**. Boundaries A, B, C, D one wavelength ($\lambda$) away from the array are used to apply different excitations from either side. Periodic boundary conditions are prescribed to all front and rear boundaries. Scattering boundaries (SB) are prescribed $2\lambda$ away from the left and right ends of the array in order to eliminate any unwanted reflections. (**d**) Single beam spectral response of the investigated ASR design in terms of reflectivity (R), transmission (T) and absorption (A). Lines correspond to simulations of an infinite array simulated as a single meta-molecule with periodic boundary conditions applied to all lateral boundaries (as shown in Fig. 2.4). Dots represent the spectral response as calculated by the model of panel **c** for single beam uniform illumination.

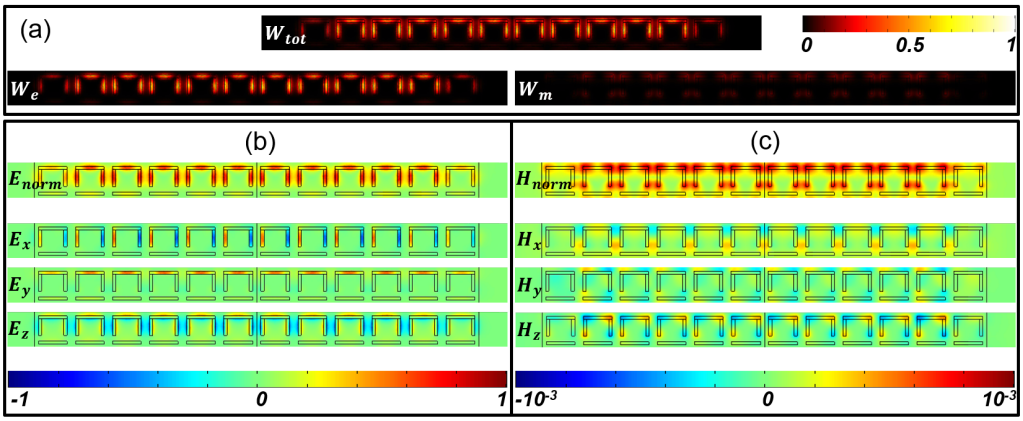


**Figure 2.10: ASR array under uniform single beam excitation.** (**a**) Total $W_{tot}$, electric $W_e$ and magnetic $W_m$ field energy densities normalized to the maximum total energy density and plotted on the same colour scale. (**b**) Electric field amplitude and $x$, $y$, $z$ electric field components normalized to the maximum electric field amplitude plotted on the same colour scale. (**c**) Magnetic field amplitude and $x$, $y$, $z$ magnetic field components normalized to the maximum magnetic field amplitude plotted on the same colour scale. All distributions are plotted 5 nm away from the array.

Fig. 2.9 c illustrates the 3D model geometry for the array orientation shown by Fig. 2.9 a. Excitation boundaries stand a wavelength away from the array to guarantee plane wave excitation. By separate definition of field distributions on boundaries A and B as well as C and D, the excitation differentiation from either side of lines $\alpha\beta$ and $\gamma\delta$, respectively, is achieved. In the following cases, the linearly polarized light is always polarized along the meta-molecules symmetry axis, ($y$-axis of Fig. 2.9 c for the semi-finite array of Fig. 2.9 a and $x$-axis for the one of Fig. 2.9 b. The field and energy distributions in the near-field of the array under single beam uniform illumination prescribed across boundaries A and B are given in Fig. 2.10. The comparison of the field and energy density distributions leads to the conclusion that the analysis can be based on the electric field amplitude $E_{norm}$ and energy density $W_e$, since the magnetic field contribution is minuscule in the near field of the ASR array.

All necessary information on the inter-meta-molecular coupling and the excited modes lies in the array's near-field under coherent excitation and therefore the near-field is plotted in all cases on a plane 5 nm away from the array. In the first case to be considered, $E = 0$ along both boundaries A and C and $E_y = 1$, $E_y = 1e^{i\Delta\varphi}$ along boundaries B and D, respectively, see Fig. 2.11 a. As expected, across excited areas, for

$\Delta\varphi = 0$, the energy density close to the array is the quadruple of the energy density for single beam excitation. For $\Delta\varphi = \pi$, the array is not excited ($E$-field amplitude and energy density close to 0). Based on the maps of E-field amplitude in the near-field, a strict and cautious estimate would account for two neighbouring meta-molecules (on the left of the pink dashed line) being weakly excited (with the furthest meta-molecule being almost negligibly excited) through coupling to the illuminated part of the array. Even if this weak excitation is considered to contribute to the overall performance, the area covered by 2 meta-molecules is close to the diffraction limit of the optical system (defined as $0.61\frac{\lambda}{NA}$, where NA is the numerical aperture of the system's optics and is equal to 0.8) and any underlying coupling effect will be rather difficult to resolve.

Moreover, the energy coupling is minuscule, left column of Fig. 2.11 a. If the resolution of the imaging system was sufficient to detect the effect from meta-molecules excited through coupling, the ASR array design optimization could further reduce the coupling (e.g. by increasing the inter-meta-molecular spacing). Identical conclusions are derived for the array response under spatially varying phase profiles, as shown in Fig. 2.11 b. This time, $E_y = 1$ along boundaries A, B and C, whereas $E_y = 1e^{i\Delta\varphi}$ along boundary D.

For the consistency of the analysis, the array response for the case of the transition line being perpendicular to the ASR symmetry axis (array orientation shown in Fig. 2.9 b) must also be considered. Respective results are presented in Fig. 2.12. For this case, two orientations of the ASR are considered as shown in Fig. 2.12 a, c and b, d to account for any differences that may occur when either the "I" or "C"-shaped slit part of the excited ASRs faces the pink dashed line. Once again, any inter-meta-molecular coupling is limited to a maximum of two neighbouring meta-molecules, which is not problematic or restrictive for our experiments as explained above.

It must be underlined that a further investigation has been conducted to reveal any possible differences when the line $\alpha\beta$ of Fig. 2.9 d is translated across the array in steps smaller than the unit cell size to account for different positions within the unit cell.

However, the total maximum coupling observed in all cases corresponds to two meta-molecules (the furthest of which is almost negligibly excited).

Taking all the above into consideration, the conclusion is that the selected ASR design has a rather satisfactory performance under the spatially addressable coherent

scheme and its effect on the spatial resolution of such a system is minor as compared to the diffraction limit. Therefore, this design is adopted for the experimental implementation that will be demonstrated in the following chapters. A dedicated study on the overall spatial resolution limitations of the experimental platform will be presented in Chapter 4.

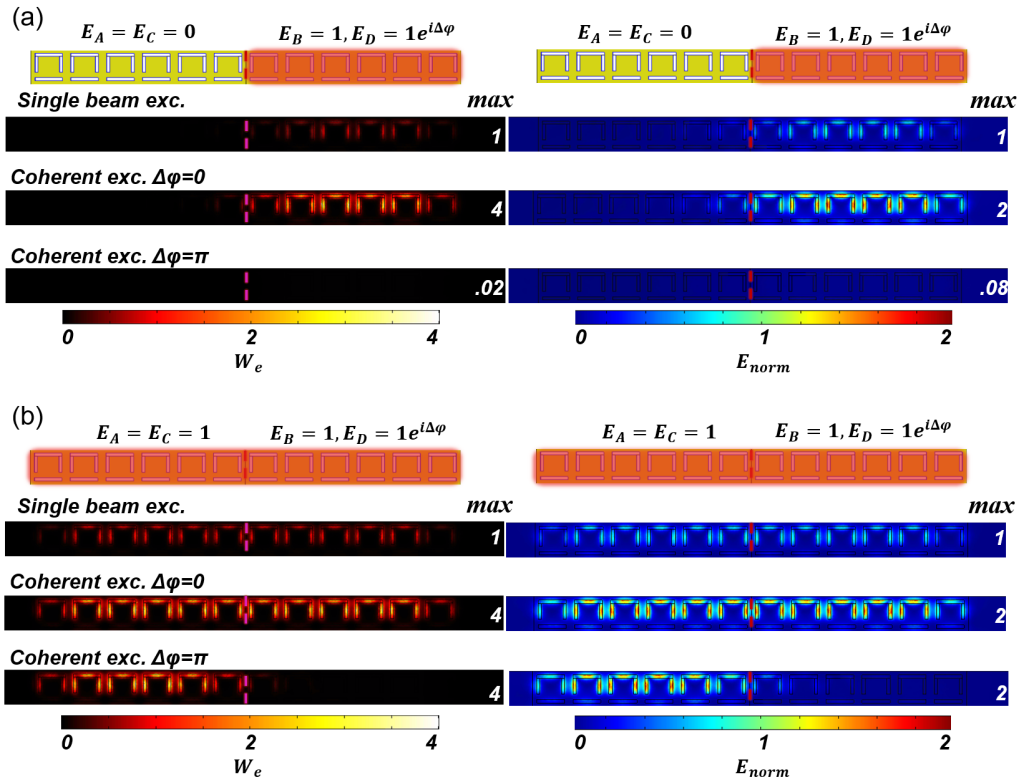


**Figure 2.11: ASR array under spatially varying excitation: Excitation transition boundary line parallel to the array's symmetry axis.** In all graphs the resulting $W_e$ (left) and $E_{norm}$ (right) under the excitation profile are depicted conceptually in the $1^{st}$ row (annotations according to Fig. 2.9 c). The near-field under single beam excitation is presented in the $2^{nd}$ row and coherent in-phase and out-of-phase excitation with two beams are shown in the $3^{rd}$ and $4^{th}$ rows, respectively. In case of in-phase excitation, $W_e$ quadruples and $E_{norm}$ doubles. (**a**) Spatially varying intensity. (**b**) Spatially varying phase. In all figures the pink dashed line corresponds to line $\alpha\beta$ of Fig. 2.9 c. All $W_e$ distributions are normalized to the maximum $W_e$ resulting from illumination with a single beam and plotted on the same colour scale. $E_{norm}$ results are normalized to the maximum $E_{norm}$ resulting from illumination with a single beam and plotted on the same colour scale. All distributions are plotted 5 nm away from the array.

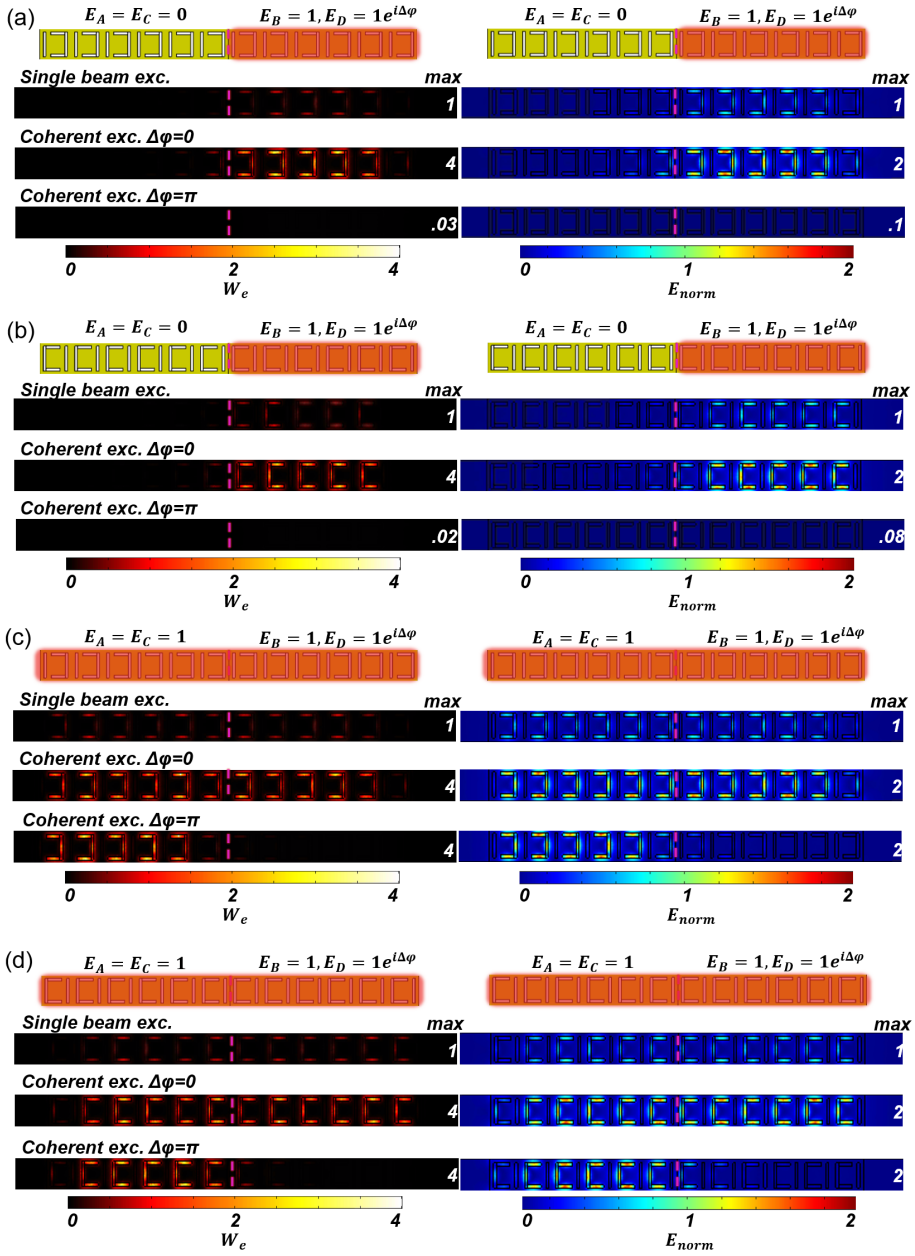


**Figure 2.12: ASR array under spatially varying excitation: Excitation transition boundary line perpendicular to the array's symmetry axis.** In all graphs the resulting $W_e$ (left) and $E_{norm}$ (right) under the excitation profile are depicted in the $1^{st}$ row. The near-field under single beam excitation is presented in the $2^{nd}$ row and coherent in-phase and out-of phase excitation are shown in the $3^{rd}$ and $4^{th}$ rows, respectively. For in-phase excitation $W_e$ quadruples and $E_{norm}$ doubles. (**a**) - (**b**) Spatially varying intensity. (**c**) - (**d**) Spatially varying phase. In all figures the pink dashed line corresponds to line $\alpha\beta$ of Fig. 2.9 c. All $W_e$ distributions are normalized to the maximum $W_e$ resulting from illumination with a single beam and plotted on the same colour scale. $E_{norm}$ results are normalized to the maximum $E_{norm}$ resulting from illumination with a single beam and plotted on the same colour scale. All distributions are plotted 5 nm away from the array.

## 2.3 Fabrication of metamaterials and masks

### 2.3.1 Metasurface nanofabrication and characterization

The development of nanofabrication technologies over the last two decades enabled the flourishing research of metamaterials and metasurfaces with creative designs that stretch the feature size down to sub-wavelength dimensions across a vast spectral range.

For the purpose of two-dimensional coherent control the Asymmetrically Split Ring array design was chosen to access the necessary absorption resonance at the wavelength of interest (785 nm) as explained in Section 2.2. According to the elaborate simulations that were conducted to finalize the sample design, the symmetry requirements of coherent control revealed the necessity for a truly free-standing gold metasurface sample for optimum system performance. J. Valente (former Nanophotonics and Metamaterials group member) has recently developed a nanofabrication technique for creating truly free-standing gold metasurfaces with ASR designs for the needs of the experiments of this thesis and fabricated the sample to be used as the *ideal thin absorber* in experiments. The process involves thin film deposition, etching and focused ion beam milling (FIB) and will be described in detail in this section.

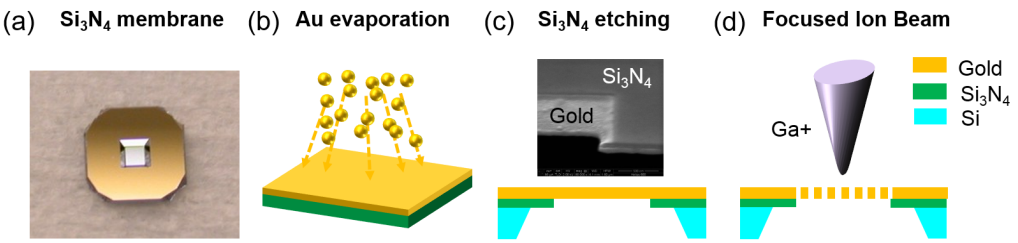


**Figure 2.13: Fabrication process for free-standing gold Asymmetrically Split Ring array.** (**a**) Commercially available $Si_3N_4$ membrane. (**b**) Resistive thermal evaporation of gold on the membrane (artistic impression). (**c**) $Si_3N_4$ membrane substrate removal by reactive ion etching (bottom: schematic diagram of the end result cross-section. top: SEM image depicting the free-standing gold and $Si_3N_4$ parts of the sample). (**d**) Focused $Ga^+$ ion beam milling of the metasurface nanostructure (artistic impression).

The nanofabrication process is initiated with deposition of a thin (60 nm) gold film on a commercially available $Si_3N_4$ membrane (50 nm thick) using resistive thermal evaporation, see Fig. 2.13. Gold deposition occurs in high vacuum in order to reduce the number of particle collisions as the evaporated particles travel towards the substrate,

hence providing increased purity of the final films. Gold pellets contained in tungsten crucibles are electrothermally heated up to the melting point of gold by applied current. Optimization of deposition parameters, such as pressure, temperature and evaporation rate can further improve the quality of the final gold thin films (i.e. roughness, high uniformity). For this thesis, the resistive thermal evaporation was conducted in high vacuum ($2 \times 10^{-6}$ mbar) with gold pellets (99.99%) at evaporation rates of 0.10 nm/s.

For the end result of a truly free-standing gold sample, Reactive Ion Etching (RIE) was employed to remove the supporting $Si_3N_4$ substrate after the resistive thermal evaporation of the thin gold film. RIE is a dry etching technique which occurs in an ion plasma environment and enables the easy and gentle removal of material without affecting neighbouring materials (gold in this case). High-energy ions from a chemically reactive plasma generated by an electromagnetic field in vacuum interact with $Si_3N_4$ and the induced chemical reaction results in the removal of $Si_3N_4$. Gas pressure is maintained between $10^{-3}$ to $10^{-1}$ mbar and the frequency of the applied RF electromagnetic field is typically set to 13.56 MHz applied at a few hundred Watts. For this particular process the precursor gases are $CHF_3$ and Ar with fluxes 2 sccm (sccm = standard cubic centimetres per minute) and 10 sccm, respectively and RF power is about 80 W. With these settings, gold remains intact and the $Si_3N_4$ substrate of 50 nm thickness is removed in approximately 10 minutes. At the end of the etching step (Fig. 2.13 c), the resulting free-standing gold film is ready to be perforated with the desired metasurface profile by focused ion beam milling.

The milling process is performed in the FEI Helios 600 NanoLab instrument. Focused ion beam milling is conducted in a vacuum chamber where pressure is maintained below $10^{-7}$ mbar. Liquid Ga is extracted from a liquid source by electric field induction upon high voltage. Ions of Ga are then accelerated and form an ion beam of typical energy between 10 and 30 keV for the milling process. The beam profile is shaped by an aperture and subsequently condensed by an electrostatic lens and corrected for astigmatism by an octopole. Variation of the beam current between 1 pA and 22 nA is achieved by a variable aperture. The beam current defines the resolution of the FIB milling. A blanking deflector and aperture are used to blank the beam during fabrication. Another octopole performs the raster scanning of the beam over the sample in a user-defined pattern and a second electrostatic lens focuses the beam to a fine spot enabling resolution in the sub-5-nm range. Material removal from the sample is achieved by physical

sputtering induced by the FIB through a series of collisions of the incident ions with the solid target (Fig. 2.13 d). The milling is carried out in a repetitive scanning manner and can create a vast range of surface topologies via control of the scanning pattern, location and ion dosage. In this work a focused 30 keV $Ga^+$ ion beam of less than 5 nm diameter can create features less than 30 nm in size.

The FIB system is supplemented by a scanning electron microscope (SEM) system that has the same focal spot and facilitates imaging of the sample area to be processed by the FIB as well as monitoring of the FIB milling in real time. SEM imaging is the tool for initial characterization of the fabricated metasurface samples.

For the spectral characterization of metasurfaces, a CRAIC micro-spectro-photometer is used to measure the optical properties of the fabricated samples. For such measurements, initial reference spectra corresponding to 0% and 100% reflectivity and transmission are acquired followed by reflection and transmission spectrum acquisition for either side of the sample under linearly polarized broadband light illumination generated by a Halogen lamp.

For the purposes of two-dimensional control of light with light, a free-standing gold sample was perforated with a 100 $\mu$m $\times$ 100 $\mu$m array of ASR meta-molecules based on the design specifications of the previous section. The sample was fabricated by J. Valente. An SEM image and the measured sample spectrum are presented in Fig. 2.14. For illumination of the front and back sides of the sample, measurements indicate almost identical properties (averaging the front and back side response for each case): 35% absorption, 37% transmission and 28% reflection at 785 nm. Quantitative deviations including the shifting and broadening of the spectral resonance, are attributed to fabrication deficiencies of the newly developed procedure for creating free-standing gold metasurfaces. Nonetheless, the sample response at the wavelength of interest is considered sufficient for the experimental needs of this thesis which focuses on the design, operation and characterization of the metadevice and its applications, rather than the optimization of the free-standing metasurface fabrication scheme. Deviations from the theoretical description of coherent control due to the less than ideal single beam absorption level will be discussed in each experimental chapter in order to appropriately describe each individual application.

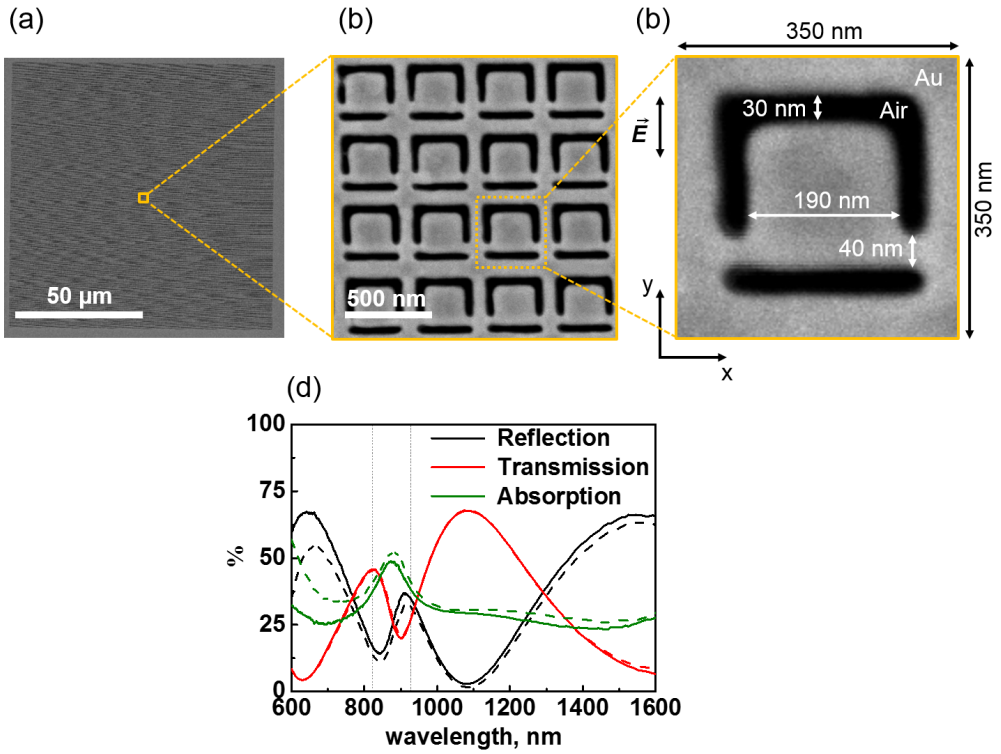


**Figure 2.14: Fabricated free-standing gold Asymmetrically Split Ring metasurface.** (**a**) SEM image of the fabricated 100 $\mu$m × 100 $\mu$m ASR array. (**b**) Enlarged view of the central part of the fabricated metasurface annotated by the yellow square in **a**. (**c**) Enlarged view of a unit cell of the fabricated metasurface annotated by the yellow square in **b**. (**d**) Measured spectral response of the fabricated sample for illumination from the front (solid lines) and rear side (dashed lines) of the metasurface.

### 2.3.2 Mask fabrication

Throughout the experimental demonstrations of this thesis, coherent control is implemented in a spatially addressable way via counter-propagating beams with binary profiles of structured intensity. For this purpose, intensity masks of different types were fabricated for the distinct applications that are presented in the following chapters.

For two-dimensional profiles with coarse features (down to 0.9 mm aperture diameters) of low complexity, a milling machine was used to drill apertures of various diameters on purpose-designed 1 mm thick aluminium mask templates. The optical setup where the masks will be used is constructed on a 30 mm cage system as will be explained in Section 2.4. Therefore, mask templates included 30 mm cage system compatible mount features, see Fig. 2.15 a and b, in order to be properly positioned at prescribed positions

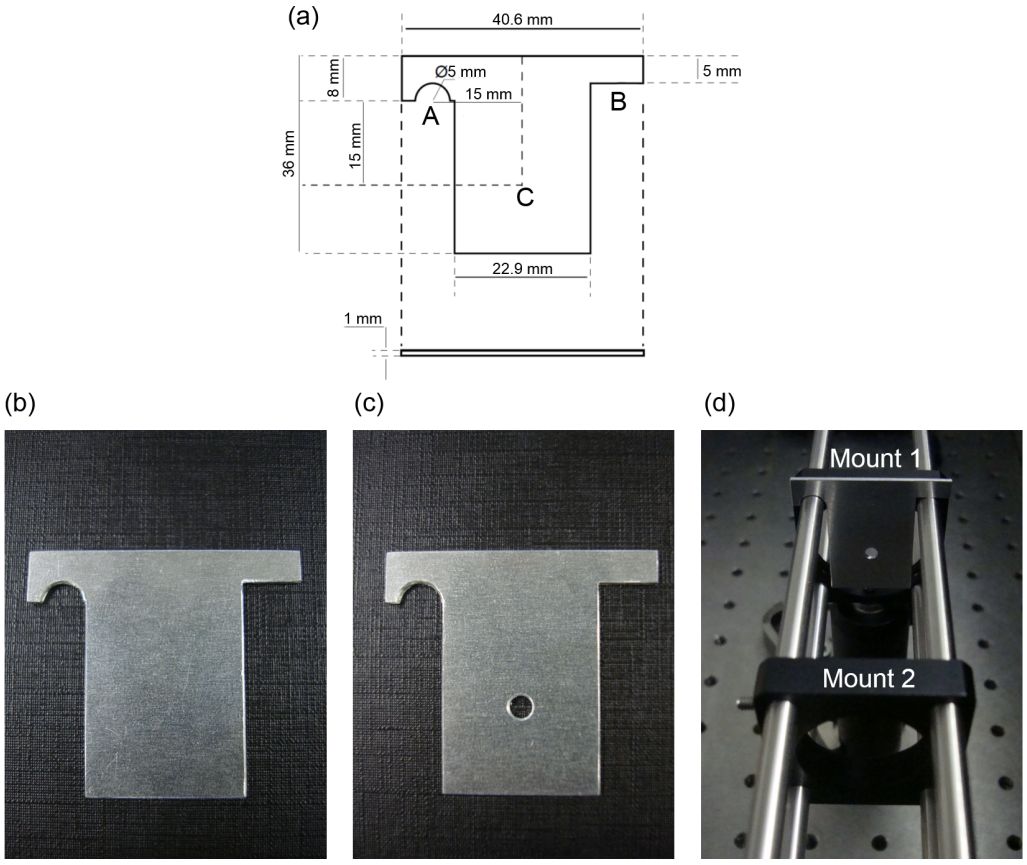


**Figure 2.15: Binary intensity masks fabricated with mechanical milling.** (**a**) Mask template design and dimensions. Features around points A and B are properly tailored for mounting on a 30 mm cage system resulting in the alignment of the centre C of the mask with the optical axis of the cage system. (**b**) Fabricated aluminium mask template. (**c**) Fabricated aluminium mask template with 1.5 mm aperture drilled in the centre of the mask. (**d**) Mask mounting mechanism to avoid tilting with respect to the optical axis of the cage. Mount 1 (30 mm cage compatible 1" clear aperture plate) is fixed on the cage to determine the positioning of the mask across the optical path. Mount 2 (30 mm cage compatible 1" clear aperture plate) is pressed against the mask to restrict any mask movement or tilt throughout experiments. Fabricated masks are presented before being painted black for illustration purposes.

along the cage-supported part of the optical system and aligned with the system's optical axis. Depending on the binary profile to be imposed, apertures of prescribed diameter were drilled in the aluminium mask templates, Fig. 2.15 c. Subsequently, the masks were painted black to avoid any unwanted reflections. The minimum achievable feature with this technique corresponds to a 0.9 mm diameter aperture. Finally, when mounted on the cage system, the masks were placed between two 30 mm cage compatible 1" clear

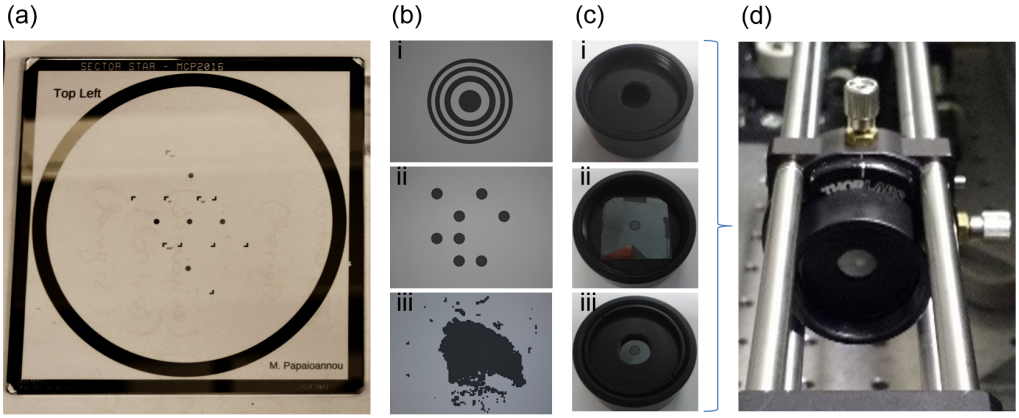


**Figure 2.16: Binary intensity masks fabricated with photo-lithography.** (**a**) Commercially produced custom photo-mask including designs for experimental demonstrations of this thesis. Metal features of the photo-mask prevent the exposure of sample areas to be removed during "lift-off". (**b**) Optical microscope images of selected fabricated photolithography mask examples: i - Fresnel Zone plate pattern, ii - circular dot pattern, iii - binary satellite image of Arctic and Greenland areas. Gray areas correspond to chromium and black areas to glass (**c**) Mask mounting mechanism: i - 1" mount to be mounted on a 30 mm cage plate with the rear mask surface protected by a rubber ring, ii - Square mask of 1" diagonal positioned on the protective rubber ring, iii - top mask surface protected by the second rubber ring and the retaining ring. (**d**) Mask and kinematic mounting mechanism assembly in the optical system.

aperture plates to avoid tilting with respect to the optical axis, Fig. 2.15 d.

For complex binary intensity profiles of higher resolution (smaller features than the mechanical drilling minimum feature of 0.9 mm), binary chromium on silica masks were fabricated by photo-lithography. 18 mm $\times$ 18 mm silica cover slips of 120 - 170 $\mu$m thickness and high flatness quality were prepared for the photolithography process. The cover slip preparation involved solvent cleaning to remove any residues and dust from the surface through subsequent sonic baths of acetone, isopropanole and de-ionized water followed by blow-drying process. Positive photo-resist (Microposit S1813) was then spin-coated on the sample. The photo-resist thickness is dictated by its viscosity and the spin coating rotation speed and is a critical parameter for achieving good resolution and efficient material removal. The resist thickness must be larger than the deposited material thickness to efficiently separate features to be removed from desired features on the final sample during lift-off and sufficiently small in order not to compromise the achievable resolution. For the demonstrations presented in this thesis, the metal film thickness is set to 120 nm (unless stated otherwise) to ensure minimum transmission

through the opaque areas of the fabricated masks and the minimum feature is 22 $\mu$m throughout the employed designs. For these requirements the spin-coating occurred at a rotation speed of 4500 rpm (rotations per minute) which corresponds to a thickness of 1-2 $\mu$m for the used photo-resist. The resist-coated samples were then heated to 110°C for 60 s and exposed to UV light through a photo-mask which included the negatives of the desired binary intensity profiles for the experimental demonstrations, see Fig. 2.16 a. After exposure, the sample was sunk into a developer bath for 50 s to remove the exposed photo-resist and then washed and dried. In the next step, 120 nm of chromium were deposited on the sample with electron beam evaporation. This physical vapour deposition technique occurs in vacuum (less than 1 $\times 10^{-6}$ mbar) where an intense electron beam is generated from a filament and directed via electromagnetic fields to a source crucible including the material (in this case chromium) to be vaporized due to heating via energy transfer and deposited on the sample. The last step of the mask fabrication process is known as "lift-off". During this stage, the samples are treated in sonic baths with acetone resulting in the removal of the unexposed photo-resist with the metal on top which corresponds to the transparent features of the binary designs. The resulting binary mask profiles are examined with an optical microscope, see Fig. 2.16 b. Finally, the mechanism for mounting the fabricated masks on the cage system of the optical setup is shown in Fig. 2.16 c and d. The square (1" diagonal) mask samples are mounted on a 1" mount compatible with the 30 mm cage system's 1" plates. Two clear aperture rubber rings are protecting the front and rear surfaces of the masks which are fixed in the 1" mount with retaining rings. This technique guarantees the accurate positioning of the mask in positions determined by the 1" cage plates and limits tilting of the mask with respect to the optical axis.

## 2.4 Optical imaging interferometer for two-dimensional coherent control of absorption of light

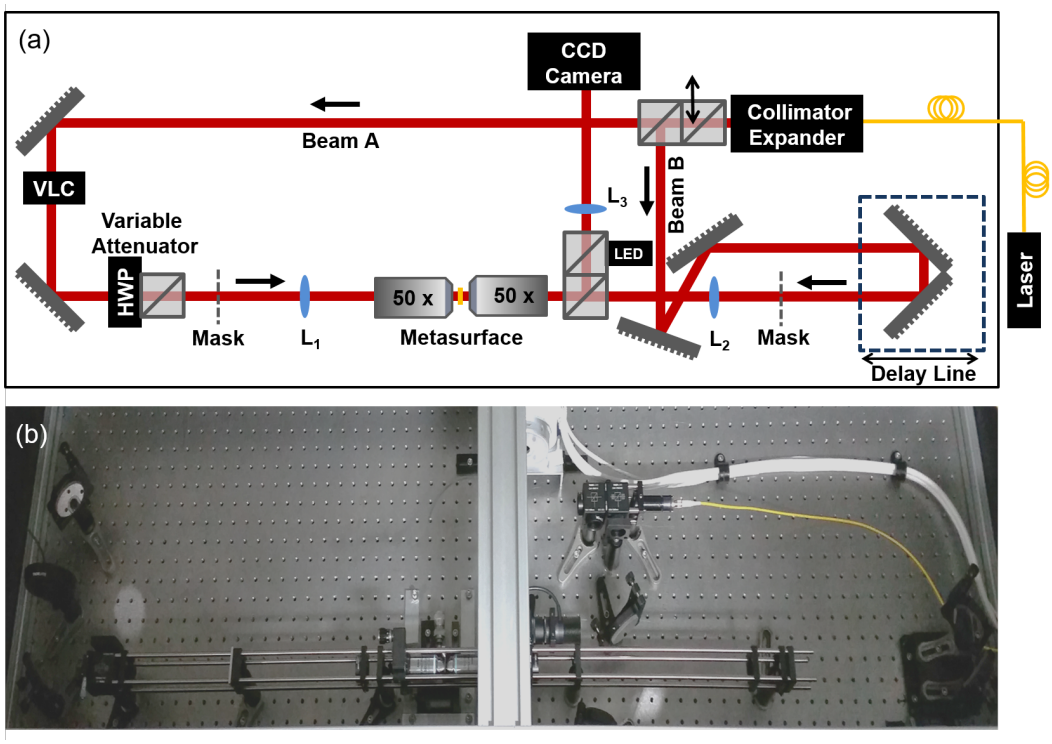


**Figure 2.17: Optical setup for two-dimensional coherent control.** (**a**) Schematic illustration of optical system components. (**b**) Photograph of the experimental configuration. VLC: Variable Liquid Crystal, HWP: Half-Wave Plate, LED: Light Emitting Diode, CCD: Charge Coupled Device.

The spatially addressable coherent control experimental platform consists of a standing-wave interferometer with integrated imaging parts in both interferometer arms. As explained in Section 2.2.2, excitation profiles propagating in either arm can be of varying phase and/or intensity across the wavefront cross-sections. The imaging parts of the interferometer project any distributed excitation profile from the rear focal plane of the imaging system on the thin film or metasurface (front focal plane of the imaging system) from either side. In this way, the interference pattern on the metamaterial plane is spatially modified, accordingly. For the experimentally demonstrated applications of two-dimensional coherent control, the intensity of counter-propagating wavefronts is spatially structured by binary masks which partially block the incident beam wavefronts. Consequently, *coherent perfect absorption* or *transparency* occurs solely over the

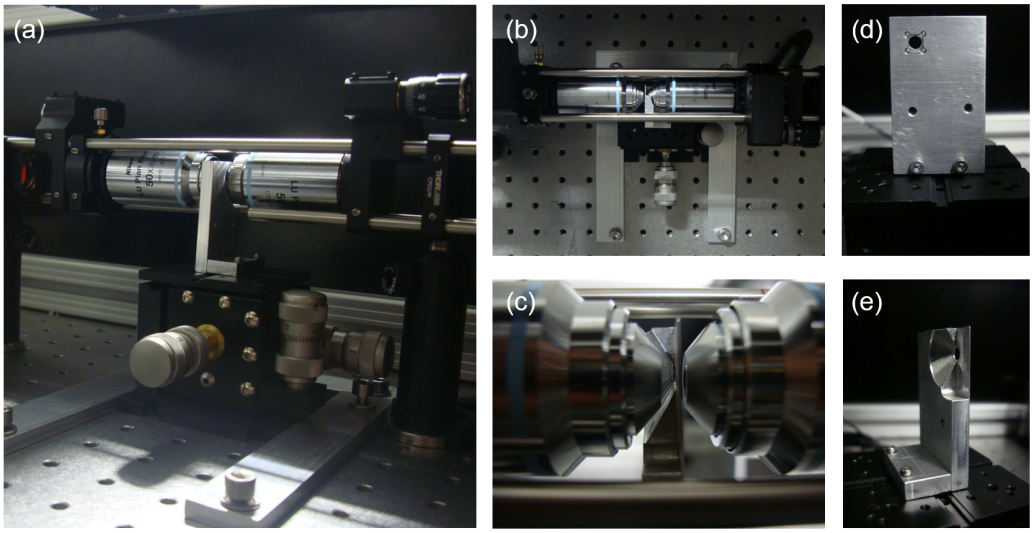


**Figure 2.18: Metasurface sample mounting assembly.** (**a**) Side view, (**b**) top view and (**c**) zoomed-in side view photographs of the sample holder mounting assembly in the optical system illustrating the sample holder designed to fit between the tight objective foci (1 mm working distance) causing minimum disruption to the cage system of the optical step. The sample holder is mounted on an $x$-, $y$- and $z$-translation cube to facilitate accurate positioning of the metasurface with respect to the foci of both objectives. Bulk aluminium trails were designed to fix the translation cube position on the optical bench. (**d**) @Front and (**e**) rear view photograph of the sample holder designed to accommodate the square 5 mm × 5 mm membrane frame supporting the metasurface sample.

metamaterial areas that correspond to non-zero intensity profiles transmitted through the masks from both sides simultaneously.

The experimental setup is depicted in Fig. 2.17. Walking through the setup, a fibre collimator expands the output of a fibre-coupled CW laser diode module operating at 785 nm (in some experimental demonstrations a fibre Bragg grating temperature stabilized laser with a central wavelength of 790 nm and 0.01 nm linewidth is used instead and will be explicitly mentioned in the relevant experimental descriptions). A cubic polariser imposes the desired polarization across the system which is chosen to be parallel to the ASR meta-molecule's symmetry axis on the sample. The beam is then evenly split by a 50:50 beam splitter into beams A and B, which propagate along different paths. The path lengths of the interferometer are precisely matched via a delay line created along the path of beam A. The delay line consists of two mirrors in a retro-reflector configuration mounted on a $z$-axis manual translation stage which is used to ensure the path lengths match within the 600 $\mu$m coherence length of the 785 nm

laser (for the 790 nm laser the coherence length is larger than the overall length of the experimental configuration and no further path length matching is required via the delay line when the optical setup is operated with this source). The variation of the relative phase difference $\Delta\varphi$ between the two beams is introduced by a Variable Liquid Crystal (VLC) retarder located along the path of beam A. In the same path, the combination of a Half-Wave Plate (HWP) with a polarizing beam-splitting cube comprises a variable attenuator used to compensate for any intensity mismatch between the beams.

Up to this point, the system description matches the general description of any standing wave interferometer. The essential addition that is made in the standing wave interferometer used here is the introduction of imaging configurations in the system to impose the two-dimensional mask profiles onto the metasurface without disrupting the sensitive operation of the interferometer. Two identical imaging configurations are employed in either arm of the interferometer to project a mask plane profile on the metasurface from either side with suitable de-magnification ratios. Each imaging system consists of a tube lens ($L_1$ for the path of beam A and $L_2$ for the path of beam B in Fig. 2.17) and a 50× infinity-corrected objective of 0.8 numerical aperture (NA) and 4 mm focal length (1 mm working distance). The binary masks that impose the structured intensity profiles are placed at the rear focal plane of the tube lens of each path and the metasurface plane is equidistant from both objectives (based on their focal length). The distance from the pupil entrance of each objective to the tube lens is not affecting the performance of the imaging system in an infinity-corrected system (aberrations are introduced when this distance becomes significantly larger than the tube lens focal length). The de-magnification ratio of such imaging system is defined by the ratio of the objective focal length to the tube lens focal length (e.g. 100× demagnification for 400 mm tube lens focal length). Different magnifications are used throughout the experimental demonstrations, hence tube lens focal lengths will be given separately for each case. The overall coherent response is projected via the combination of the objective of beam path B and the tube lens $L_3$, which has a fixed focal length of 200 mm (resulting in 50× magnification), on a Charge Coupled Device (CCD) sensor and monitored in real time (the specifications of the CCD will be given separately for each demonstration as different sensors have been used). At this point it should be underlined that $x$, $y$ and $z$-axis alignment should be preserved across the system in order to preserve the coherent operation and standing wave formation throughout the system. Moreover,

simultaneous focusing of all imaging systems is required without disruption of the desired magnification ratios. In order to comply with these rather challenging restrictions, kinematic mounts are used in conjunction with the system's objectives as well as the metasurface sample holder and the binary masks.

Finally, a 735 nm Light Emitting Diode (LED) is used to illuminate the sample during imaging of the sample surface onto the CCD to ensure operation on the structured sample area. In order to avoid alignment and stability issues, the imaging and focusing parts of the system have been assembled in a cage configuration and enclosed in a box. It should be noted that a special sample holder was designed and fabricated with a milling machine for mounting the metasurface between the tight foci of the objectives, with minimum disruption of the cage system while still compatible with $x$-, $y$- and $z$-translation capability (sample holder mounted on an $x$-, $y$- and $z$-translation cube), see Fig. 2.18.

## 2.5 Summary

In this Chapter, the theoretical framework of coherently controlled thin films and metasurface functionalities has been defined and the mathematical description of metasurface coherent absorption has been presented. The theoretical model has been complemented by a detailed 3D simulation study to identify the ideal metasurface absorber realized by a free-standing gold film perforated with an array of Asymmetrically Split Ring slits. Subsequently, the numerical analysis of coherent control of absorption has been expanded in two spatial dimensions. The optimized metasurface absorber was examined under spatially varying illumination and simulations revealed that any induced inter-meta-molecular coupling effects do not exceed the diffraction limit of the optical system and therefore do not compromise the resolution of the spatially addressable coherent control scheme. In the second part of the Chapter, the methods that were employed throughout experimental demonstrations were described, including metasurface nanofabrication, characterization, mask fabrication techniques as well as a detailed description of the optical system that was built and used for all major experimental demonstrations throughout this thesis.

# Chapter 3

# All-optical logic and demultiplexing based on coherent perfect absorption

*The work in this Chapter has been partially published in [124, 125] and Figs. 1-3 of [124] and Figs. 1,3-5 of [125] are reproduced here.*

## 3.1 Introduction

Encoding, transmitting and processing information in the spatial domain is anticipated to be the next breakthrough in the hunt for technologies that will overcome the forthcoming capacity crunch [126, 127]. However, in order to harvest the inherent spatial parallelism of photonics technologies, new data processing schemes based on all-optical wavefront control are required.

Virtually every optical system relies on control over light propagation by modifying the phase or intensity across a beam of light. Lenses, prisms, gratings and transformation optics devices [128] such as optical cloaks [129–131] all redirect light by engineering the spatial distribution of optical constants in two or three dimensions. Recently, several research groups demonstrated that the propagation direction of light can also be controlled by phase gradient metasurfaces, where spatially varying resonators on an interface scatter with different phases [61, 63, 70, 71, 132–135]. While these are powerful

solutions for static wavefront control, they cannot offer dynamic control over light propagation. Established solutions for dynamic wavefront control are either electro-optical spatial light modulators based on liquid crystals or digital micromirror devices [136–138], or all-optical devices based on holographic operations in nonlinear photorefractive media, which rely on microsecond- to second-scale nonlinear light-matter interactions in a volume medium [136, 139, 140].

This work introduces a fundamentally different approach to dynamic control of the wavefront of light with light that establishes a platform for all-optical logical computations and parallel signal processing for coherent photonic networks. The underpinning principle is based on coherent light-matter interaction and offers radical advantages. As explained in Chapter 2, manifestations of optical phenomena in traveling and standing waves are different: a thin film or metasurface may be placed at an electric field node or anti-node of the standing wave formed by counter-propagating coherent light beams, resulting in suppression or enhancement of the electric light-matter interaction, respectively (Fig. 1.6). This approach has been shown to allow modulation of intensity [28], propagation direction [104] and polarization [113] of light with high contrast, at THz bandwidth [108, 109] and with arbitrarily low intensity levels down to single photons [107].

The proof-of-principle demonstrations of this Chapter expand the principle of control of coherent interaction of optical beams on highly absorbing plasmonic metasurfaces to two spatial dimensions, thus establishing the framework for metamaterial-based ultrafast all-optical logic in two dimensions. Two-dimensional all-optical logical operations (AND, XOR, XNOR, OR) are performed experimentally and potential applications related to multichannel logic schemes for telecommunications are explored. In fact, the presented platform is an elementary version of an optical computer that has the main characteristics of a Turing machine. It takes data (two-dimensional signal profile) from one optical input and processes it using instructions (rules) taken from the second optical input (two-dimensional control profile). The metasurface acts as the processor that performs elementary logical functions. The optical data processor operates in an analogue, rather than a discrete, digital fashion. Moreover, this computer operates in the parallel regime handling the entire two-dimensional inputs at once. The approach is compatible with arbitrarily low intensity levels and with 100 THz bandwidth, thus promising new applications in space division multiplexing, adaptive optics, 2D binary

optical data processing, and reconfigurable optical devices.

## 3.2 All-optical logical operations in two dimensions

In the hunt for next-generation ultra-fast and energy-efficient data processing schemes, all-optical components have long been considered to be the obvious replacements of semiconductor-based electronics which suffer from increased interconnection delays and large heat generation. The key element to realize any optical function is the optical logic gate. Over the years, several optical logic gate configurations have been reported based on nonlinear optical elements [141], second-harmonic generation and parametric downconversion processes [142], semiconductor optical amplifiers [143], photonic crystals [144–146], interferometric architectures [147] and nano-scale plasmonic waveguides [148]. Most of these approaches involve slow and energy-demanding nonlinearities, lack multi-functional operation and are usually targeting a single data channel at a time. Here, the full potential of optical spatial parallelism is explored via wavefront control on a plasmonic metasurface leading to all-optical logic that is reconfigurable with light and - in principle - compatible with arbitrarily low intensities and ultrafast response times.

All-optical wavefront control is demonstrated by projecting two-dimensional signal profiles of modulated intensity onto opposite sides of an absorbing plasmonic metasurface using coherent light. By modulating the relative phase ($\Delta\varphi$) of the two beams, control of absorption of light, hence control of the wavefront, is achieved with spatial resolution. On this basis, Boolean logic operations can be performed in two dimensions.

Based on the theoretical description of coherent control of the expression of thin film absorption in Chapter 2, destructive interference of coherent counter-propagating electromagnetic waves of equal intensity will cancel the electric field interacting with a metasurface placed at a node of the standing wave. In contrast, constructive interference doubles the electric field interacting with a metasurface placed at an anti-node in comparison to illumination with a single beam. While absorption in metasurfaces illuminated by a single wave is limited to 50%, the interaction of two coherent waves allows absorption to be controlled continuously from 0% to 100% by changing the position of the metasurface relative to the standing wave.

At this point it is worth considering the interaction of coherent light waves on beam splitters, see Fig. 3.1. In general, beam splitters may be either lossless or lossy


| Lossless beam splitter | | | | | |
|---|---|---|---|---|---|
| $\Delta\varphi$ | 0 | $\pi/2$ | $\pi$ | $3\pi/2$ |
| $I_C$ | 1 | 2 | 1 | 0 |
| $I_D$ | 1 | 0 | 1 | 2 |

| Lossy beam splitter | | | | |
|---|---|---|---|---|
| $\Delta\varphi$ | 0 | $\pi/2$ | $\pi$ | $3\pi/2$ |
| $I_C$ | 0 | 0.5 | 1 | 0.5 |
| $I_D$ | 0 | 0.5 | 1 | 0.5 |

**Figure 3.1: Interaction of coherent beams on lossless and lossy beam-splitters.** The output intensities $I_C$ and $I_D$ depend on the relative beam phase difference $\Delta\varphi$ between the equal intensity input beams $I_A = I_B = 1$ on the beam splitter (BS), where the intensity $I_i$ corresponding to the electric field $\vec{E_i}$ is defined as $\vec{E_i}\vec{E_i^*}$. The lossless beam splitter provides 50% transmission and reflection of a single impinging beam, while for the lossy beam splitter, in the "ideal" case providing 50% single beam absorption and 25% single beam transmission and reflection each is considered.

and are fundamental components of many systems in both classical and quantum optics. Considering illumination by a single beam of light, the limiting case of an ideal lossless beam splitter is defined as an interface having 50% transmission and 50% reflection, and the limiting case of an ideal lossy beam splitter as an interface having 25% transmission, 25% reflection, and 50% absorption which is equivalent to the description of a *ideal thin absorber* given in Appendix A. It is important to underline the role of beam splitters in optics and to consider the distinction between lossless and lossy beam splitters in optical networks. Beam splitters are fundamental components of photonic systems, allowing optical information merging in a strictly defined fashion. In quantum optics, beam splitters serve as key components for linear optical quantum computing [149] and combine single photons into exotic N00N states [150]. Recently, exotic properties of lossy beam splitters, such as apparent nonlinear absorption [151], have attracted the attention of the nanophotonics community [107, 152]. As illustrated by Fig. 3.1, the interaction of two counter-propagating coherent beams of equal intensity on an "ideal" lossy beam splitter results in two output beams of equal intensity, as described in Chapter 2. In this case, the thin lossy beam splitter is realized by an absorptive metasurface. In contrast, a lossless beam splitter divides the power unevenly between the output channels. Therefore, the power in a given channel of a coherent optical network can double with every interaction on a lossless beam splitter. Such exponential

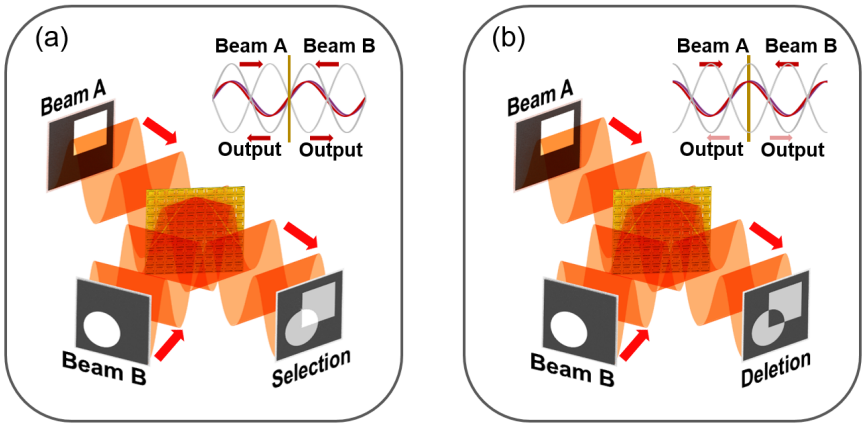


**Figure 3.2: Two-dimensional control of absorption of light with light.** Two-dimensional profiles A and B projected by coherent light onto an absorbing metasurface result in (**a**) selection (enhanced transmission) or (**b**) deletion (complete absorption) of intersecting wavefront areas, depending on the phase difference between intersecting beams.

growth that can concentrate the power of all input channels in a single output channel and cause equipment overload is impossible in a coherent network based on the "ideal" lossy beam splitter, for which the power in any output channel cannot exceed the single channel input power.

In this Chapter, the optical data processing capability of coherent control of an *ideal thin absorber* (or "ideal" lossy beam splitter), also known as coherent perfect absorber, realized by a metasurface is explored in the classical regime to access spatially selective modulation of absorption from 0% to 100%. The translation of the concept in two dimensions aiming at the demonstration of parallel all-optical logic is graphically illustrated in Fig. 3.2. In this representation, the structured intensity profiles of beams A and B carry the simple shapes of a square and a circle which partially overlap when projected on either side of the metasurface. Across areas of spatial overlap, beams A and B coherently interact with the metasurface and their relative phase difference $\Delta\varphi$ defines the level of coherent absorption exhibited by the intersecting wavefront areas from 0% to 100% leading to their unperturbed and enhanced transmission relative to the non-intersecting areas (Fig. 3.2 a), or their complete deletion from the outgoing wavefront (Fig. 3.2 b), respectively.

More specifically, the outgoing wavefront intensity levels across overlapping areas of beams A and B are given by Eqs. 2.10 - 2.11 for $s(\lambda) = -0.5$:

$$I_C = I_D = (I_A + I_B - 2\sqrt{I_A I_B}\cos\Delta\varphi)/4, \tag{3.1}$$

where $I_i = \overrightarrow{\boldsymbol{E_i}}\overrightarrow{\boldsymbol{E_i^*}}$. While absorption of 100% for $\Delta\varphi = 0$ and 0% for $\Delta\varphi = \pi$ requires $I_A = I_B$, tolerance towards input intensity differences is large, e.g., if one input intensity is twice as large as the other the absorption levels only change marginally to 97% and 3%, respectively. Consequently, the overlapping wavefront area output intensities depend on whether beams A and B are switched on or off, for given phases $\Delta\varphi$, which enables all-optical input-output relations that are analogous to Boolean logic operations.

For $\Delta\varphi = \pi$ this corresponds to the truth table of the logical operation A AND B, with an intensity threshold between 0.25 and 1 separating logical "0" and logical "1":

**Table 3.1:** Logical operation A AND B based on Eq. 3.1.

| Input Intensities | | Output intensities (for $\Delta\varphi = \pi$) |
|---|---|---|
| $I_A$ | $I_B$ | $I_C = I_D$ |
| 1 | 1 | 1 |
| 1 | 0 | 0.25 |
| 0 | 1 | 0.25 |
| 0 | 0 | 0 |

Similarly, $\Delta\varphi = 0$ corresponds to the truth table of A XOR B (or NOT A if $I_B = 1$ is fixed) with an intensity threshold between 0 and 0.25:

**Table 3.2:** Logical operation A XOR B based on Eq. 3.1.

| Input Intensities | | Output intensities (for $\Delta\varphi = 0$) |
|---|---|---|
| $I_A$ | $I_B$ | $I_C = I_D$ |
| 1 | 1 | 0 |
| 1 | 0 | 0.25 |
| 0 | 1 | 0.25 |
| 0 | 0 | 0 |

And finally, $\Delta\varphi = \pm\pi/3$ corresponds to A OR B with an intensity threshold between 0 and 0.25:

**Table 3.3:** Logical operation A OR B based on Eq. 3.1.

| Input Intensities | | Output intensities (for $\Delta\varphi = \pm\pi/3$) |
|---|---|---|
| $I_A$ | $I_B$ | $I_C = I_D$ |
| 1 | 1 | 0.25 |
| 1 | 0 | 0.25 |
| 0 | 1 | 0.25 |
| 0 | 0 | 0 |

Ideal performance requires a metasurface of deeply sub-wavelength thickness that absorbs 50% of a single beam illuminating the structure. The fabricated 60-nm-thick free-standing gold metasurface with a split ring aperture unit cell which comprises the thin absorber employed throughout experimental demonstrations (see Fig. 2.14) provides an absorption resonance near the experimental wavelength of 785 nm provided by a fibre-coupled CW laser module. The laser output power is 6.7 mW and is attenuated to a few $\mu$W to avoid detector saturation. The nanostructure has an almost identical optical response for illumination of its front and rear sides and absorbs around 33% of a single illuminating beam, see Fig. 2.14.

The optical imaging interferometer presented in Fig. 2.17 hosts the first metasurface-based experimental demonstrations of all-optical Boolean logic operations reported here. The relative beam phase difference of the incoming counter-propagating beams is temporally controlled by a VLC and the resulting coherent effects are monitored by imaging the metasurface plane on a CCD camera (Photometrics Evolve 512) in the path of output beam C that is formed by transmission of beam A and reflection of beam B. It is noted that less-than-ideal absorption in the sample reduces the achievable level of coherent absorption and results in a difference between intensity levels in the output beams [113]. The small difference between experimental transmission and reflection levels is compensated for by adjusting the input intensities.

For the fundamental proof-of-principle demonstration of Boolean logic as described by Tables 3.1 - 3.3, the simple binary intensity profiles illustrated in Fig. 3.3 were chosen. Two circular apertures of 1.5 mm diameter were mechanically drilled in purpose-designed

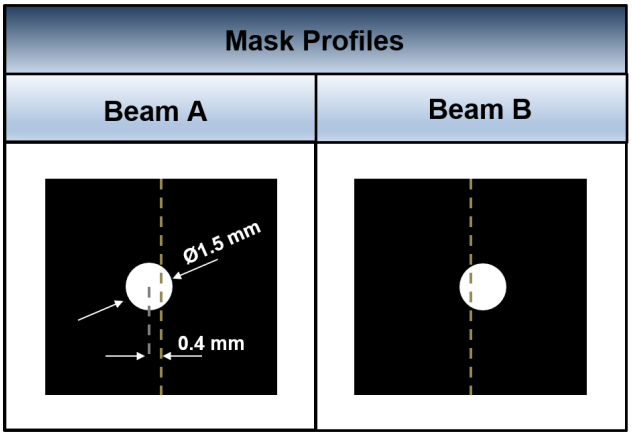


**Figure 3.3: Binary intensity mask designs for all-optical coherent Boolean logic demonstrations.** Intensity mask designs for structuring the profile of beams A and B which are subsequently projected onto the metasurface from either side.

cage-compatible aluminium mask templates based on the mask fabrication technique described in Section 2.3. The centres of the apertures designed for structuring the intensity profiles of beam A and beam B were 0.8 mm apart in the horizontal direction (0.4 mm to the left and right of the centre of the mask, respectively). In this way, the partially overlapping circular intensity profiles of beams A and B, create a Venn-like pattern on the metasurface plane (parts of the metasurface area are illuminated by beam A only, beam B only and beam A and B concurrently) that is used to examine the Boolean logic operation capability of the experimental platform. The fabricated masks are positioned on the prescribed mask planes of Fig. 2.17 and are projected on the metasurface with 100× demagnification ratio provided by the combination of a 50× infinity-corrected objective with a 400 mm focal length tube lens on either side.

Fig. 3.4 illustrates the experimental results for two-dimensional control of light with light on the metasurface for the simplest possible case of two partially overlapping illuminating circular beams, A and B (Fig. 3.4 a and b), realized by imaging the intensity profiles imposed by the two fabricated metallic masks described in Fig. 3.3 onto opposite sides of the metasurface. Across areas of overlapping illuminating beams, the detected intensity depends dramatically on the relative phase difference between the incident waves. Noting that intensities of incoherent beams would simply add up, the results reveal that illumination with a second coherent illuminating beam leads to a range of output intensities from four-fold increase to almost complete suppression.

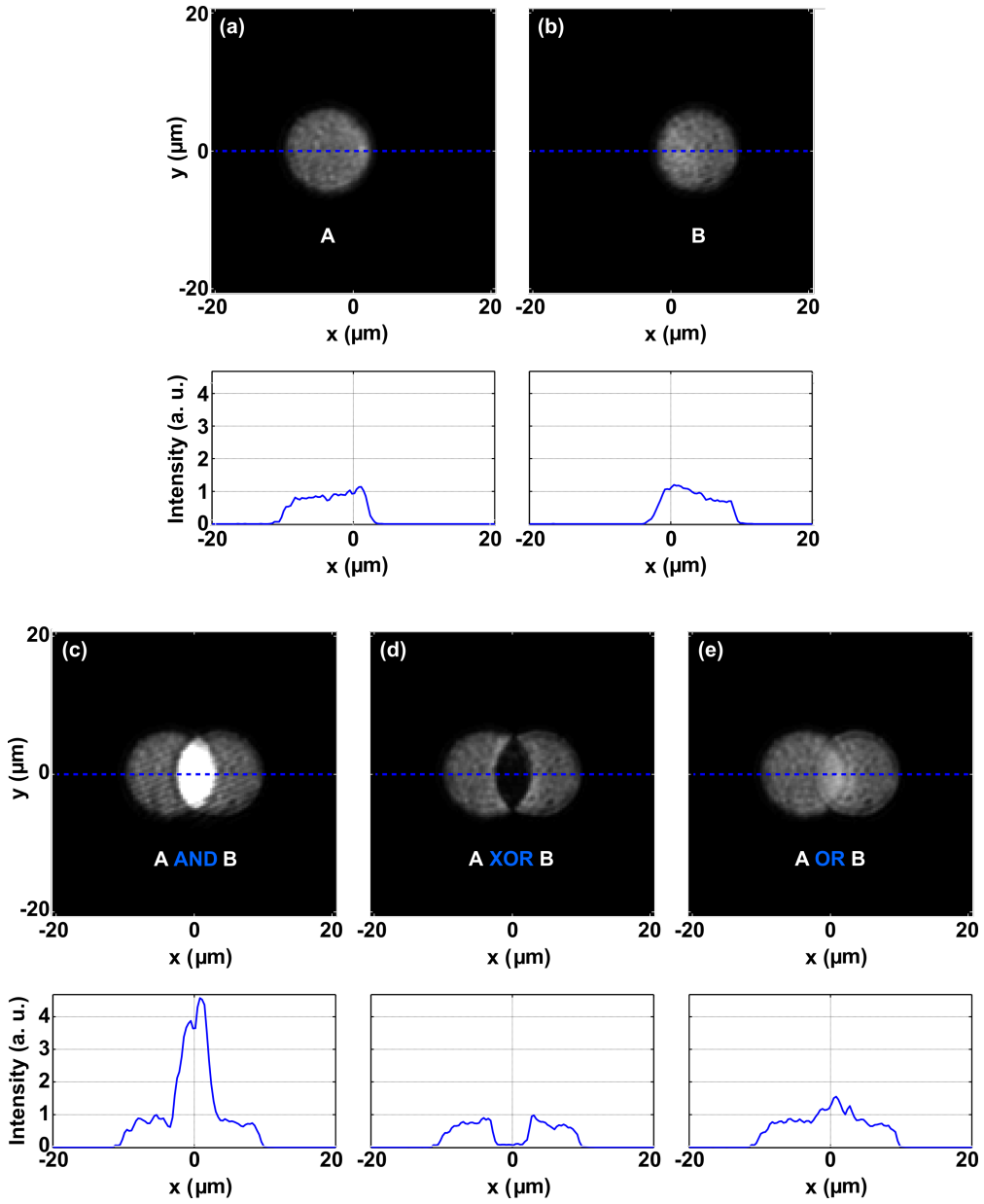


**Figure 3.4: Two-dimensional all-optical coherent logical operations.** Images of the metasurface illuminated by (**a**) beam A only, (**b**) beam B only, and (**c** - **e**) both beams A and B. Different relative phases of beams A and B correspond to different logical operations: (**c**) A AND B, (**d**) A XOR B, (**e**) A OR B. Graphs show the intensity cross-section along the corresponding dashed blue line. Intensity levels are shown on the same grayscale for all images and on the same vertical scale for all graphs.

The coherently enhanced output intensity (Fig. 3.4 c) corresponds to a reduced light-matter interaction and thus reduced absorption at the standing wave's electric node. On the other hand, changing the phase of one illuminating beam by $\pi$ translates the standing wave, placing the metasurface at an electric anti-node, where almost complete

suppression of the detected output intensity occurs as a result of enhanced light-matter interaction and therefore enhanced absorption (Fig. 3.4 d). Intermediate phases can in principle lead to the full range of intermediate intensities, e.g. the A OR B operation (Fig. 3.4 e). This is the first experimental proof of metasurface-based all-optical two-dimensional logical computations. Taking into account the compatibility of the underpinning principle with arbitrarily low intensities [107] and ultrafast response times [108, 109], the introduced platform could comprise a prime candidate for all-optical data and channel processing for telecommunications coherent networks as will be explained in the following sections.

## 3.3 Towards multichannel logic for telecommunications

The exponential growth of telecommunications bandwidth will require next generation optical networks, where multiple spatial information channels will be transmitted in parallel. Research advances in the field of multi-core and multi-mode fiber design and fabrication have flourished over the past few years, providing numerous efficient routes to data transfer in spatially multiplexed channels [153–156]. To exploit the full potential and capacity increase that spatial optical parallelism could provide, fast and scalable multichannel solutions for processing of parallel optical data channels are needed. Established electronic solutions have high energy requirements and complexity as they require conversion between optical and electronic signals, while all-optical techniques enabled by photorefraction are slow. Recently, several metamaterial-based approaches to dynamic spatial control over optical signals have emerged [157–159], including all-optical ones [160], which create interesting possibilities. Current approaches for demultiplexing spatially multiplexed channels are based on free-space platforms with bulk optics [161], laser-engraved light guiding cores [162, 163], tapered claddings [164], integrated photonic platforms [165, 166] and super-symmetric mode converters [167].

Here, an alternative metasurface-based approach is introduced for separating parallel spatially multiplexed channels that could work with single photons [107] and 100 THz bandwidth [108, 109]. All-optical logical operations between pairs of simulated spatially multiplexed information channels are experimentally demonstrated using the coherent interaction of light with light on a plasmonic metamaterial. The approach translates

the potential of all-optical logical operations in two dimensions (presented in the previous section) to the manipulation of spatially multiplexed channels which are suitable for fiber implementation and thus promise ultrafast, low-power solutions for all-optical parallel data processing across coherent photonic and telecommunication networks.

In the proposed approach, spatially selective absorption of light is applied to simple representations of spatially multiplexed signals in free-space, demonstrating all-optical Boolean logic operations between such information channels. Essentially, the paradigm of all-optical Boolean logic in the form of Venn patterns (as introduced in the previous section) is employed to enable manipulation of signals with spatially encoded information. In contrast to nonlinear techniques in general, this approach is linear and therefore does not have fundamental minimum intensity requirements. Moreover, the scheme could be implemented in a multi-core fiber network and extended to additional degrees of control since interaction of coherent waves on metamaterials also allows the polarization [113] and propagation direction [104] of optical signals to be modulated at single-photon intensity levels [107].

### 3.3.1 Logical operations between intensity- and phase-modulated channels

All-optical logical operations result from combining coherent optical channels on the absorbing plasmonic metasurface and externally controlling their relative phase difference in order to influence how signals in the data channels modulate the absorption characteristics of the metasurface absorber. The description of modulated absorption must take into account the phase difference between the interacting channels as well as any phase modulation used to encode information within the channels, as information is usually encoded in the phase of telecommunications channels. Thus, the total phase difference $\varphi_{\text{total}}$ that controls metasurface absorption is the sum of the externally imposed channel phase difference $\Delta\varphi$ and — depending on the digital modulation scheme — any phase difference $\varphi_{\text{data}}$ between the interacting data bits from each channel, $\varphi_{\text{total}} = \Delta\varphi + \varphi_{\text{data}}$. Therefore, Eq. 3.1 becomes:

$$I_C = I_D = (I_A + I_B - 2\sqrt{I_A I_B}\cos\varphi_{\text{total}})/4 \tag{3.2}$$

**Table 3.4:** Logical operations between equal intensity phase-modulated data streams A and B ($I_A = I_B = 1$) according to Eq. 3.2

| Input states | | Output intensities $I_C = I_D$ | |
|---|---|---|---|
| | | $\Delta\varphi = 0$ | $\Delta\varphi = \pi$ |
| A | B | A XOR B | A XNOR B |
| + | + | 0 | 1 |
| + | - | 1 | 0 |
| - | + | 1 | 0 |
| - | - | 0 | 1 |

If both interacting channel waves are in phase on the absorber ($\varphi_{\text{total}} = 0$), constructive interference of electric field leads to absorption of the bit. In contrast, a phase difference $\varphi_{\text{total}} = \pi$ between the channel waves results in destructive interference that renders the absorber transparent for the bit.

Consider a pair of interacting channels A and B that carry different coherent data streams using binary phase-shift keying (PSK). We denote the binary states that have the same intensity and a phase difference of $\pi$ by "+" and "-". In-phase interaction of both phase-modulated data streams on the absorber ($\Delta\varphi = 0$) will result in lossless transmission of opposite bits ($\varphi_{\text{data}} = \pi$) which will destructively interfere on the metasurface ($\varphi_{\text{total}} = \pi$) and absorption for identical bits ($\varphi_{\text{data}} = 0$), which interfere constructively on the metasurface ($\varphi_{\text{total}} = 0$). The result is an intensity-modulated channel corresponding to A XOR B, where high intensity corresponds to a logical "1" and low intensity corresponds to a logical "0", see Table 3.4. The inverse logical operation can be realized by applying a constant phase shift of $\Delta\varphi = \pi$ between channels, which eliminates the absorption of identical bits, while opposite bits are absorbed as the phase shift will result in their in-phase interaction with the absorber. The result is an intensity-modulated data stream A XNOR B. Furthermore, the inverse and identity operations can be realized by using the unmodulated carrier as channel B (e.g. corresponding to a fixed "+" state, see first and third row of Table 3.4) and setting the phase shift between channels A and B to be either $\Delta\varphi = 0$ or $\pi$, resulting in conversion of the phase-modulated data stream A into an intensity-modulated data stream NOT A or A, respectively.

Similarly, elementary coherent logical operations can also be realized between coherent intensity-modulated channels [115]. In this case, the phase difference $\varphi_{\text{total}}$ between waves interacting on the metasurface is the phase $\Delta\varphi$ that is externally imposed between the channels, $\varphi_{\text{total}} = \Delta\varphi$ (as $\varphi_{\text{data}} = 0$ in all cases), and sets the logical operation to be

**Table 3.5:** Logical operations between in-phase ($\varphi_{\text{data}} = 0$) intensity-modulated data streams A and B according to Eq. 3.2

| Input states | | Output intensities $I_C = I_D$ | | |
|---|---|---|---|---|
| | | $\Delta\varphi = \pi$ | $\Delta\varphi = 0$ | $\Delta\varphi = \pm\pi/3$ |
| A=$I_A$ | B=$I_B$ | A AND B | A XOR B | A OR B |
| 1 | 1 | 1 | 0 | 0.25 |
| 1 | 0 | 0.25 | 0.25 | 0.25 |
| 0 | 1 | 0.25 | 0.25 | 0.25 |
| 0 | 0 | 0 | 0 | 0 |

performed. When the input channel intensities are both zero, the output channel will of course also be zero, while for absorber illumination by a single input channel of intensity 1, the detected intensity will be 0.25 for an ideal planar absorber which will transmit as well as reflect 25% of the incident intensity. However, for simultaneous illumination by both input channels, the detected channel intensity will be strongly phase-dependent, due to perfect absorption for $\Delta\varphi = 0$ , transparency for $\Delta\varphi = \pi$ and partial absorption at intermediate phases. By selecting the correct external phase, a range of logical operations can be achieved. The resulting output channel intensities are listed in Table 3.5 and correspond to logical operations A XOR B when $\Delta\varphi$ is chosen to be 0 and the threshold is chosen to be a value between 0 and 0.25, A AND B ($\Delta\varphi = \pi$, threshold $> 0.25$) and A OR B ($\Delta\varphi = \pi/3$, threshold $< 0.25$), where the suitably chosen threshold intensity separates the logical "1" and "0" states. The multichannel logic for intensity-modulated channels is identical to the description of all-optical logic given in the previous section and Table 3.5 essentially summarizes Tables 3.1 - 3.3. Real applications may require a further 4× amplification step following the XOR and OR operations to restore the original signal level and to avoid different threshold intensities. An inversion, NOT A, for an intensity-modulated channel A can also be realized for $\Delta\varphi = 0$ by keeping the B-channel switched on.

### 3.3.2 Logic and demultiplexing with spatially multiplexed channels

In this proof-of-principle experimental demonstration simple binary intensity profiles are employed to simulate spatially multiplexed signals. A signal is considered to be composed of 5 spatially separated circular intensity lobes that could represent separate information channels running along a multi-core fiber, see Fig. 3.5 a. These are combined with a second set of optical channels on the metamaterial, i.e. Fig. 3.5 b - d,

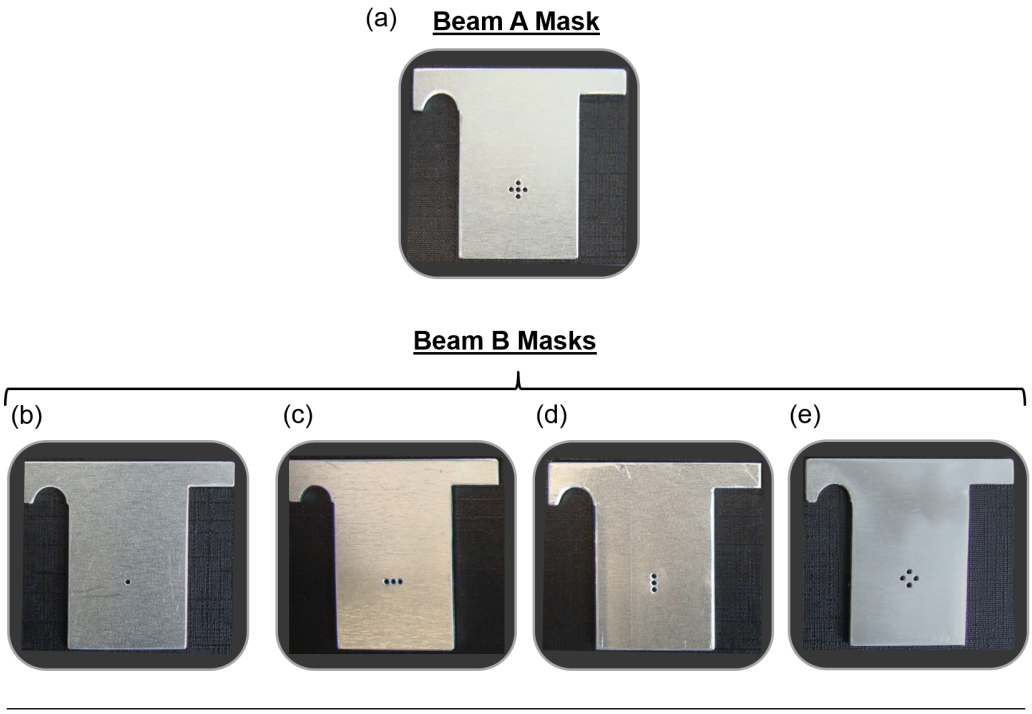


**Figure 3.5: Binary intensity masks for spatially multiplexed channel signals.** Fabricated 30 mm cage-compatible aluminium mask templates with drilled apertures of 0.9 mm diameter. (**a**) Mask for structuring the intensity of beam A to form 5 identical spatially separated channels. The intensity profile of beam B is shaped in order to address 4 different channel combinations corresponding to (**b**) 1 central, (**c**) 3 horizontal, (**d**) 3 vertical and (**e**) 4 peripheral channels of beam A. For all cases the aperture centre to centre distance in the horizontal and vertical directions is 1.3 mm. All masks were fabricated with mechanical milling and drilling as described in Section 2.3 and subsequently painted black to avoid unwanted reflections (presented here before painting for illustration purposes).

to demonstrate selective logical operations on different combinations of the signal's information channels. Spatial information channels resembling those of multi-core fibers are represented by apertures made by drilling holes of 0.9 mm diameter in 1 mm-thick aluminium specially made mask templates as described in Section 2.3. The masks are positioned on the back focal plane of the imaging optics in the paths of beam A and beam B, aligned, and imaged onto both sides of the metasurface in the experimental setup shown by Fig. 2.17 with the specifications defined in Section 3.2.

Fig. 3.6 illustrates logical operations for 1 out of 5 spatial channels of beam A (Fig. 3.6 a) with 1 channel of beam B corresponding to the central lobe (Fig. 3.6 b). Setting the total relative phase difference $\varphi_{\text{total}} = \pi$ the spatially addressable central channel lobe is transmitted unaffected to the system output (Fig. 3.6 c) as this case

corresponds to *coherent perfect transparency* of the metasurface due to destructive interference of the incident waves. In the formulation of multichannel logic as described by Tables 3.4 and 3.5, the case $\varphi_{\text{total}} = \pi$ corresponds to transmission of opposite phase-modulated bits in an XOR operation, transmission of equal phase-modulated bits in an XNOR operation and transmission of intensity-modulated bits in an operation 1 AND 1, for appropriately set channel phases. In contrast, when $\varphi_{\text{total}} = 0$ the central lobe will exhibit enhanced absorption (*coherent perfect absorption* case of the underpinning principle) and will be deleted from the system output (Fig. 3.6 d). The case of ($\varphi_{\text{total}} = 0$) corresponds to absorption of equal phase-modulated bits in an XOR operation, absorption of opposite phase-modulated bits in an XNOR operation and absorption of intensity-modulated bits in an operation 1 XOR 1, for appropriately set channel phases. In comparison to the peripheral channels that were not addressed, the detected intensity of the central channel is approximately four-fold increased in the metasurface's transparent state and negligible in its absorbing state (Fig. 3.6 e). Logical operations on the central channel do not affect the peripheral channels.

Fig. 3.7 shows — for the same set of 5 A-channels (first column) — how different combinations of B-channels (second column) can be used to perform the same logical operations (third and fourth columns) on corresponding combinations of information channels (panels a - c). No evidence of cross-talk between neighbouring channels has been observed, indicating that the spatial channels are sufficiently well separated to ensure that logical operations between pairs of A- and B-channels are not affected by their neighbours.

In this proof-of-principle demonstration, B-channels are selected with an intensity mask and their phase is modulated by the same phase modulator. In applications, it would be desirable to control the phase of each B-channel independently. This would allow prescription of different logical operations to each pair of data channels, which could then be switched dynamically. Independent phase control over each B-channel would also enable spatial demultiplexing of arbitrary combinations of information channels. To achieve this, information channels containing the same data stream would be combined on the absorbing thin film, where a constant phase difference $\Delta\varphi = \pi$ would be applied to eliminate absorption of wanted information channels, while a phase difference of $\Delta\varphi = 0$ would be set for the unwanted channels, resulting in their complete absorption.

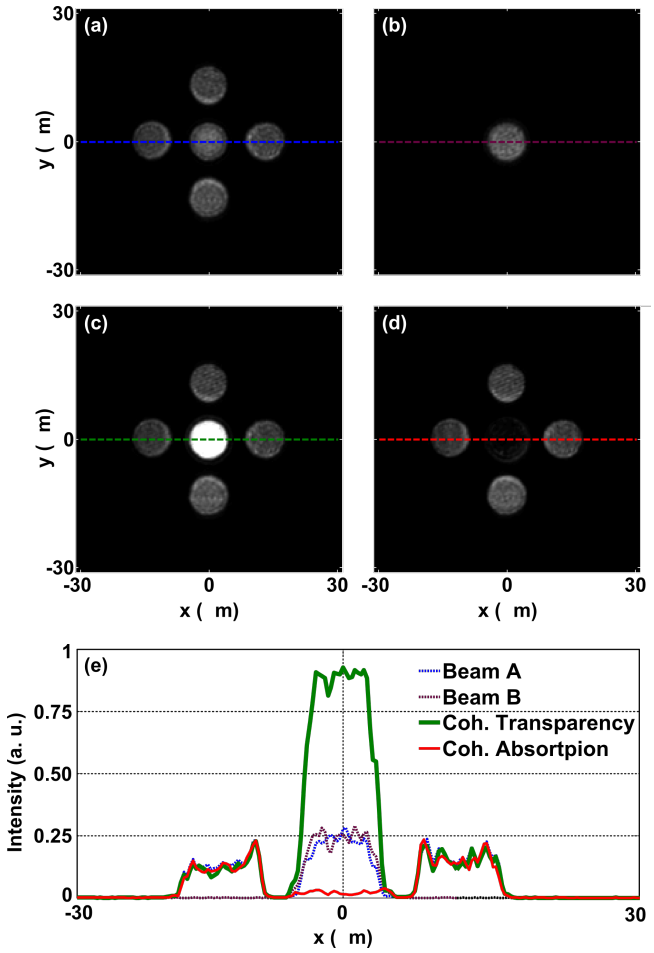


**Figure 3.6: Coherent logic with the central channel.** Images of the metasurface illuminated by (**a**) a 5-channel signal as beam A (beam B blocked), (**b**) the central channel as beam B (beam A blocked), (**c**) beams A and B with destructive interference on the metasurface corresponding to logical operations + XOR -, - XOR +, + XNOR +, - XNOR - of Table 3.4 and 1 AND 1 of Table 3.5 for the central channel, (**d**) beams A and B with constructive interference on the metasurface corresponding to logical operations + XOR +, - XOR -, + XNOR -, - XNOR + of Table 3.4 and 1 XOR 1 of Table 3.5 for the central channel. (**e**) Intensity cross-sections along the coloured dashed lines of images **a** - **d**. All images show intensity on the same grayscale.

It is important to consider the fundamental energy costs associated with the logical operations and demultiplexing applications discussed above. Spatial demultiplexing and logical operations that convert phase-modulated data into intensity-modulated data — XOR, XNOR, NOT and identity, see Table 3.4 – exploit *coherent perfect transparency* to achieve a logical "1" and *coherent perfect absorption* to achieve a logical "0", with about 17 dB contrast in the presented experiments. There are no unwanted losses in this case. The energy costs associated with logical operations on intensity-modulated

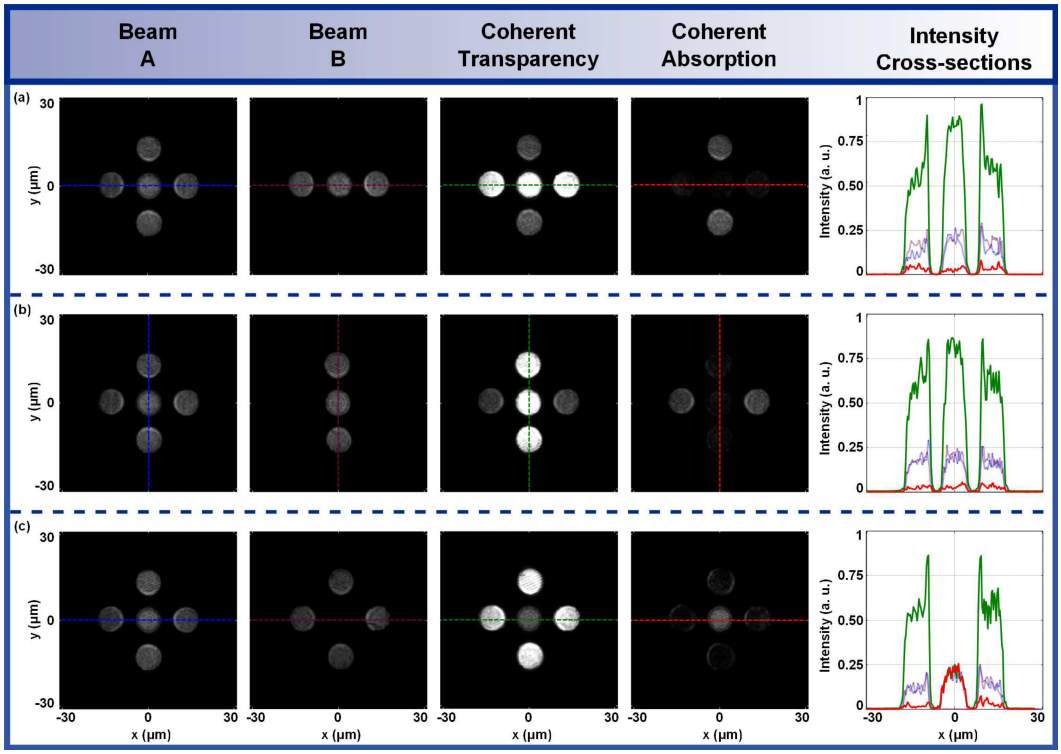


**Figure 3.7: All-optical multichannel logic operations.** Images of a metasurface illuminated by a 5-channel signal as beam A (first column) and beams B (second column) corresponding to (**a**) the horizontal, (**b**) vertical and (**c**) peripheral channels. The third and fourth columns correspond to destructive (coherent transparency) and constructive (coherent absorption) interference of beams A and B on the metasurface, respectively. For phase-modulated optical signals (Table 3.4), the third (fourth) column corresponds to the XOR operation between opposite (same) phase states in the selected channels. For intensity-modulated signals (Table 3.5), the third column corresponds to the AND operation, while the fourth column corresponds to the XOR operation. The relative mask alignment is adjusted for each pair of beams A and B. An intensity reduction towards the outer edge of the channel patterns is caused by the Gaussian intensity profile of the beams illuminating the masks. All images show intensity on the same grayscale and the last column shows intensity cross-sections along the dashed lines in the images of the same row using corresponding colours.

data — as shown by Table 3.5 – are less favorable. The XOR and NOT operations achieve 11 dB experimental contrast, while the contrast of the OR operation is only limited by background noise. However, XOR, NOT and OR suffer from 6 dB loss arising from partial absorption of a single input channel. These losses could be reduced to 3 dB by combining the identical output channels C and D and fully compensated by amplification. The AND operation yields a logical "1" (theoretically without any loss) based on *coherent perfect transparency*, however, imperfect absorption of a single light beam limits the intensity contrast between the "0" and "1" states to 6 dB. The solution

of channel recombination and signal regeneration/amplification becomes crucial in the case of a signal processing network of many interconnected logic gates where universal intensity thresholds for logical "0" and "1" must apply throughout the network.

Looking towards implementation of logical operations and demultiplexing in real telecommunications systems, it is noted that the spectral position of the metamaterial's bands of operation (absorption bands) approximately scales with the size of its unit cell and with the refractive index of the metamaterial's environment. The fabricated metasurface has absorption bands around 875 nm and 1850 nm wavelength. Thus, a 20% smaller metamaterial structure may be expected to come close to the ideal 50% absorption in the telecommunications band around 1550 nm wavelength, while the existing metamaterial design surrounded by glass (at the interface between two optical fibers) should perform well in the 1310 nm telecommunications band. It is anticipated that any implementations would either involve metamaterial fabrication on optical fiber end faces or encapsulated units with fiber connectors containing lenses that image the fiber output onto a metamaterial. The simulated optical channels investigated here have a diameter of about 9 $\mu$m on the metamaterial, which is comparable to typical optical fiber cores. The channel pitch of about 13 $\mu$m would need to be increased for typical multi-core fibers that have a core pitch of several 10s of $\mu$m. Absence of cross-talk between realistically sized channels with comparatively small spacing indicates that cross-talk between channels will not be an issue for coherent all-optical data processing in multi-core fiber systems. The channels remain well-separated with clearly defined edges, indicating absence of long-range coupling between the split ring apertures of the plasmonic metamaterial. Cross-talk between even more closely packed channels or overlapping channels, as is the case in spatial mode multiplexing encoding schemes could be explored in future work. It is however expected, as explained in Section 2.2.2, that cross-talk issues may only arise if the distance of neighbouring channels is close to the diffraction limit of the employed imaging system or smaller than the cautiously estimated spatial resolution restriction from inter-meta-molecular coupling, which for this case is equal to two unit cells (700 nm).

The step from single-channel to multichannel logical operations as reported here is non-trivial and technically demanding. Single-channel logical operations can be realized through interaction of two counter-propagating coherent plane waves on a small absorber. In contrast, our implementation of multichannel logical operations engages

waves with a continuous spectrum of wave vectors for imaging of multiple channels onto a much larger metasurface area. As coherent absorption is controlled by the phase difference between A- and B-channels, phase distortions across all channels must be avoided. This requires flatness within 10s of nm and homogeneity of the plasmonic absorber and of all optical components across the area occupied by all channels, as well as precise alignment.

## 3.4 Summary

In this Chapter, the interaction of coherent waves with spatially modulated wavefronts was exploited in order to control the light-matter interaction on a lossy metasurface and thus perform elementary all-optical computations. Constructive interference at the metasurface led to enhanced light-matter interaction and therefore absorption, while destructive interference suppressed the interaction of light with absorbing matter. The metasurface essentially constitutes a functional lossy beam-splitter that can be reconfigured all-optically with spatial resolution.

In the constructed experimental platform, all-optical logical operations AND, XOR, OR were performed between partially overlapping, circular, counter-propagating coherent beams. These demonstrations essentially provide a representation of all-optical logic in terms of Venn-diagram set theory and constitute an all-optical version of a Turing machine.

On this basis, the coherent interaction of light with light on a lossy metasurface was used for dynamic selection and deletion of spatially distinct optical data channels, as well as elementary multichannel all-optical data processing. The demonstrated all-optical operations were applied to multiple channels leading to up to 17 dB experimental contrast between logical “1” and “0” for phase-modulated input channels and 6-11 dB experimental contrast for intensity-modulated input channels. The speed at which different logical operations can be set and channels selected is in principle determined by the response time of commercial phase modulators (10s of GHz). It has been shown in [108, 109] for similar arrays of asymmetrically split ring apertures in gold that the speed of the underlying coherent interaction is limited by the plasmon relaxation time to about 10 fs, which is about 3 orders of magnitude faster than telecommunications data rates that are on the order of 10s of Gbit/s per channel. Furthermore, the coherent effect is

compatible with arbitrarily low intensities [107]. The presented selective transmission or deletion of modes from multimode signals promises solutions for mode selection in spatial mode multiplexing for higher bandwidth optical telecommunications. Therefore, coherent control of light with light has potential applications in space division multiplexing and elementary all-optical data processing in coherent information networks. For example, the XOR operation is a vital component of many all-optical cryptography schemes [168, 169]. However, since the translation between the states of *coherent perfect transparency* and *coherent perfect absorption* requires phase stability, it may be challenging to apply to large-scale fibre networks, therefore the approach is more applicable to local systems and possibly on-chip integrated photonics implementations. Moreover, in order to go beyond simple single-step logical functions, cascading of multiple coherent all-optical logical operations will need to be explored. For this, the output of one logical operation will have to serve as the input of the next, which may require intermediate signal regeneration/amplification. The practical potential of the presented scheme is further reinforced by the fact that two-dimensional coherent control could provide a solution for spatially-resolved dynamic control over the expression of many properties of metasurfaces and thin films of sub-wavelength thickness, e.g. to control intensity [28], propagation direction [104] and polarization [113] of electromagnetic waves throughout the electromagnetic spectrum.

With femtosecond-scale response times, large optical contrast and quantum-level energy requirements, two-dimensional control of light with light has potential applications ranging from tuneable, reconfigurable and adaptive optical devices, as well as coherent image and video processing to massively parallel modulation and processing of optical data and all-optical computing. Such applications will be explored in the following Chapters.

# Chapter 4

# All-optical image processing and pattern recognition

*The work in this Chapter has been partially published in [124, 170] and Fig. 4 of [124] and Figs. 1-3 of [170] are reproduced here.*

## 4.1 Introduction

The ability to control the wavefront of light is fundamental to focusing and redistribution of light, enabling many applications from imaging to spectroscopy. Wave interaction on highly nonlinear photorefractive materials is essentially the only established technology allowing the dynamic control of the wavefront of a light beam with another beam of light, but it is slow and requires large optical power.

All-optical wavefront manipulation constitutes an inherently parallel optical technique and could efficiently address recognition, comparison and analysis of large patterns or images which are computationally intensive tasks as they rely on sequential electronic data processing. Therefore, the inherent parallelism of photonic systems has long been considered to be the route towards fast and energy efficient, real-time pattern recognition and image processing systems with reduced computational costs as compared to purely electronic solutions. Optical Fourier techniques and spatial light modulators, have been widely employed in image processing schemes intended for medical imaging [138, 171]. However, the ultimate potential of photonic systems is revealed when all-optical logic computations come into play [115, 124, 125, 143, 147]. All-optical pattern

recognition schemes have been realized with different types of optical correlators based on photorefractive polymers [172], semiconductor optical amplifiers [173], delay lines and phase shifter designs [174]. Photorefraction [175], phase-conjugation [176], second harmonic generation [177], vapour atomic transitions with 4-wave mixing [178], spatial dispersers [179] and reservoir computing [180] systems have served as the basis of reliable all-optical image processors. Nevertheless, the impact of these approaches is limited by complexity as well as fundamental speed restrictions and energy requirements due to the nonlinearities involved.

Two-dimensional control of a light beam with another beam of light has been achieved experimentally on a metasurface for the first time within the context of this thesis and presented in Chapter 3. Under this scheme, the absorption level introduced by a plasmonic metasurface is coherently controlled with spatial resolution. The technique can in principle operate in the quantum regime [107] with up to 100 THz bandwidth [108, 109]. The computational potential of this technique was revealed in Chapter 3 through the experimental realization of Boolean logic operations between counter-propagating beams carrying simply structured intensity profiles. The successful demonstrations of the technique acted as an inspiration to explore how efficiently this scheme can be applied to complex two-dimensional profiles targeting all-optical processing, analysis and recognition of images and patterns. In this Chapter, new routes to image and pattern analysis, processing and recognition are explored based on the new technology for two-dimensional control of light with light exploiting the coherent interaction of optical beams on highly absorbing plasmonic metasurfaces.

In particular, binary image analysis and pattern recognition are experimentally demonstrated based on the spatially resolved linear interaction of light with light on a plasmonic absorbing planar metamaterial. The International Year of Light logo is chosen for an initial demonstration of the image processing capability of the existing experimental platform. In the following experiments, similarities and differences between binary dot patterns are recognized and satellite images analyzed by projecting reference and test images onto opposite sides of the absorbing metasurface using coherent light. Quantitative measurements of image agreement and disagreement, and indeed of any set operation between the images, can be performed by imaging the metasurface plane onto a photodetector. This way, the relationship between any pair of binary images (containing a large amount of optical data) may be reduced all-optically to a total of

3 characteristic power values of electronic data. Furthermore, imaging onto a CCD camera reveals maps of similarities and differences. Lastly, the spatial resolution of the presented image processing platform is experimentally explored with the use of a sector star pattern. In contrast to methods based on slow and energy demanding nonlinearities and electronics, the proposed approach is based on linear optics and therefore it is, in principle, ultrafast with up to 100 THz bandwidth [108, 109] and compatible with arbitrarily low intensities down to single photons [107].

## 4.2 All-optical image processing

Recently, metamaterial and metasurface research has started to increasingly focus on analogue signal and image manipulation on a hardware level [181]. Metamaterial-based imagers have been reported for frequency-indexed computational imaging [182], acoustic sub-wavelength edge detection [183], aberration-free imaging [184] and Terahertz compressive imaging [185]. However, research on all-optical, software-free analysis and processing of images in the optical to near-infrared regime with metamaterials is still at its infancy. In this section, the first paradigm of metasurface-based image processing and manipulation is presented based on two-dimensional control of coherent absorption.

As discussed in Chapter 3, the coherently controlled interaction of partially overlapping beams A and B on the metasurface strongly resembles the associated Venn diagrams of set theory, see Fig. 3.4. In the experimental configuration of Fig. 2.17, variation of the relative beam phase difference between beams A and B via the phase retarding component (VLC) results in the performance of logical operations AND, XOR and OR across the intersecting areas of the incoming intensity-structured wavefronts of beams A and B. Thus, coherent control provides an all-optical way of performing logical operations, which may be applied to arbitrary combinations of images.

For the initial demonstration of all-optical image processing, the international Year of Light logo was imprinted on a photolithography-fabricated chromium-on-glass mask as explained in Section 2.3 and projected onto the metasurface using beam A by positioning the fabricated mask at the rear focal plane of the imaging optics of beam path A, see Fig. 2.17. Aiming to manipulate the central sun of the logo, a similar mask was fabricated for the path of beam B. Using the same experimental system setting as described in Section 3.2 (785 nm CW fibre-coupled laser module with 6.7 mW output

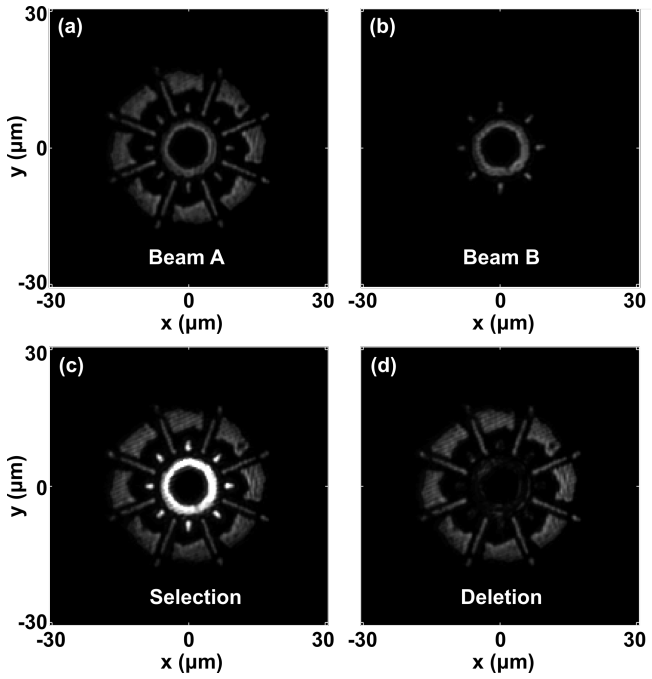


**Figure 4.1: Coherent image processing.** Images of the metasurface illuminated by (**a**) the International Year of Light logo (beam A) and (**b**) its central sun (beam B). Coherent (**c**) selection and (**d**) deletion of the sun within the logo for different relative phases of beam A and B corresponding to electric field nodes and anti-nodes of the standing wave, respectively.

power attenuated to a few $\mu$W, Photometrics Evolve 512 CCD camera and 100$\times$ demagnification realized by the combination of 50$\times$ objective with a 400 mm tube lens), image processing was attempted by two-dimensional control of metasurface absorption. This is illustrated by Fig. 4.1. Panels a and b depict the detected logo of the International Year of Light (beam A) and the sun that forms its center under single beam illumination, respectively. For simultaneous projection of both patterns onto the metasurface, reduced absorption near the electric field node of the standing wave results in four-fold enhancement or selection (recognition) of the logo's central sun, which both images have in common (panel c). On the other hand, a $\pi$ phase shift of one illuminating beam shifts the standing wave, placing the metasurface at an electric anti-node, where the sun is strongly absorbed and therefore deleted from the logo, leaving just the flags that are present in only one image (panel d). In this way, two-dimensional coherent control of light with light provides an all-optical method for image processing.

## 4.3 Set operations between images

The image processing demonstrations of Fig. 4.1 acted as an inspiration for establishing a concise formulation for the introduced image processing platform and exploring the potential computational functionalities that the technique may provide.

For this analysis two binary patterns, A and B, are considered to be projected by coherent light onto opposite sides of a thin film with intensity transmission and reflection coefficients, $T$ and $R$. The intensities of the illuminating light beams, $I_{\mathrm{A}}$ and $I_{\mathrm{B}}$, are chosen such that the transmitted beam A and the reflected beam B have the same intensity for single beam illumination, $I_{\mathrm{sgl}} = TI_{\mathrm{A}} = RI_{\mathrm{B}}$. Across areas of pattern overlap, constructive or destructive interference of the transmitted beam A and reflected beam B will lead to addition or cancellation of the corresponding fields depending on the phase difference between the illuminating light beams, where doubled field amplitudes correspond to an intensity of $4I_{\mathrm{sgl}}$ while field cancellation implies vanishing intensity. It follows that the similarity of two patterns can be quantified by measuring the phase-dependent overall power of the output beam with a photodetector. For binary reference and test images, A and B, with illuminated areas $S_{\mathrm{A}}$ and $S_{\mathrm{B}}$, respectively, similarities and differences can be characterized by the area $S_{\mathrm{A}\cap\mathrm{B}}$ that is illuminated by both images (agreement) and the area of $S_{\mathrm{A}\oplus\mathrm{B}}$ that is illuminated by only one image (disagreement). The area of disagreement will lead to detection of phase-independent power $I_{\mathrm{sgl}}S_{\mathrm{A}\oplus\mathrm{B}}$. In contrast, coherent interaction of light with light in areas illuminated from opposite sides yields detection of a phase-dependent power $4I_{\mathrm{sgl}}S_{\mathrm{A}\cap\mathrm{B}}\cos^2\frac{\theta}{2}$, where $\theta$ is the phase difference between the transmitted beam A and the reflected beam B. Therefore, the detected power is

$$P(\theta) = I_{\mathrm{sgl}}(S_{\mathrm{A}\oplus\mathrm{B}} + 4S_{\mathrm{A}\cap\mathrm{B}}\cos^2\tfrac{\theta}{2}), \tag{4.1}$$

where $\theta$ is proporational to the relative beam phase difference $\Delta\varphi$ of the input beams A and B. It is convenient to normalize the detected output power by $4P_{\mathrm{A,sgl}}$, where $P_{\mathrm{A,sgl}} = I_{\mathrm{sgl}}S_{\mathrm{A}}$ is the total detected output power when the metamaterial is illuminated by the reference image only. The normalized output power $\tilde{P}(\theta) = \frac{P(\theta)}{4P_{\mathrm{A,sgl}}}$ is

$$\tilde{P}(\theta) = \tfrac{S_{\mathrm{A}\oplus\mathrm{B}}}{4S_{\mathrm{A}}} + \tfrac{S_{\mathrm{A}\cap\mathrm{B}}}{S_{\mathrm{A}}}\cos^2\tfrac{\theta}{2} \tag{4.2}$$

Normalized in this way, the size of various characteristic areas of the images relative

**Table 4.1:** Set operations between images A and B based on photodetector measurements of maximum and minimum power, $P_{\max}$ and $P_{\min}$, normalized by the reference power $4P_{\mathrm{A,sgl}}$ (normalized power $\tilde{P}_{\max}$ and $\tilde{P}_{\min}$, their average $\tilde{P}_{\mathrm{avg}}$ and difference $\Delta\tilde{P}$).

| Area $[S_{\mathrm{A}}]$ | Power measurement |
|---|---|
| $S_{\mathrm{A}}$ | $1$ |
| $S_{\mathrm{B}}$ | $4\tilde{P}_{\mathrm{avg}} - 1$ |
| $S_{\mathrm{A}} + S_{\mathrm{B}}$ | $4\tilde{P}_{\mathrm{avg}}$ |
| $S_{\mathrm{A}\cap\mathrm{B}}$ | $\Delta\tilde{P}$ |
| $S_{\mathrm{A}\cup\mathrm{B}}$ | $4\tilde{P}_{\mathrm{avg}} - \Delta\tilde{P}$ |
| $S_{\mathrm{A}\oplus\mathrm{B}}$ | $4\tilde{P}_{\min}$ |
| $S_{\mathrm{A}\setminus\mathrm{B}}$ | $1 - \Delta\tilde{P}$ |
| $S_{\mathrm{B}\setminus\mathrm{A}}$ | $4\tilde{P}_{\mathrm{avg}} - 1 - \Delta\tilde{P}$ |

to the area $S_{\mathrm{A}}$ of the reference image can be easily determined with a photodetector by measuring only the maximum $\tilde{P}_{\max}$ and minimum $\tilde{P}_{\min}$ of the phase-dependent total power of one output beam. This is illustrated by Table 4.1 where $\tilde{P}_{\mathrm{avg}} = (\tilde{P}_{\max} + \tilde{P}_{\min})/2$ and $\Delta\tilde{P} = \tilde{P}_{\max} - \tilde{P}_{\min}$. In particular, the sum of the illuminated areas A and B corresponds to the average power, the differences between the binary images are given by the minimum power and the overlap between the images corresponds to the phase-dependent power fluctuations.

While the above holds for any thin film with intensity transmission and reflection coefficients, $T$ and $R$, it is interesting to consider the limiting cases of the ideal lossless beam splitter ($T = R = 50\%$) and the *ideal thin absorber* ($T = R = 25\%$). For coherent illumination with co-polarized counter-propagating light beams, $I_{\mathrm{A}} = I_{\mathrm{B}}$, the lossless beam splitter will split the incident intensity unevenly between the output beams, while the lossy beam splitter will split the incident intensity between absorption and two identical output beams. In the lossless case, coherent transparency at the standing wave node implies that the phase $\theta$ is related to the phase difference $\Delta\varphi$ between the waves incident on the beam splitter by $\theta = \Delta\varphi \pm \pi/2$. In the lossy case, vanishing intensity implies *coherent perfect absorption* which occurs when the *ideal thin absorber* is placed at an electric field anti-node of the standing wave formed by the incident waves, while the maximum output intensity corresponds to *coherent perfect transparency* occurring when *ideal thin absorber* is placed at a node where interaction with the wave is eliminated. For such a coherent perfect absorber, the phase $\theta$ is related to the phase difference $\Delta\varphi$ between the incident waves on the beam splitter by $\theta = \Delta\varphi + \pi$.

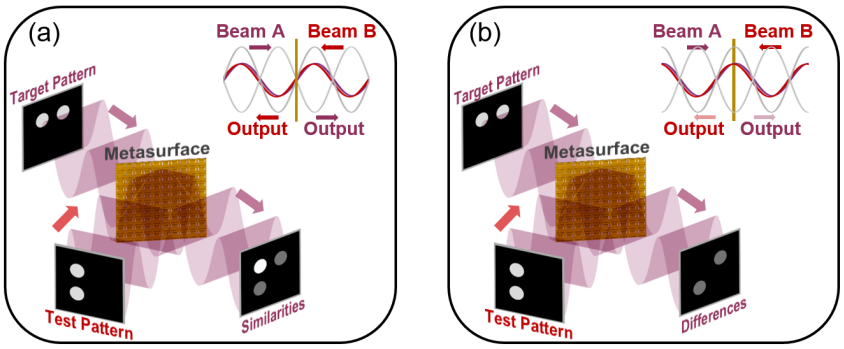


**Figure 4.2: All-optical metasurface-based pattern recognition concept.** For the limiting case of a metasurface that is an *ideal thin absorber*, standing wave translation between nodes (**a**) and anti-nodes (**b**) leads to similarity detection due to vanishing absorption and difference detection due to coherent perfect absorption, respectively, as illustrated by the insets.

## 4.4 Pattern recognition

The qualitative image processing of Section 4.2 along with the quantitative analysis of set operations between images with a simple photodetector of Section 4.3 were exploited to create the first all-optical platform for pattern recognition that does not involve slow and energy-demanding non-linearities or computationally intensive algorithms and post-processing schemes. In Fig. 4.2, the concepts of all-optical metasurface-based logic and two-dimensional wavefront control are brought together to highlight the similarities and differences between structured beams A and B which are composed of 2-dot vertically and horizontally arranged patterns. The single dot that is common between the two patterns is highlighted at nodes and deleted at anti-nodes, thus revealing the similarities (Fig. 4.2 a) and differences (Fig. 4.2 b) of patterns A and B based on *coherent perfect transparency* and *coherent perfect absorption*, respectively.

For the experimental realization of pattern recognition, patterns of 8 dots occupying 8 out of 16 positions in a 4 × 4 grid were designed and fabricated with photolithography resulting in the chromium-on-glass binary masks shown in Fig. 4.3. The pattern recognition strategy aims to experimentally compare a target pattern (Fig. 4.3 a) with a set of test patterns (Fig. 4.3 b - f) in order to qualitatively and quantitatively measure the degree of pattern agreement and identify the target pattern amongst the patterns under test. To this end, test patterns include patterns with increasing number of matching dots starting from 0 matching dots (Fig. 4.3 b) up to 8 out of 8 matching dots (Fig. 4.3 f)

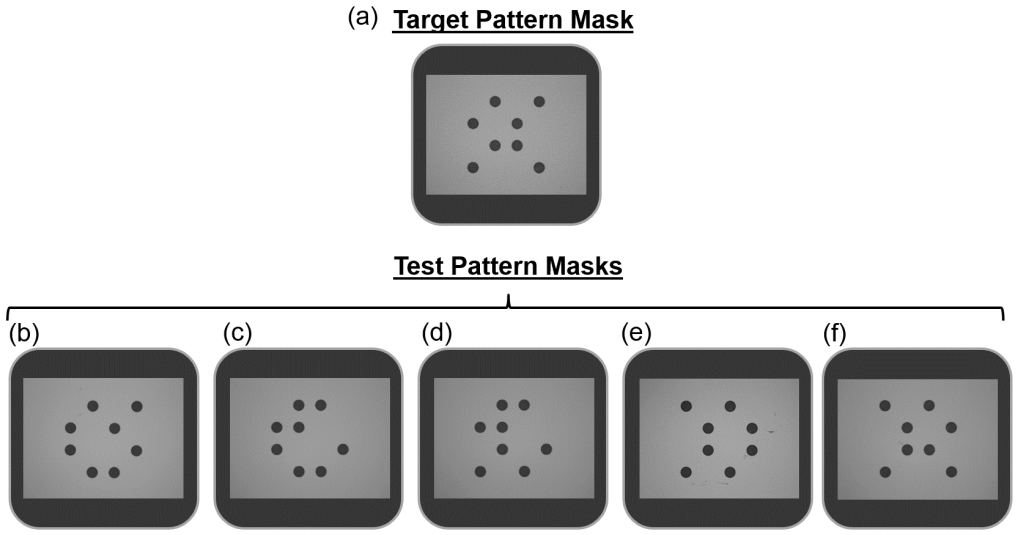


**Figure 4.3: Photolithography-fabricated binary masks for pattern recognition.** Optical microscope images of (**a**) target pattern and (**b**) - (**f**) test pattern masks. In each pattern 8 dots of 175 $\mu$m diameter are arranged in a 4 $\times$ 4 grid of 350 $\mu$m horizontal and vertical centre-to-centre spacing. Gray areas represent chromium-covered (opaque) mask areas and darker areas correspond to glass. Patters under test are horizontally inverted on the masks with respect to the target pattern in order to be projected on the metasurface with the correct orientation.

in steps of 2 (Fig. 4.3 c - e). It should be noted that for the counter-propagating beams A and B the prescribed binary intensity profiles should be horizontally inverted with respect to each other on the mask plane in order to be projected on the metasurface with matching orientation. Across all patterns, the dot diameter is constant and equal to 175 $\mu$m and the horizontal and vertical centre-to-centre dot spacing is 350 $\mu$m on the mask.

The reported proof-of-principle pattern recognition experiment is performed in the experimental platform of Fig. 2.17. The coherent source is a 790 nm fibre Bragg grating temperature-stabilised CW laser with 2 mW output power. The employed metasurface (see Fig. 2.14) has a broad absorption peak around 875 nm near the experimental wavelength of 790 nm for which 34% of a single incident beam gets absorbed. Thus, it is much closer to the limiting case of an *ideal thin absorber* than the case of a lossless beam splitter. Throughout all optical experiments, the metasurface was illuminated by linearly polarized light with the electric field oriented parallel to the symmetry axis of the split rings. Binary masks are positioned on the back focal plane of the imaging optics (50$\times$ infinity-corrected objective with 300 mm focal length tube lens resulting in 75$\times$

demagnification ratio from the mask plane to the metasurface plane) in beams A and B, aligned via rotation and kinematic mounts, and imaged onto both sides of the metamaterial. Alignment of target and test masks must be better than their characteristic feature size to ensure that the target and test patterns overlap on the metasurface and misalignments are easily noticeable on the camera image. Moreover, flatness and alignment of the metasurface with respect to beams A and B is also critically important to ensure a constant phase difference between beams A and B across the metasurface and misalignments are apparent as interference fringes on the camera image, which serves as a valuable alignment tool. While the approach will work at any intensity below damage thresholds, the laser light is attenuated to few $\mu$W to avoid detector saturation. The laser beam is split and propagates along paths A and B of matched lengths, forming a standing wave where the metasurface is illuminated from both sides. The resulting coherent effects are controlled by varying the relative beam phase difference via a liquid crystal phase retarder (VLC) and detected in the output beam formed by the transmitted beam A and the reflected beam B by imaging the metamaterial onto a CCD camera (Photometrics Evolve 512 CCD camera). The input beam intensities were chosen such that the single beam transmission of beam A and reflection of beam B have the same intensity.

Fig. 4.4 illustrates binary pattern recognition for patterns of bright dots occupying 8 positions in a $4 \times 4$ grid. These may be thought of as, for example, spatially multiplexed optical data, lottery tickets or multiple choice answer sheets. A target pattern (data, winning ticket or answer sheet) is compared with test patterns with zero, 25%, 50%, 75% and full agreement (row 1) by projection onto the metasurface as described above. Across areas of pattern mismatch there is no coherent interaction and therefore the detected intensity $I_{\mathrm{sgl}}$ is constant. In contrast, across areas of pattern agreement, coherent interaction between beams A and B on the planar metamaterial causes the detected intensity to oscillate between $4I_{\mathrm{sgl}}$ (row 2, $\theta = 0$) and 0 (row 3, $\theta = \pi$) as a function of the phase difference between beams A and B on the metasurface. As a result, areas of agreement are highlighted in row 2, while they are deleted in row 3, thus revealing areas of agreement (similarities) and disagreement (differences), respectively.

Direct quantitative comparison of the images is most easily achieved by detecting the total power of the output beam with a photodetector. Here, the CCD is used as an effective photodetector by integrating the total power in each acquired image.

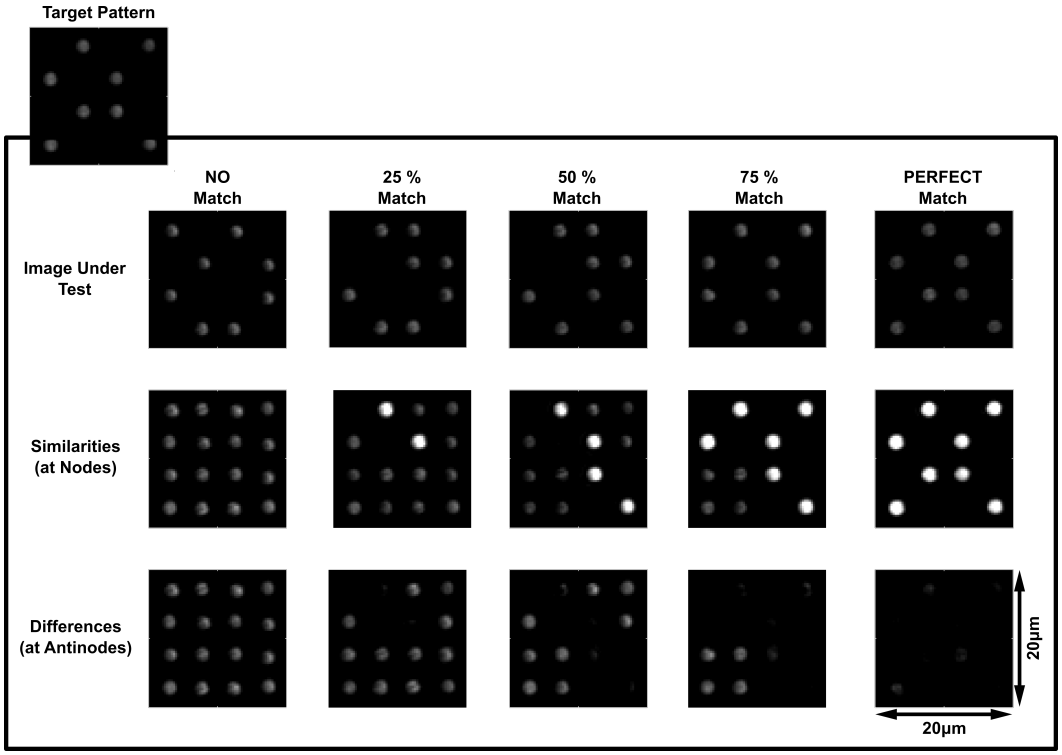


**Figure 4.4: Qualitative all-optical pattern recognition.** A target pattern is compared to a set of test patterns. Row 1 shows images of all patterns as captured by the CCD for single beam illumination. All test patterns are compared with the target pattern by projection onto opposite sides of the planar metamaterial using coherent light, revealing similarities (row 2) and differences (row 3) for phase differences between transmitted reference light and reflected test light for $\theta = 0$ and $\pi$, respectively.

The necessary power measurements are (i) the output power when the metamaterial is illuminated by the reference image only $P_{\mathrm{A,sgl}}$, as well as (ii) the maximum $P_{\max}$ and (iii) minimum $P_{\min}$ output power for simultaneous metasurface illumination by reference and test images. The latter are normalized by $4P_{\mathrm{A,sgl}}$ which yields $\tilde{P}_{\max}$ and $\tilde{P}_{\min}$ as described above, see Fig. 4.5. Theory predicts that the phase-dependent power fluctuation $\Delta\tilde{P} = \tilde{P}_{\max} - \tilde{P}_{\min}$ should correspond to the fraction of the reference pattern that overlaps with the test pattern, and indeed it is found that $\Delta\tilde{P}$ increases with pattern agreement. The measured $\Delta\tilde{P} = 0$ for 0% pattern agreement increasing to $\Delta\tilde{P} = 0.8$ for 100% pattern agreement, which is slightly less than the theoretical value of 1.0 due to experimental imperfections including about 1% residual transmission through nominally opaque mask areas, pattern misalignment, noise and background signals.

$4\tilde{P}_{\min}$ should correspond to the area where the reference and test patterns do not overlap and for 0% pattern agreement experiments correctly predict that the area of disagreement is twice as large as the illuminated area of the reference pattern. $\tilde{P}_{\min}$

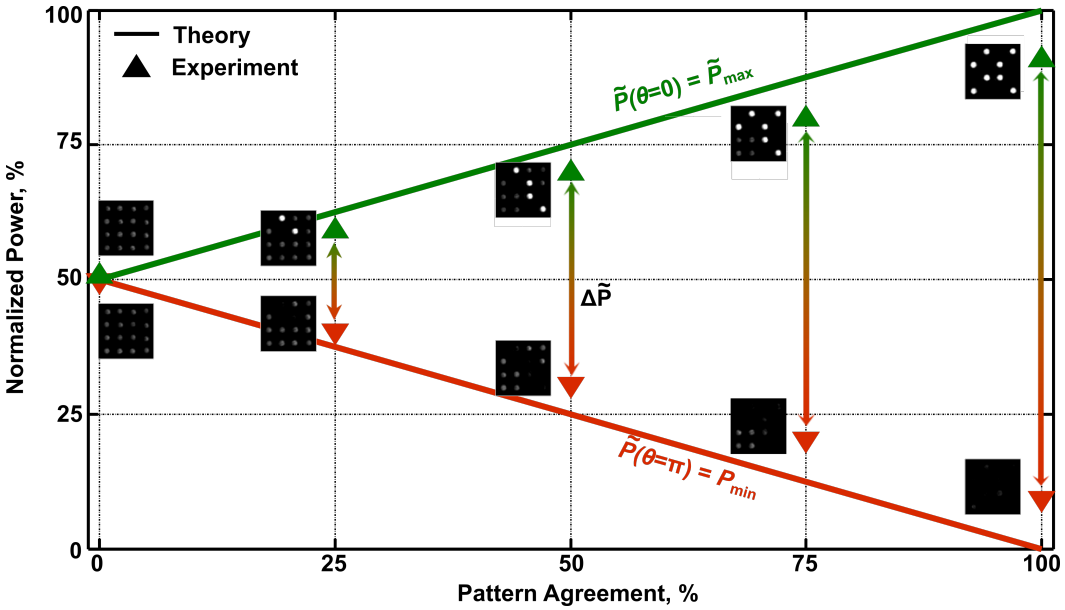


**Figure 4.5: Quantitative all-optical pattern recognition.** Maxima and minima of the measured (triangles) and expected (lines) total detected power normalized by 4× the total target pattern image power, $\tilde{P}$. The agreement between test and target patterns corresponds to the normalized power fluctuation, $\Delta\tilde{P}$ (double arrows). Graph insets depict the qualitative pattern recognition result of Fig. 4.4 for each case.

decreases monotonously with increasing pattern overlap reaching 0.1 — slightly more than the theoretical value of zero — for complete pattern agreement. Thus, the power measurements are consistent with theory and provide quantitative measurements of the level of image agreement and disagreement with about 80% of the theoretically predicted contrast (double arrows in Fig. 4.5). The experimental imperfections may be most easily taken into account by introducing an instrumental contrast correction factor $f$, e.g. $\tilde{P}_{\mathrm{corr}} = f(\tilde{P}_{\mathrm{exp}} - 0.5) + 0.5$. The ideal case corresponds to $f = 1.0$ and the contrast correction factor for this setup takes a value of about 1.2 here and about 1.1 with higher contrast masks in the case discussed in the following section for which the chromium thickness was increased from 120 nm to 130 nm to improve opacity of chromium-covered mask areas.

## 4.5 Image analysis

In order to illustrate the image analysis capabilities of the method, ice coverage evolution in the Arctic and Greenland region is experimentally analyzed. Binary designs based on satellite images available from the National Snow and Ice Data Center (USA) [186] were

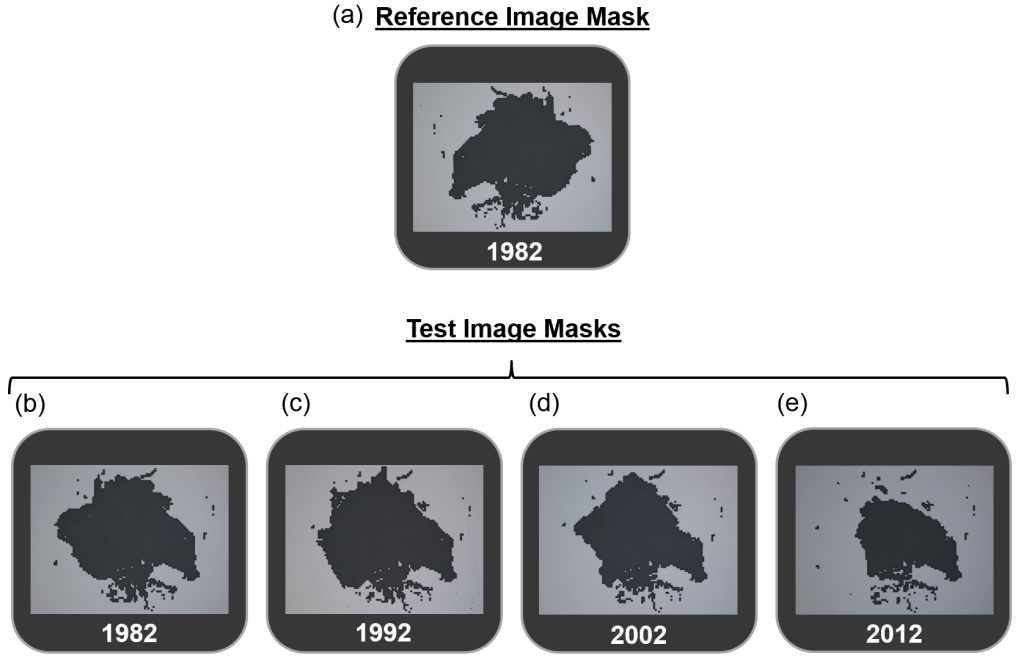


**Figure 4.6: Photolithography-fabricated binary Arctic and Greenland ice extent evolution masks for the period of 1982 to 2012.** Optical microscope images of binary masks representing September ice coverage based on satellite images taken 10 years apart [186]. (**a**) 1982 reference ice extent mask (for beam A) and (**b**)-(**e**) 1982 - 2012 ice extent masks for beam B. Gray areas represent chromium-covered (130 nm thick) opaque mask areas and darker areas correspond to glass. Test images are horizontally inverted on the masks with respect to the reference image in order to be projected on the metasurface with the correct orientation. Each satellite image was converted to a binary pattern of 100 $\times$ 100 square pixels of 22 $\mu$m $\times$ 22 $\mu$m each on the mask plane. Circular alignment marks were created on each mask during photolithography for alignment purposes (not shown).

created and fabricated on chromium-on-glass masks with photolithography, see Fig. 4.6. As previously stated, the images under test are horizontally inverted in order to match the orientation of the target image when projected on the metasurface. The images were taken one decade apart around the annual ice cover minimum which occurs in September from 1982 until 2012. Experiments are performed in the same experimental configuration that was used for pattern recognition (see Section 4.4) where all satellite images (test images B) are compared to the initial ice cover of 1982 (reference image A), see Fig. 4.7 a. Coherent interaction of the test and reference satellite images (row 1) on the metasurface clearly shows the regions where the ice cover remained unchanged (row 2) and the regions where the ice cover changed (row 3, mostly due to melting) for different phases of the illuminating beams. Using the CCD camera as an effective

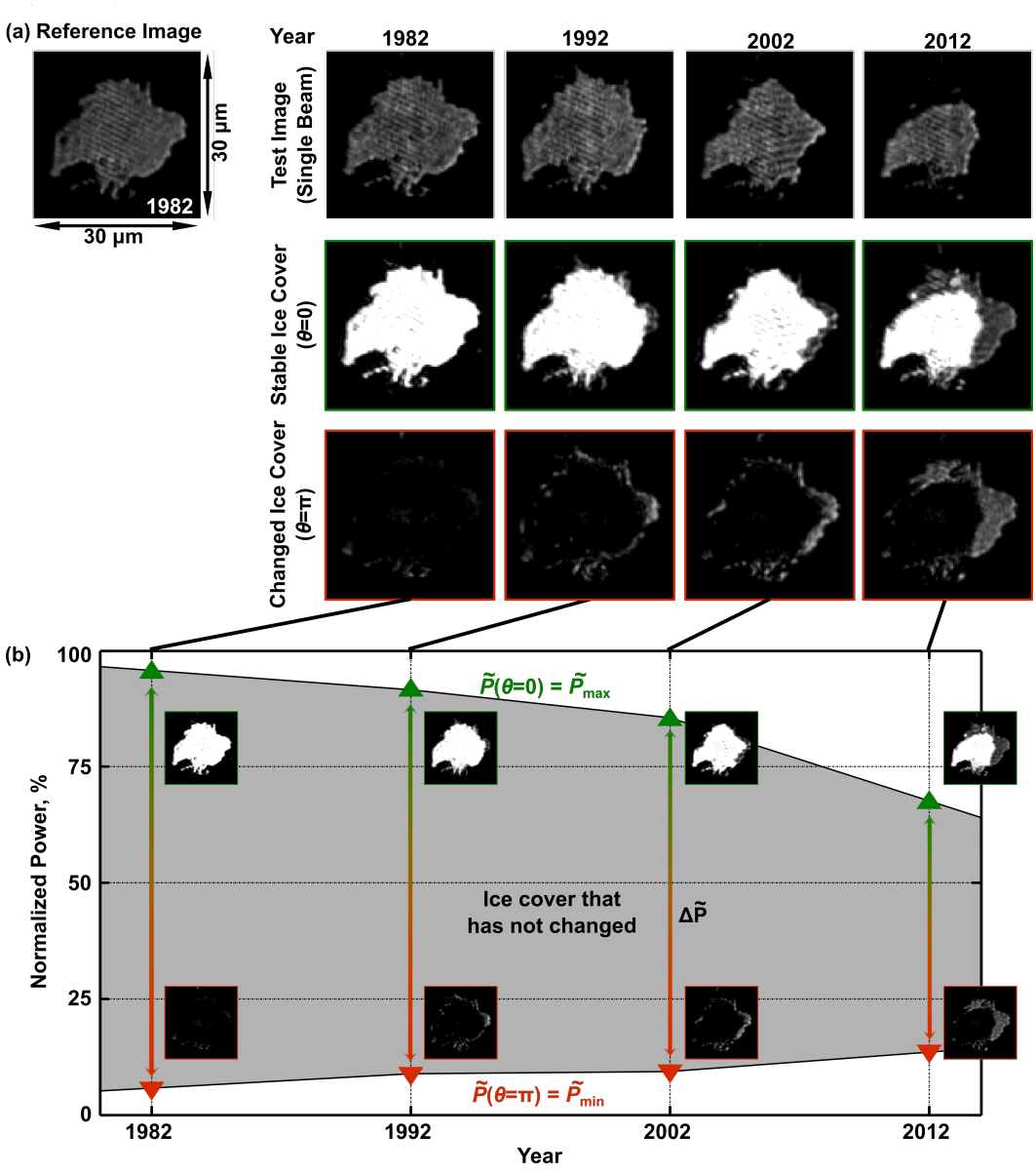


**Figure 4.7: Image analysis of Arctic and Greenland ice extent evolution from 1982 to 2012.** (**a**) Binary masks representing September ice coverage based on satellite images taken 10 years apart [186] as seen by the CCD camera for single beam illumination (row 1). Comparison to the initial 1982 ice cover by projection of the test and reference masks onto opposite sides of the metasurface using coherent light, revealing similarities (row 2) and differences (row 3) for phase differences between transmitted reference light and reflected test light of $\theta = 0$ and $\pi$, respectively. (**b**) Measured normalized power $\tilde{P}_{\max}$ (green, $\theta = 0$) and $\tilde{P}_{\min}$ (red, $\theta = \pi$), where $\Delta\tilde{P} = \tilde{P}_{\max} - \tilde{P}_{\min}$ (arrows) corresponds to the fraction of ice cover that remained unchanged and $4\tilde{P}_{\min}$ corresponds to the fraction of ice cover change (growth or melting). The power has been determined by integrating the intensity across the corresponding image.

photodetector, image power is integrated to determine the maximum and minimum of the phase-dependent normalized total power, $\tilde{P}_{\max}$ and $\tilde{P}_{\min}$, as described above, see Fig. 4.7 b. The phase-dependent power fluctuation $\Delta\tilde{P}$ corresponds to the area of ice cover that remained unchanged, indicating that the ice cover of 1982 remained largely intact until 1992 and that substantial melting took place thereafter. However, the power fluctuation alone does not indicate growth of ice in areas that were not covered in 1982. A much more detailed analysis becomes possible when taking both $\tilde{P}_{\max}$ and $\tilde{P}_{\min}$ into account to calculate the areas where the ice cover remained, melted and grew based on Table 4.1. Relative to the initial ice cover of 1982 ($S_{\mathrm{A}}$), the total ice cover of a test image $S_{\mathrm{B}}$ is given by $4\tilde{P}_{\mathrm{avg}} - 1$ and consists of the ice cover that remained unchanged $S_{\mathrm{A}\cap\mathrm{B}}$ given by $\Delta\tilde{P}$ and the ice cover $S_{\mathrm{B}\setminus\mathrm{A}}$ that grew since 1982 given by $4\tilde{P}_{\mathrm{avg}} - 1 - \Delta\tilde{P}$. The ice cover $S_{\mathrm{A}\setminus\mathrm{B}}$ that melted since 1982 is given by $1 - \Delta\tilde{P}$. Fig. 4.8 shows the correct theory values for remaining, grown and melted ice cover in comparison to the optical experiments. Experiments correctly reproduce the general ice cover evolution indicating that the total ice cover remains roughly constant until 1992 and then reduces by about 20% per decade. However, without applying an instrumental contrast correction factor, the areas of ice growth and ice melting are somewhat overestimated. If a contrast correction factor of $f = 1.1$ is applied to compensate for an experimental contrast of 90% rather than 100%, then the experiments reproduce the areas of ice cover that remained, melted and grew accurately.

## 4.6 Study on the spatial resolution of the experimental optical imaging interferometer

All experimental demonstrations throughout this thesis are underpinned by coherent control of metasurface absorption. The speed and power limitations of the principle have been recently explored [107–109] revealing its potential to reach THz bandwidths and quantum regime intensities. The exploitation of the principle for all-optical two-dimensional profile manipulation has been theoretically and experimentally demonstrated for the first time in Chapters 2 - 4. The application of the technique for pattern recognition and analysis of images (Sections 4.4 and 4.5) invokes the need to investigate the spatial resolution limitations of the experimental platform, i.e. to determine the smallest feature size that can be addressed experimentally under the two-dimensional

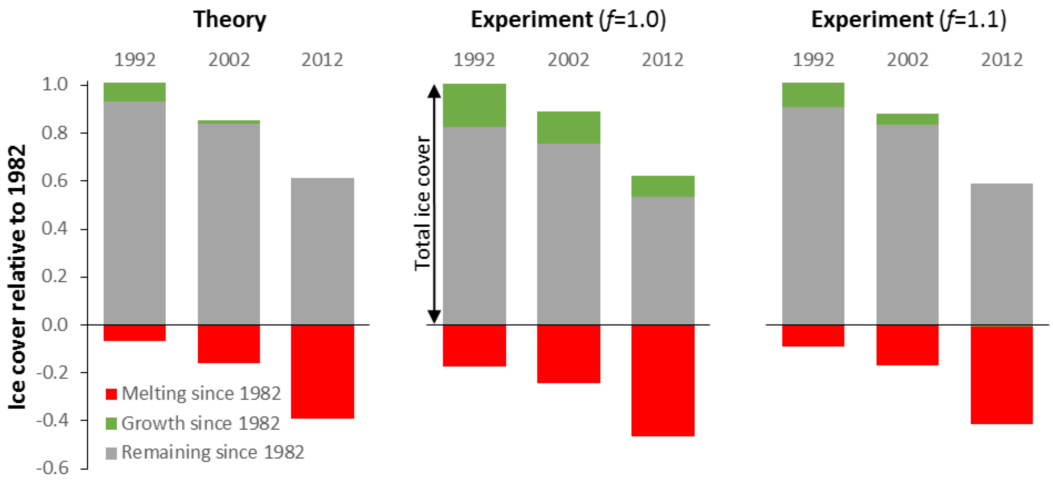


**Figure 4.8: Comparison of theoretical and experimental image analysis of Arctic and Greenland ice extent evolution from 1982 to 2012.** Exact theoretical and experimentally determined areas of molten $1-\Delta\tilde{P}$, grown $4\tilde{P}_{\text{avg}}-1-\Delta\tilde{P}$ and remaining $\Delta\tilde{P}$ ice cover relative to the original ice cover without ($f = 1.0$) and with ($f = 1.1$) contrast correction.

coherent control scheme.

In an experimental configuration that includes conventional imaging optics, the minimum-size feature that can be resolved is governed by the theoretical diffraction limit of the system. This is established by the Rayleigh criterion which defines the minimum separation distance between two spatially resolved point sources [187]:

$$\Delta l = 0.61\frac{\lambda}{NA}, \tag{4.3}$$

where $\lambda$ is the wavelength of light and $NA$ is the numerical aperture of the lenses, i.e. the angle range within which the lenses can emit or accept light. For the employed experimental system (Fig. 2.17), the numerical aperture is limited to $NA = 0.8$ by the infinity-corrected objectives included in either interferometer arm which are used to project the two-dimensional profiles of beam A and B on the metasurface from either side. It should be noted that although tube lens focal lengths are varied between experimental demonstrations, both infinity-corrected objectives are permanent parts of the configuration and therefore define the numerical aperture for all experiments. Subsequently, depending on the laser in use, the theoretical diffraction-limited resolution for the constructed optical system is $\Delta l = 598.6$ nm for $\lambda = 785$ nm when the CW fibre-coupled diode laser is employed and $\Delta l = 602.4$ nm for $\lambda = 790$ nm when the CW

fibre Bragg grating laser is used.

Another theoretical limitation to the spatial resolution of a realistic system arises from the Nyquist sampling theorem [188] based on which the pixel size of the employed detector should be no more than half the size of the smallest feature to be resolved. In the experimental demonstrations presented so far, the Evolve 512 Photometrics camera was used to monitor the system output. The sensor of this camera is comprised of 16 $\mu$m $\times$ 16 $\mu$m pixels arranged in a 512 $\times$ 512 array. For this camera, the minimum resolvable feature based on the Nyquist sampling theorem is 32 $\mu$m $\times$ 32 $\mu$m on the sensor plane. The permanent system optics that image the metasurface plane on the camera sensor result in 50$\times$ magnification ratio between the two planes. Therefore, the minimum feature size to be resolved by the Photometrics camera is equivalent to a 640 nm $\times$ 640 nm feature on the metasurface. This size is slightly larger than the diffraction-limited resolution ($\Delta l$) defined above for either experimental wavelength. In order to eliminate this detector-related limitation, a CCD camera with 4.65 $\mu$m $\times$ 4.65 $\mu$m pixels is used for the spatial resolution experiments of this section. For this camera, the minimum resolvable feature on the metasurface plane is 186 nm $\times$ 186 nm in size according to the Nyquist theorem which is well below the diffraction-limited spot size for either experimental wavelength.

In the theory of coherent control of metasurface absorption, the metasurface sample is considered to be a uniform film of deep sub-wavelength thickness since all nanostructure dimensions are smaller than the wavelength of light. However, in the case of two-dimensional coherent control, any inter-meta-molecular coupling induced across metasurface areas by alternating bright and dark features of the impinging spatially structured profile could result in an additional limitation to the system's spatial resolution. This case was theoretically investigated in Section 2.2.2 by simulating a semi-infinite array with different orientations of the optimized metasurface design under spatially varying illumination with one and two coherent input beams. In all cases, the inter-meta-molecular coupling resulted in the excitation of up to two meta-molecules (the furthest of which was almost negligibly excited) beyond a pre-defined transition line separating illuminated and non-illuminated metasurface areas. In terms of spatial resolution, this could be translated cautiously to a minimum separation length between bright features of the structured illuminating profiles equal to the length of two unit cells. The unit cell pitch of the metasurface is 350 nm $\times$ 350 nm resulting in a minimum

bright feature separation of 700 nm across the structured illuminating beam profiles.

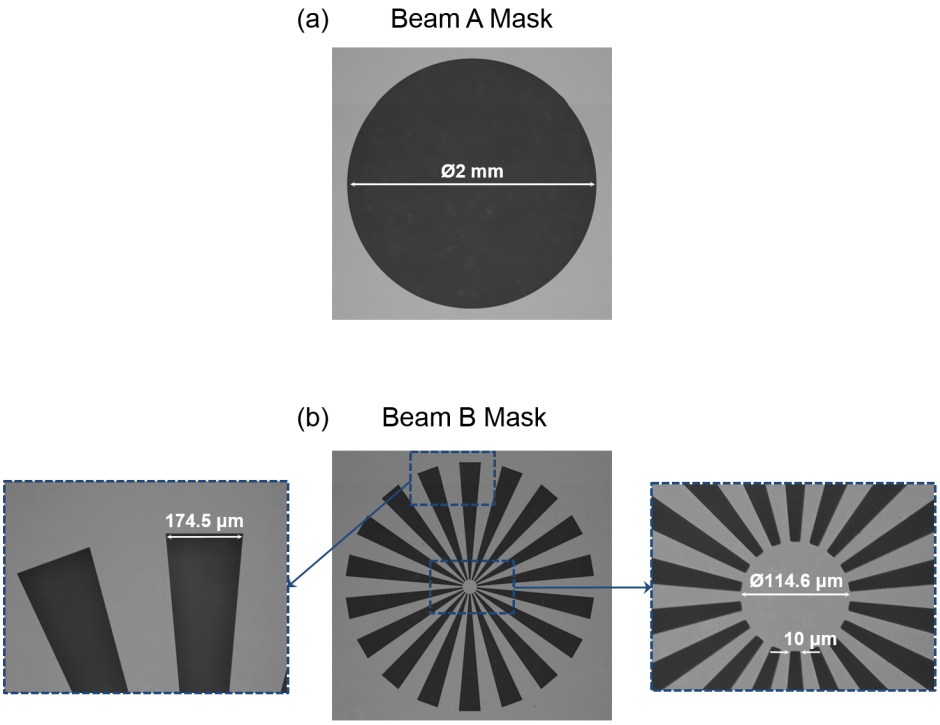


**Figure 4.9: Photolithography-fabricated masks for spatial resolution experiment.** Optical microscope images of the binary (**a**) beam A mask corresponding to a 2 mm diameter clear aperture and the (**b**) beam B mask carrying the sector star profile (central panel) of 2 mm outer diameter. Left and right panels provide zoomed views of the annotated areas of the central panel. Gray areas represent chromium-covered (130 nm thick) opaque mask areas and darker areas correspond to transparent glass.

In practice, experimental performance may be further compromised by aberrations introduced by any imperfections of the optics of the experimental setup and any deficiencies or non-uniformities of the fabricated metasurface. Therefore, it makes sense to experimentally investigate the achievable spatial resolution of the constructed optical platform. In the context of image processing as presented in Sections 4.2 - 4.5, this can be realized by employing an image mask including features that stretch the system's theoretically predicted spatial resolution limit. A broadly accepted spatial resolution test for optical systems is based on the projection and imaging of a sector star design by the tested system. Fig. 4.9 b shows a sector star design on a photolithography-fabricated chromium-on-glass mask. The design is formed by alternating bright and dark bars of identical dimensions that become thinner and more closely packed towards the centre

of the design. All bars have equal width at a particular radial distance from the centre of the design. Each bar has a width that is well above the theoretical limit of spatial resolution along the outer perimeter of the sector star and gradually reduces towards the center reaching sub-diffraction-limited widths near the inner perimeter of the design. As a result, the outer part of the sector star is clearly resolved by the system optics showing sharp bright and dark bars in the acquired image. Closer to the centre of the design, the contrast between bright and dark bars deteriorates significantly. At a particular radial distance $r$ from the centre of the design, bright and dark bars become indistinguishable. This radial distance provides a direct measure of the spatial resolution, as it is directly proportional to the width $w(r)$ of a pair of bright and dark bars at a given radial distance:

$$w(r) = 2rsin(\frac{2\pi}{N}), \tag{4.4}$$

where $N$ is the number of bars. For the minimum radius that is clearly resolved, $w(r)$ is the size of the minimum feature that can be clearly resolved by the optical configuration and therefore determines the system's spatial resolution limit. Consequently, a simple measurement of $r$ in a sector star image that is experimentally acquired is sufficient for the determination of spatial resolution.

Having defined the spatial resolution limitations according to theory, a sector star experiment is performed to test the existing platform. This experiment is conducted with the 790 nm fibre Bragg grating laser, a 400 mm tube lens with a 50× infinity-corrected objective (with $NA = 0.8$) in either interferometer arm resulting in 100× demagnification of beam A and B profiles when projected on the metasurface and a camera with 4.65 $\mu$m × 4.65 $\mu$m pixel pitch in the configuration of Fig. 2.17. For this combination, the theoretical minimum feature is limited to 604 nm by diffraction, to 186 nm by the Nyquist sampling theorem and to about 700 nm by inter-meta-molecular coupling in the nanostructure as predicted by simulations. Taking all the above into consideration, the minimum bar width in the centre of the sector star design should be smaller than 700 nm when projected on the metasurface. For the employed sector star $N = 36$ bars are included in the design, see Fig. 4.9 b. The inner and outer diameters of the sector star are equal to 114.6 $\mu$m and 2 mm, respectively. Therefore, the inner bar width is 10 $\mu$m and the outer bar width is 175.5 $\mu$m, which correspond to 100 nm and 1.755 $\mu$m, respectively, when projected on the metasurface. Separate experiments were conducted in order to acquire images of the sector star when projected

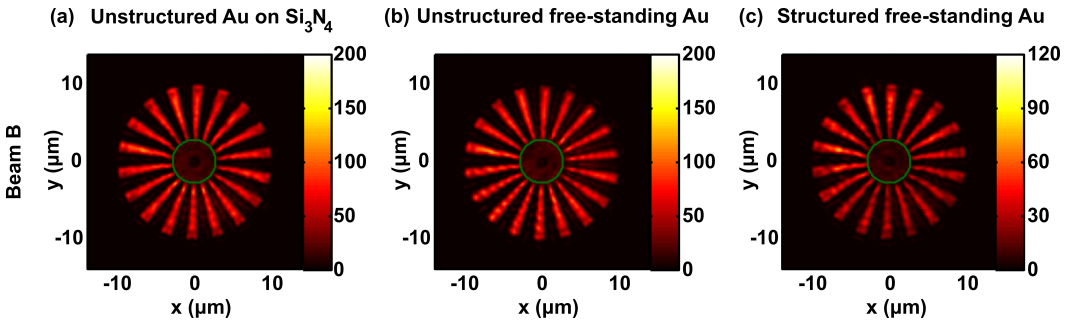


**Figure 4.10: Spatial resolution of the system for metasurface illumination by a single beam.** Images acquired in the absence of beam A when the sector star profile is projected on (**a**) unstructured gold of 60 nm thickness supported by $Si_3N_4$, (**b**) free-standing unstructured gold of 60 nm thickness and (**c**) free-standing structured gold of the metasurface. Green circles of radius $r$ annotate the circle outside which dark and bright bars are distinguishable in each case. Different colour scales are used in order to better depict any qualitative discrepancies between the images.

on the metasurface in the absence of beam A and in the presence of structured beam A transmitted through the clear aperture mask of Fig. 4.9 a.

In order to investigate any existing compromise of the system's spatial resolution arising from system aberrations, fabrication deficiencies and metasurface nanostructuring, the sector star mask was illuminated by beam B and projected on different sample areas which were imaged by the CCD camera in the absence of beam A, see Fig. 4.10. Initially, the imaging performance of the system was tested by projecting the sector star on an unstructured gold area that is supported by $Si_3N_4$ (panel a). This test eliminates any effects that may be introduced by any roughness or flatness imperfections caused by the removal of $Si_3N_4$ or the nanostructuring process. Following the method described above for the definition of the minimum resolved feature size $w(r)$, a green circle is plotted on top of the acquired sector star image in order to annotate the radial position $r$ outside which the bright and dark bars can be clearly distinguished. For the definition of this radial distance, horizontal and vertical intensity cross-sections of the acquired intensity image were plotted in Matlab. Simple observation of these cross-sections led to the definition of the radial distance beyond which the bright and dark features are indistinguishable, corresponding to almost flat lines in the intensity cross-sections. In Fig. 4.10 a, this measurement yields $r = 2.6\mu$m which is translated to $w(r) = 903$ nm. This spatial resolution deterioration (as compared to the theoretical prediction of 602.4 nm) is most likely related to unavoidable focusing and aberration

deficiencies introduced by the system's optics components and is also qualitatively noticeable in the intensity map of Fig. 4.10 a in the form of slightly curved bar edges. The quality of the image of the sector star seems to deteriorate slightly further when it is projected on free-standing unstructured gold, see Fig. 4.10 b, which is probably associated with surface flatness and roughness issues induced by the removal of $Si_3N_4$. Nevertheless, the measured spatial resolution remains unaffected and equal to $w(r) = 903$ nm. Fig. 4.10 c depicts the sector star image for projection on the metasurface area. Once again the measurement yields $w(r) = 903$ nm which reveals that nanostructuring does not induce any significant further compromise of the system's spatial resolution. This does not contradict the theoretical prediction that the metamaterial structure reduces the contrast between features spaced by less than 700 nm. Thus, the spatial resolution of the experimental setup is not limited by inter-meta-molecular coupling. It is limited by aberrations and free-standing gold roughness and flatness. The experimental results do not allow more specific conclusions on how inter-meta-molecular coupling affects the overall spatial resolution.

Lastly, the system's spatial resolution is tested for the case of coherent interaction of beams A and B on the metasurface. Beam A is passing through the clear aperture mask of Fig. 4.9 a, resulting in a uniformly illuminated disk of diameter equal to the outer diameter of the sector star (row 1 of Fig. 4.11). Beam B is carrying the sector star profile (row 2 Fig. 4.11) that is identical to the one used in Fig. 4.10. The limiting cases of coherent interaction between beams A and B when the metasurface coincides with a standing wave node or antinode are shown in rows 3 and 4 of Fig. 4.11, respectively. Fig. 4.11 b provides a zoomed view of Fig. 4.11 a, enabling clearer observation of any differences between rows 2, 3 and 4. Interestingly, in all three cases the sector star bars become distinguishable beyond $r = 2.6$ $\mu$m suggesting that the spatial resolution limit is still $w(r) = 903$ nm for the coherent case. Imperfect coherent transmission or absorption across parts of beam B cannot be directly associated to the system's spatial resolution as it could be resulting from intensity or phase mismatch across the wavefront or a local defect on the metasurface.

Conclusively, the system's spatial resolution is limited to $w(r) = 903$ nm on the metasurface plane, which is only 203 nm larger than what is theoretically predicted. Although this experiment was conducted to explore the experimental limitations of pattern recognition and image processing as presented in this Chapter, its conclusions

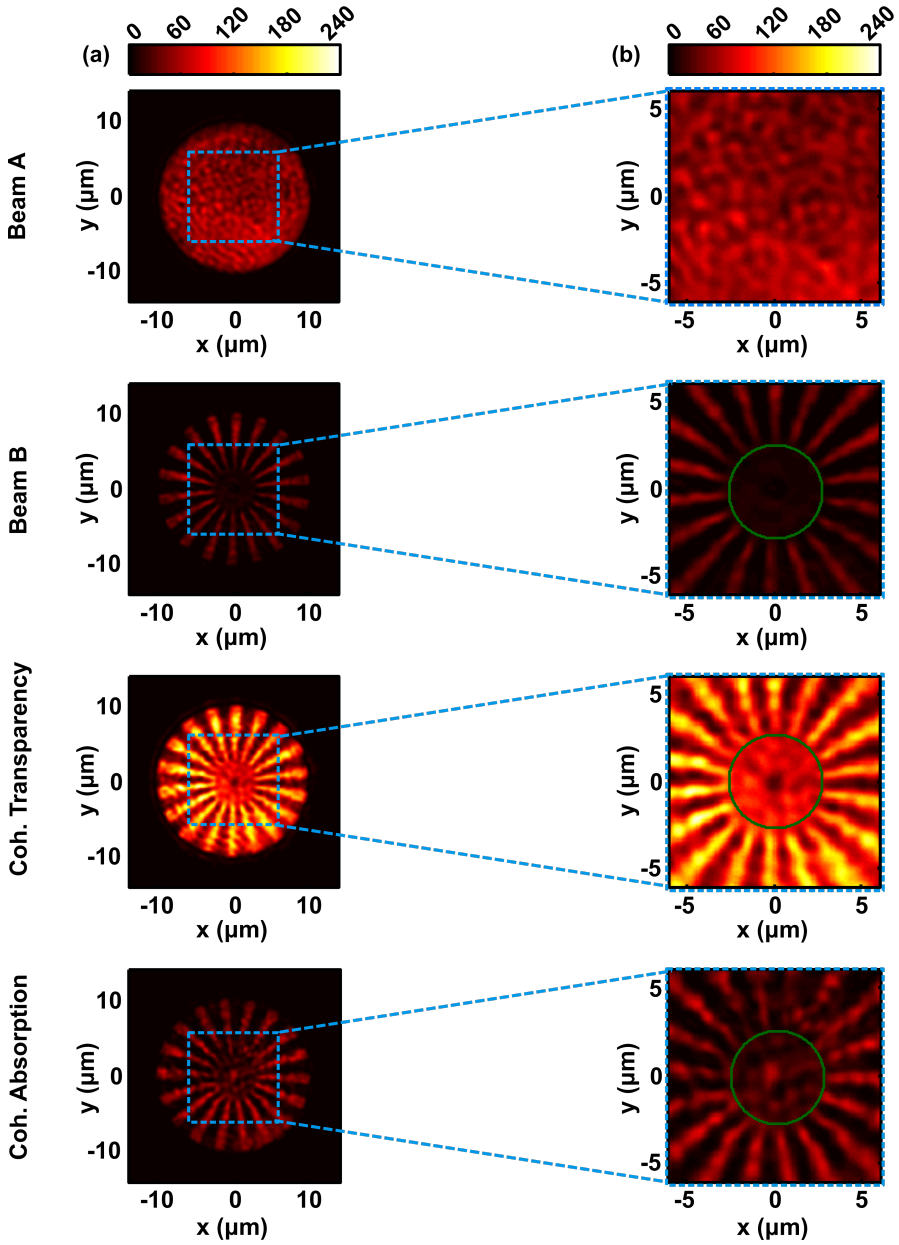


**Figure 4.11: Spatial resolution of the system for simultaneous metasurface illumination by two coherent beams.** (**a**) Illumination of the metasurface with beam A structured by a clear aperture mask (row 1) and beam B structured by the sector star mask (row 2) results in the coherent intensity enhancement of the bright bars of beam B at standing wave electric nodes (row 3) and their coherent absorption at standing wave anti-nodes (row 4). Column (**b**) provides zoomed views of the areas annotated with blue dashed lines in column **a**. Green circles of radius $r$ annotate the radius outside which dark and bright bars are distinguishable in each case. All images are plotted on the same colorscale.

apply to all experimental demonstrations that are conducted in the constructed optical imaging interferometer of Fig. 2.17. Even when using the larger pixel pitch sensor of the Evolve 512 camera, the spatial resolution limit of $w(r) = 903$ nm still applies since

it is larger than the two-pixel limitation imposed by the Nyquist theorem. Therefore, $w(r) = 903$ nm which is mainly originating from system aberrations, sample flatness and roughness imperfections, can be considered as a universal limitation to the spatial resolution of the measurements for all experimental demonstrations of this thesis.

## 4.7 Summary

In summary, all-optical image processing, binary pattern recognition and image analysis based on projecting pairs of images onto opposite sides of a planar metamaterial absorber using coherent light are presented. In contrast to nonlinear methods, the linear technique reported here does not have minimum intensity requirements and the underlying optical effect is known to operate on the femtosecond timescale. In terms of spatial resolution, image and pattern features down to 903 nm ($1.14\lambda$) in size can be resolved at the wavelength of 790 nm based on the presented sector star experimental test.

The presented pattern and image processing and recognition techniques enable both real-time mapping of similarities and differences between images using a CCD camera and quantitative analysis of the relationship between pairs of images with a photodetector. Binary images containing a large amount of optical data can be compared all-optically and their relationship can be quantified by 3 power values of electronic data that allow the area of image overlap, areas contained in one or the other image and any other set operation to be determined. Demonstrations include addressing of spatial features of the International Year of Light logo, binary pattern recognition for patterns of bright dots occupying 8 positions in a $4 \times 4$ grid and image analysis to determine the ice cover evolution in the Arctic and Greenland region based on satellite images. The introduced scheme is a hardware-based platform where image analysis and recognition is achieved with minor post-processing. Hence, this solution provides an alternative to computationally intensive pattern recognition and image analysis algorithms while circumventing the trade-off between speed and intensity requirements of previously established all-optical techniques that involve nonlinearities. Such a configuration could in principle be implemented in any imaging system that operates with coherent illumination and the speed and power requirements would be solely restricted by the response of the employed phase modulator and detector, since the underpinning coherent absorption effect could achieve bandwidths as high as 100 THz and operation in the quantum

regime.

# Chapter 5

# All-optical dynamic focusing of light with a plasmonic metasurface

*The work in this Chapter has been submitted for publication in [189] and is currently in press. Figs. 1-6 and Figs. S1-S6 of [189] are reproduced here.*

## 5.1 Introduction

Vision, microscopy, imaging, optical data projection and storage depend on focusing of light and the versatility of related technologies requires solutions that enable dynamic control over focusing properties. A light beam is focused by spatially varying its amplitude or phase distribution across the beam. Conventional convex lenses rely on the optical thickness of materials such as glass to introduce suitable phase delays, while Fresnel zone plates block light or introduce phase differences at certain radial distances from their centre in order to achieve constructive interference at the focus. Dynamic focusing is then realized by moving several solid lenses relative to each other [190], by elastic deformation [191], by varying curvature and optical thickness of microfluidic lenses [192, 192, 193] or via all-optical prescription of planar lens profiles on liquid crystal samples [194]. Moreover, spatial light modulators have been widely employed to vary the spatial intensity or phase profile of lenses [185, 195, 196]. Such techniques are based on

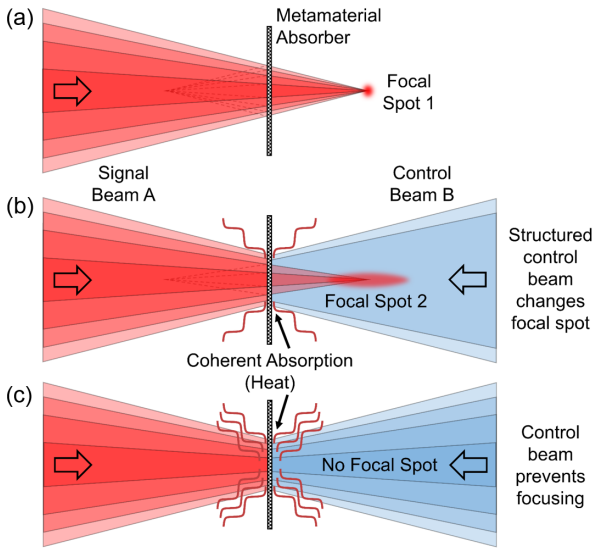


**Figure 5.1: Dynamic optical focusing with a metamaterial absorber** of substantially sub-wavelength thickness. A focused signal beam A produces focal spot 1 (**a**). A coherent structured control beam can modify signal beam A by controlling absorption on a metamaterial absorber, producing a modified focal spot 2 (**b**) or eliminating the focal spot altogether (**c**).

moving solid or liquid parts, or they rely on reorienting liquid crystal cells, making sub-millisecond response times difficult to achieve. While all-optical nonlinear self-focusing [197–199] can be much faster, its inherent intensity dependence and minimum intensity requirements are rarely practical.

As opposed to conventional dynamic focusing schemes, where control is accessed via mechanically reconfigurable lenses, spatial light modulators or microfluidics, in this Chapter dynamic control over optical focusing based on the linear interaction of light with light without moving parts is reported both theoretically and experimentally, see Fig. 5.1. The method for controlling optical focusing that is explored here exploits the properties of all-optical two-dimensional coherent control of light with light based on the theory introduced in Chapter 2. Spatially resolved coherent control of metasurface absorption allows continuous operation between the regimes of *coherent perfect transparency* and *coherent perfect absorption* by effectively translating the metasurface between nodes and anti-nodes of an optical standing wave, respectively. Hence, focusing of light resulting from illumination of the plasmonic metasurface with a Fresnel zone pattern (Fig. 5.1 a) can be controlled by another patterned beam projected on the same metasurface (Fig. 5.1 b and c) using coherent light.

In the demonstrations of this Chapter, two Fresnel zone plate patterns are imaged onto opposite sides of a lossy metasurface. Alteration of the control zone pattern enables dynamic control over intensity ("on" to "off"), depth (5 to 10 $\mu$m), diameter (700 to 940 nm) and focal distance (15 to 10.3 $\mu$m) of the focal spot as well as effective switching between a lens and a diffracting aperture. The focusing characteristics may be controlled continuously by modulating the phase of one illuminating beam. Switching can in theory be ultrafast (up to 100 THz) [108, 109]. In practice, switching occurs as fast as the control beam can be modulated, and electro-optical modulators can provide tens of gigahertz modulation bandwidth, which is orders of magnitude faster than mechanical and spatial light modulator technologies. Furthermore, the technique does not require any optically nonlinear materials and has been proven compatible with arbitrarily low intensities down to the single photon regime [107].

The presented scheme for all-optical dynamic focusing is essentially showing that coherent control of the interaction of light with a metasurface in a standing wave can effectively create a dynamically adjustable Fresnel zone plate. The following demonstrations prove that two-dimensional coherent control in metasurfaces can be useful in tasks requiring manipulation of light localization in three dimensions using the example of optical focusing.

## 5.2 Theoretical description of all-optical dynamic focusing based on two-dimensional coherent control of light with light

Two-dimensional coherent control of light with light in absorbing metasurfaces is employed to dynamically tune the focusing properties of binary Fresnel zone plates. The projection of Fresnel zone plates on either side of a metasurface by coherent counter-propagating beams results in the spatially resolved absorption of Fresnel zones from 0% to 100% based on the theory of two-dimensional coherent control. Following the mathematical description of Chapter 2, the interaction of two incident counter-propagating coherent light fields given by Eq. 2.7 with structured electric field amplitudes $E_A(x, y)$ and $E_B(x, y)$, on a thin film with complex scattering coefficient $s(\lambda)$ is described by Eqs. 2.9 - 2.11. The effective thin film translation along the established standing wave is imposed by varying the relative beam phase difference $\Delta\varphi = \arg(E_B) - \arg(E_A)$. Across

areas of spatial beam profile overlap, for an *ideal thin absorber* with scattering coefficient $s(\lambda) = -0.5$ (see Appendix A), illuminated by counter-propagating beams of equal amplitude, Eqs. 2.9 - 2.11 yield $E_C = E_A$ and $E_D = E_B$ for $\Delta\varphi = \pi$ (i.e. $E_C = -E_D$) and $E_C = E_D = 0$ for $\Delta\varphi = 0$ which correspond to the states of *coherent perfect transparency* and *coherent perfect absorption*, respectively. Therefore, for a particular Fresnel zone plate profile imposed on the profile of beam A, the profile of beam B can be patterned to address a desired number of zones in order to modify the focusing properties via selective absorption or enhanced transmission of lens zones from 0% up to 100%, see Fig. 5.1.

On this basis, for the exploration of suitable dynamic focusing paradigms several Fresnel zone plate designs were considered and their individual and combinatorial coherent response was investigated. The Fresnel zone plate structures were designed and optimized to meet the practical criteria of the experimental setup, i.e. Fresnel zones had to have a spatially resolved width and the resulting zone plates had to have focal distances, depths and diameters that can be efficiently scanned experimentally. In order to meet the practical criteria, the theoretical zone plate design was based on the generalized Fresnel zone plate radii definition:

$$R_n = \sqrt{(n+a)\lambda f + \frac{(n+a)^2\lambda^2}{4}}, \tag{5.1}$$

where $n$ is the zone order, $\lambda$ is the design wavelength, $f$ is the design focal length and $a$ is a reference phase that comes into play when an arbitrary length is added to all zone paths to the focal spot and facilitates complex design criteria combinations [200]. This radii definition ensures that all incoming light passing through the transparent Fresnel zone plate zones constructively interferes at a distance $f$ in front of the zone plate along its symmetry axis. It should be noted that for $a = 0$ the above formula yields $R_n = \sqrt{n\lambda f + \frac{n^2\lambda^2}{4}}$ which is the more widely known Fresnel zone plate radii definition. For each Fresnel zone plate, the scalar angular spectrum method [201, 202] is employed via a Matlab code in order to calculate the resulting light distribution when the zone plate placed in the $xy$-plane at $z = 0$ is illuminated by a plane wave propagating along $z$. Based on these calculations the full width at half maximum of the focal spot intensity in the $xy$-plane at $z = f$ as well as the full width at half maximum along the optical axis were calculated for each case in order to examine compliance with the scanning range capabilities of the available experimental components.

Taking all the above into consideration, the targeted focal length was set to $f = 15$ $\mu$m, for an instrumental reference phase of $a = -0.5$ at the design wavelength of $\lambda = 790$ nm. Table 5.1 provides the radii of the optimized design including 7 zones for beam profile A as depicted in Fig. 5.2 a. For beam profile B, individual cases of addressing the full zone plate structure to modulate focal intensity (Fig. 5.2 b), the inner most zones of the plate to vary focal depth and diameter (Fig. 5.2 c), as well as an inverted zone plate (Fig. 5.2 d) leading to switching between a lens and a transparent lens-sized aperture were chosen to illustrate the potential of two-dimensional coherent control for all-optical dynamic tuning of focusing. In the following sections theoretical and experimental results will be presented for each individual case.

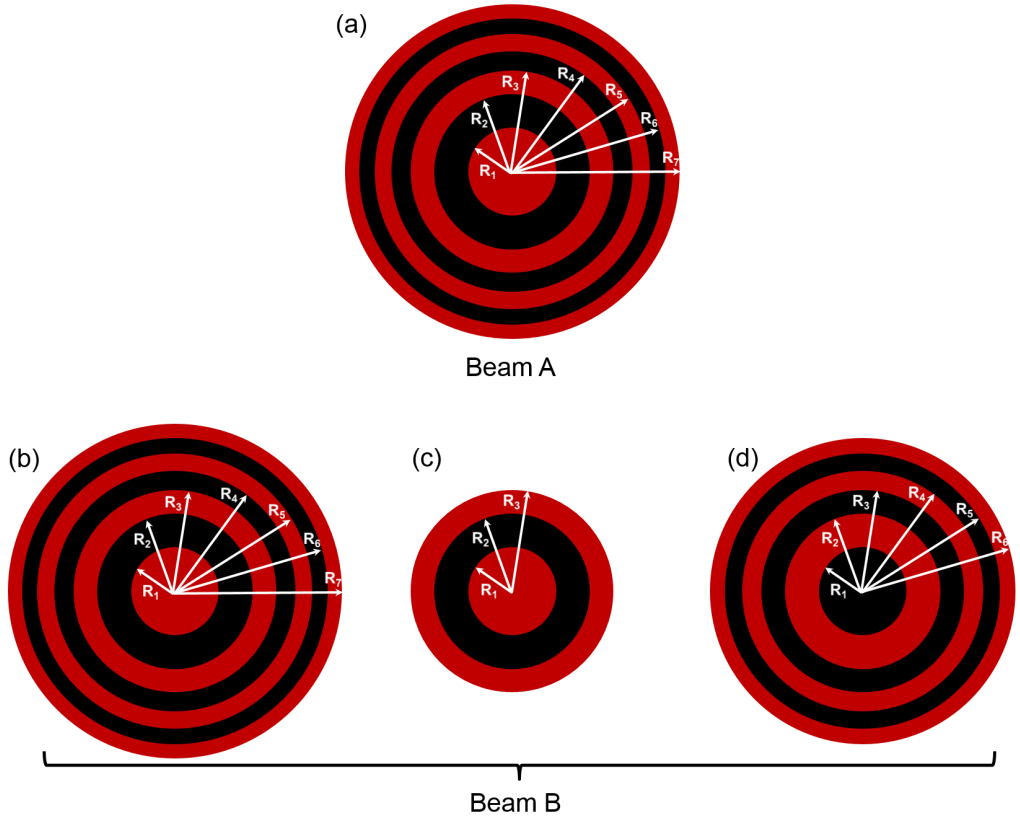


**Figure 5.2: Fresnel zone plate designs for dynamic control of optical focusing.** (**a**) Beam A Fresnel zone plate pattern design including 7 individual zones that can be coherently addressed by beam B Fresnel zone plates including (**b**) a pattern that is identical to beam A zones, (**c**) a pattern that corresponds to the three inner zones of beam A and (**d**) the inverted beam A zones. All zone plate designs target the creation of a focal spot at $f = 15$ $\mu$m for $a = -0.5$ and $\lambda = 790$ nm. Based on these parameters, zone radii $R_1$ - $R_7$ are calculated based on Eq. 5.1 and provided in Table 5.1. Design radii are common for all designs. Transmissive and opaque design zones are represented by red and black, respectively.

**Table 5.1:** Fresnel zone plate design radii based on Eq. 5.1 for $f = 15$ $\mu$m, $a = -0.5$ and $\lambda = 790$ nm.

Fresnel zone plate design radii in $\mu$m

| $R_1$ | $R_2$ | $R_3$ | $R_4$ | $R_5$ | $R_6$ | $R_7$ |
|---|---|---|---|---|---|---|
| 2.44 | 4.26 | 5.53 | 6.58 | 7.52 | 8.36 | 9.14 |

## 5.3 Demonstration of all-optical dynamic focusing functionalities

### 5.3.1 All-optical setup for coherent control of focusing properties

For the experimental demonstrations of all-optical dynamic control over focal intensity, depth and diameter the fabricated metasurface described in Fig. 2.14 is employed. For this case the experimental wavelength is 790 nm, where the metasurface absorbs about 34% of a single illuminating beam and has almost the same spectral response when illuminated from its front and rear sides. Fresnel zone plates are imaged on the metasurface from either side and their focusing properties are dynamically controlled. In order to capture the Fresnel zone plate properties, the resulting intensity distributions of the modified focal spots need to be imaged at various positions along the optical axis by the system's CCD camera. Therefore, the previously employed configuration of Fig. 2.17 needs to be modified accordingly, as illustrated in Fig. 5.3.

Throughout this work, incident light is linearly polarized with the electric field parallel to the symmetry axis of the metasurface. Coherent control of focusing of light with light is explored for Fresnel zone plate lenses manufactured by photolithography from a 130-nm-thick chromium layer on a glass substrate, see Fig. 5.3 i - iv. The Fresnel zone plate for beam A, see Fig. 5.3 i, is designed to create a focal spot at a focal distance of 15 $\mu$m in front of the metasurface. Following the design of the Fresnel zone plate for beam A, three Fresnel zone plates for beam B are fabricated corresponding to patterns comprised of zones that are identical to beam A zones (Fig. 5.3 ii), the three inner zones of beam A (Fig. 5.3 iii) and the inverse of beam A zones (Fig. 5.3 iv).

Pairs of zone plates are imaged onto opposite sides of the metasurface with 75× demagnification (via a combination of a 300 mm focal length tube lens with a 50× infinity-corrected objective of 4 mm focal length) using light from the same 790 nm

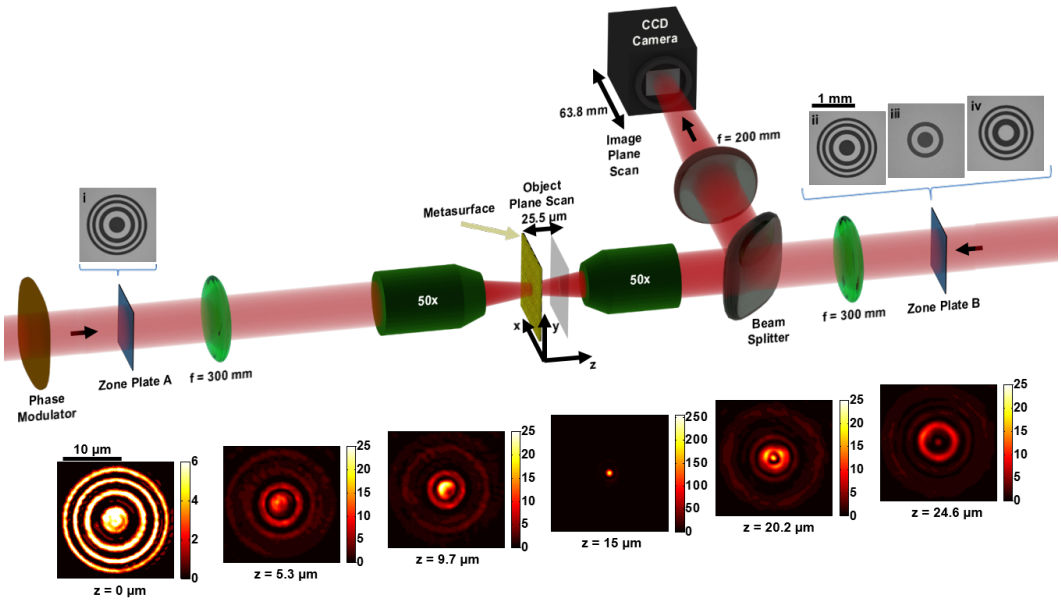


**Figure 5.3: Coherent control of optical focusing** is achieved by imaging Fresnel zone plates A and B onto opposite sides of a metasurface using coherent light of 790 nm wavelength. The optical microscope images of the fabricated chromium-on-glass zone plate masks are depicted in insets i - iv. At the metasurface, the images of the Fresnel zone plates A and B are demagnified 75× by a combination of a 300 mm focal length lens and an infinity-corrected 1 mm working distance 50× objective. Using the same objective combined with a 200 mm focal length lens, the intensity distribution at different distances $z$ from the metasurface is imaged onto a CCD camera by translating the camera along the optical path. The image sequence at the bottom shows intensity patterns recorded by the camera at different distances $z$ when identical zone plates A and B are imaged on the lossy metasurface positioned near a node of the standing wave ($\Delta\varphi = \pi$) as in the third row of Fig. 5.5. Here the intensity map taken at $z = 15$ $\mu$m depicts the focal hotspot created by the Fresnel zone plates.

wavelength fiber-Bragg-grating-stabilized CW diode laser with 2 mW output power and less than 0.01 nm line width. Dynamic control over focusing is achieved by modulating the phase of light illuminating one zone plate with a liquid crystal phase modulator. Focusing of light resulting from transmission of zone plate image A and reflection of zone plate image B is characterized by imaging in front of the metasurface (object plane) starting at $z = 0$ (metasurface plane) up to $z = 25.5$ $\mu$m in steps of 880 nm with a CCD camera (Thorlabs DCU224M). Using an optical imaging system with 50× magnification $M$ to image the metasurface plane on the camera (combination of a 200 mm focal length tube lens with a 50× infinity-corrected objective of 4 mm focal length), the longitudinal magnification is defined by $M^2$ [203] and therefore scanning is achieved by moving the

camera 63.8 mm along the wave propagation direction in 2.2 mm steps using a linear z-axis translation stage. This scanning range is well beyond the focal length, which was designed to be 15 $\mu$m in all cases.

The input beam intensities are chosen such that transmission of beam A and reflection of beam B have the same intensity when the zone plates are not present. The different experimental data sets studying (i) identical Fresnel zone plates, (ii) zone plates with a different number of rings and (iii) inverted zone plates use different camera exposure times to make optimal use of the camera's dynamic range. Therefore, intensity is shown in the same arbitrary units within each data set, but different data sets use different arbitrary units in the following demonstrations.

Alongside experimentally acquired data sets, theoretical light distributions calculated based on the angular spectrum method [201, 202] are provided for all cases to validate experimental performance based on expected coherent and incoherent responses. To aid comparison between experimental and theoretical intensity distributions, the arbitrary intensity units of the theoretical data sets are chosen such that the theoretical focal peak intensity of Fresnel zone plate A matches that of the corresponding experimental data set.

In all cases, the focal diameter is determined as the full width half maximum of the focal spot intensity in the $xy$-plane at $z = 15$ $\mu$m and the focal depth was determined as the full width half maximum of the focal spot intensity along the optical axis ($z$-axis).

### 5.3.2 Control of focal intensity

Considering the simplest case of imaging identical Fresnel zone plates on opposite sides of the *ideal thin absorber* or metasurface and following the analysis of Section 5.2, $\Delta\varphi = \pi$ yields $E_C = -E_D$ implying identical focusing behaviour of maximum intensity in both directions, whereas $\Delta\varphi = 0$ results in absorption of all light, $E_C = E_D = 0$.

Fig. 5.4 illustrates the theoretically predicted coherent control of focal intensity with light, which results from imaging of identical Fresnel zone plates A and B onto opposite sides of an *ideal thin absorber* with coherent light. Fig. 5.5 corresponds to the experimentally measured coherent control of focal intensity. Fig. 5.6 includes the focal spot depth and diameter graphs for both theoretical (Fig. 5.4) and experimental results (Fig. 5.5). The projections of the individual zone plates onto the metasurface and the

resulting focusing characteristics are shown by the first two rows in Figs. 5.4 - 5.6. Both zone plates form similar focal spots with about 15 $\mu$m focal length, 4.4 $\mu$m focal depth and 800 nm focal diameter which are in excellent agreement between theoretical and experimental data sets for all cases, see Fig. 5.6.

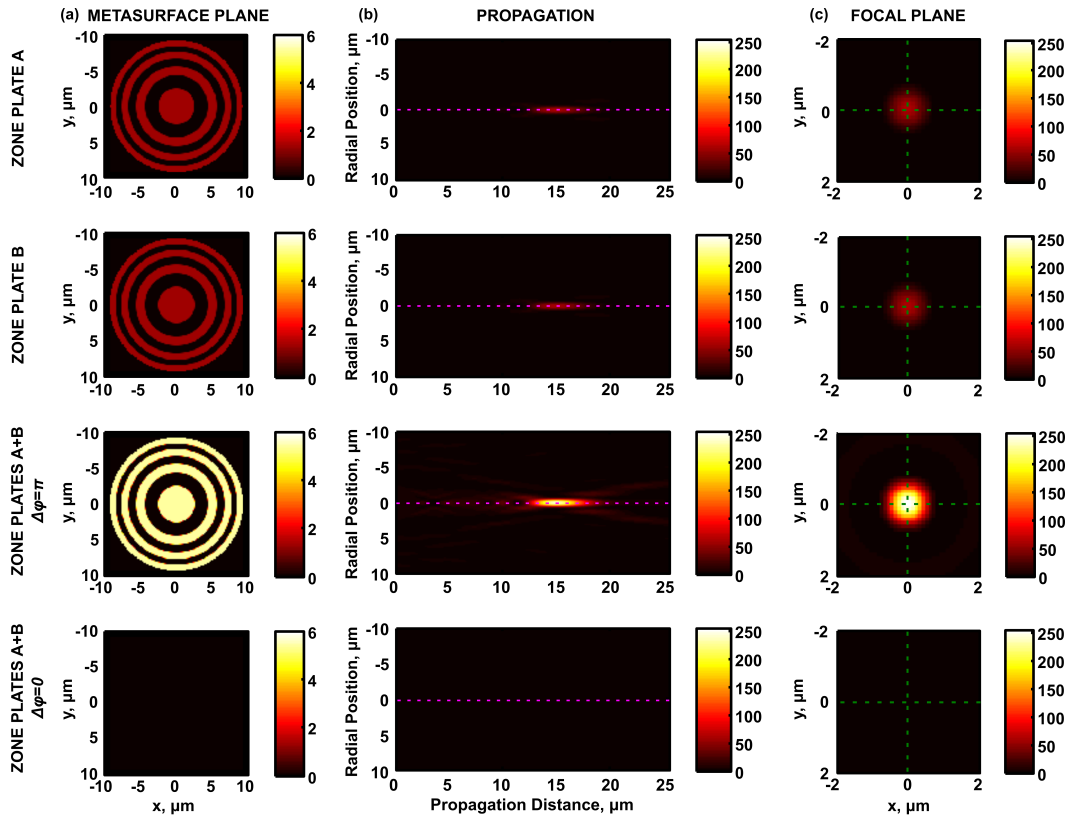


**Figure 5.4: Simulation results for controlling focal intensity** by projecting identical Fresnel zone plate patterns, A (row 1) and B (row 2) onto opposite sides of the metasurface. Coherent interaction of patterns A and B on the metasurface leads to high focal intensity for $\Delta\varphi = \pi$ (row 3), while $\Delta\varphi = 0$ (row 4) leads to vanishing focal intensity. (**a**) Simulated intensity on the metamaterial plane. (**b**) Simulated light distribution at different distances $z$ from the metasurface ($yz$-plane). The pink dotted line indicates the optical axis along which the focal depth is defined. (**c**) Simulated intensity distribution in the focal plane at $z = 15$ $\mu$m. Green dotted lines indicate the intensity cross-sections used to determine the focal diameter. All color scales show intensity.

Simultaneous projection of both lens patterns onto the metasurface does not affect the focal depth and diameter within experimental accuracy, however, the focal intensity becomes strongly dependent on the phase difference of the illuminating beams, see Figs. 5.4 - 5.6. Coherent interaction of lens pattern A with lens pattern B for $\Delta\varphi = \pi$ (row 3) leads to a 4-fold intensity increase, while $\Delta\varphi = 0$ (row 4) results in almost complete absence of the focal spot. While simulations predict that the focal intensity

should reduce to zero for $\Delta\varphi = 0$, a residual intensity of about 7% of the peak intensity is observed in experiments, corresponding to 1400% contrast between maximum and minimum focal intensity. The residual intensity arises from experimental imperfections related to the accuracy of phase control and alignment as well as metasurface flatness and homogeneity. The focal intensity can be controlled continuously between these extremes by varying $\Delta\varphi$ from 0 to $\pi$.

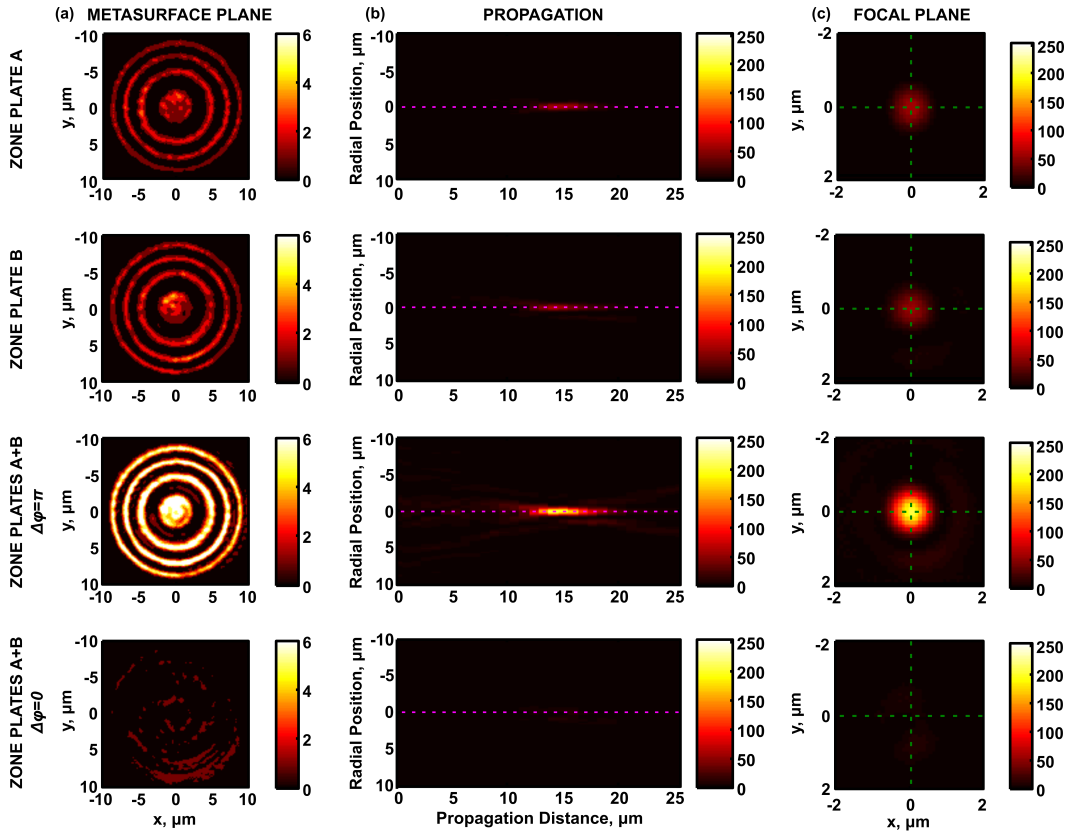


**Figure 5.5: Experimental results for controlling focal intensity** by projecting identical Fresnel zone plate patterns, A (row 1) and B (row 2) onto opposite sides of the metasurface. Coherent interaction of patterns A and B on the metasurface leads to high focal intensity for $\Delta\varphi = \pi$ (row 3), while $\Delta\varphi = 0$ (row 4) leads to vanishing focal intensity. Column (**a**): Images of the metamaterial plane taken with a camera. Column (**b**): Measured light distribution at different distances $z$ from the metasurface ($yz$-plane). The pink dotted line indicates the optical axis along which the focal depth is defined. Column (**c**): Measured intensity distribution in the focal plane at $z = 15$ $\mu$m. Green dotted lines indicate the intensity cross-sections used to determine the focal diameter.

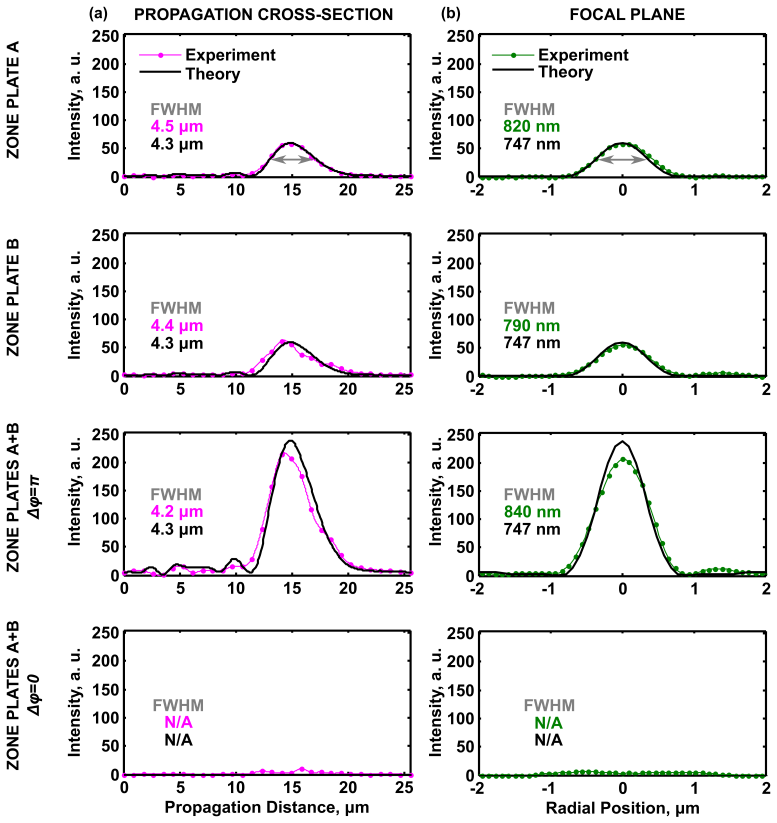


**Figure 5.6: Focal depth and diameter for identical Fresnel zone plate patterns**, A (row 1) and B (row 2) projected onto opposite sides of the metasurface. Coherent interaction of patterns A and B on the metasurface leads to high focal intensity for $\Delta\varphi = \pi$ (row 3), while $\Delta\varphi = 0$ (row 4) leads to vanishing focal intensity. Column (**a**): Calculated (black solid lines) and measured (pink lines with data points) intensity distribution along the optical axis (indicated by pink dotted lines in Figs. 5.4 and 5.5). Column (**b**): Calculated (black solid lines) and measured (green lines with data points) radial intensity distribution in the focal plane at $z = 15$ $\mu$m, obtained by averaging cross-sections along $x$ and $y$ (indicated by green dotted lines in Figs. 5.4 and 5.5).

### 5.3.3 Control of focal depth and diameter

Figs. 5.7 - 5.9 illustrate coherent control of focal depth and diameter with light, which results from imaging Fresnel zone plates with a different number of rings onto opposite sides of the metasurface, where the smaller zone plate corresponds to the central part of the larger one. The projections of the individual zone plates onto the metasurface and the resulting focusing characteristics are shown by the first two rows in all three figures and the arbitrary intensity units of the theoretical data set has been chosen such that the theoretical focal peak intensity of Fresnel zone plate A matches that of the corresponding experimental data set. The smaller 2-ring zone plate has an increased

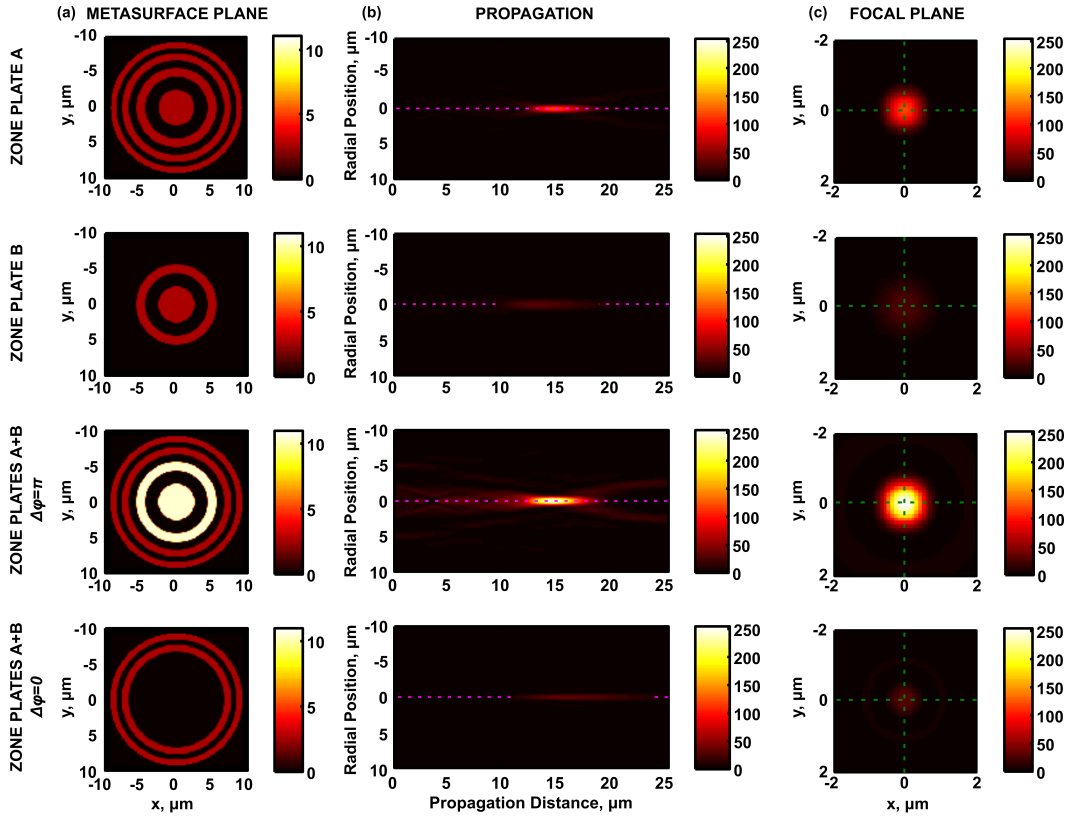


**Figure 5.7: Simulation results for controlling focal depth and diameter** by projecting different Fresnel zone plate patterns, A (row 1) and B (row 2) onto opposite sides of the metasurface. Coherent interaction of patterns A and B on the metasurface leads to a short, high-intensity focus for $\Delta\varphi = \pi$ (row 3), while $\Delta\varphi = 0$ (row 4) a dimmer, narrower Bessel-beam-like focus with a large focal depth. (**a**) Simulated intensity on the metamaterial plane. (**b**) Simulated light distribution at different distances $z$ from the metasurface ($yz$-plane). The pink dotted line indicates the optical axis along which the focal depth is defined. (**c**) Simulated intensity distribution in the focal plane at $z = 15$ $\mu$m. Green dotted lines indicate the intensity cross-sections used to determine the focal diameter. All color scales show intensity.

focal depth and diameter compared to the 4-ring zone plate, see Fig. 5.9. Simultaneous projection of both lens patterns onto the metasurface creates an effective zone plate, where the phase $\Delta\varphi$ controls the contribution of the inner rings from 4-fold intensity enhancement ($\Delta\varphi = \pi$, row 3 of Fig. 5.7 a and Fig. 5.8 a) to complete suppression ($\Delta\varphi = 0$, row 4 of Fig. 5.7 b and Fig. 5.8 b) compared to the outer rings.

Enhancement of the inner rings yields similar focusing characteristics to the original 4-ring zone plate (see row 3 of Fig. 5.9) with a small increase in focal depth and diameter, accompanied by about 2-fold focal spot intensity increase. In contrast, suppression of the inner rings yields a dimmer focus resembling an optical needle [204] or a Bessel beam

[205, 206], which has a very long focal depth of 10 $\mu$m and a small, sub-wavelength focal diameter of only 700 nm (Fig. 5.9). Thus, variation of $\Delta\varphi$ from $\pi$ to 0 allows the focal depth to be controlled from 5-10 $\mu$m and the focal diameter that determines the resolution to be controlled from 940-700 nm, corresponding to dynamic ranges of 100% and 35%, respectively.

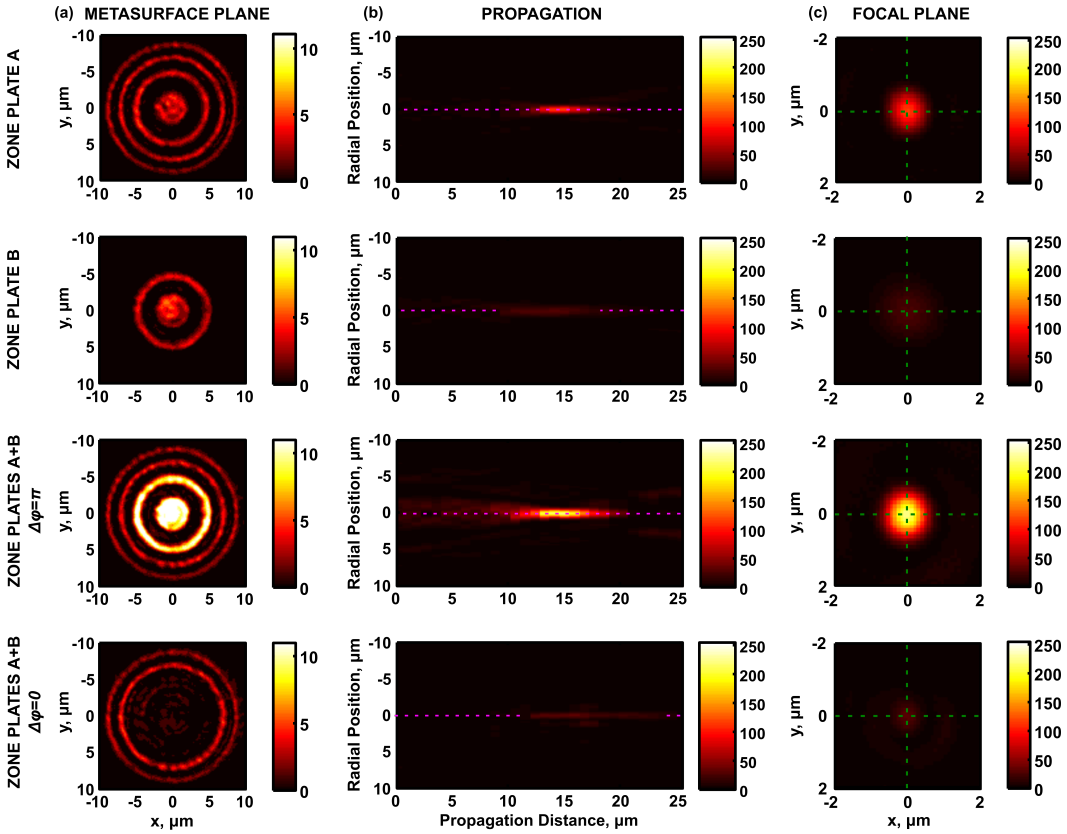


**Figure 5.8: Experimental results for controlling focal depth and diameter** by projecting different Fresnel zone plate patterns, A (row 1) and B (row 2) onto opposite sides of the metasurface. Coherent interaction of patterns A and B on the metasurface leads to a short, high-intensity focus for $\Delta\varphi = \pi$ (row 3), while $\Delta\varphi = 0$ (row 4) leads to a dimmer, narrower Bessel-beam-like focus with a large focal depth. Column (**a**): Images of the metamaterial plane taken with a camera. Column (**b**): Measured light distribution at different distances $z$ from the metasurface ($yz$-plane). The pink dotted line indicates the optical axis along which the focal depth is defined. Column (**c**): Measured intensity distribution in the focal plane at $z = 15$ $\mu$m. Green dotted lines indicate the intensity cross-sections used to determine the focal diameter. All color scales show intensity.

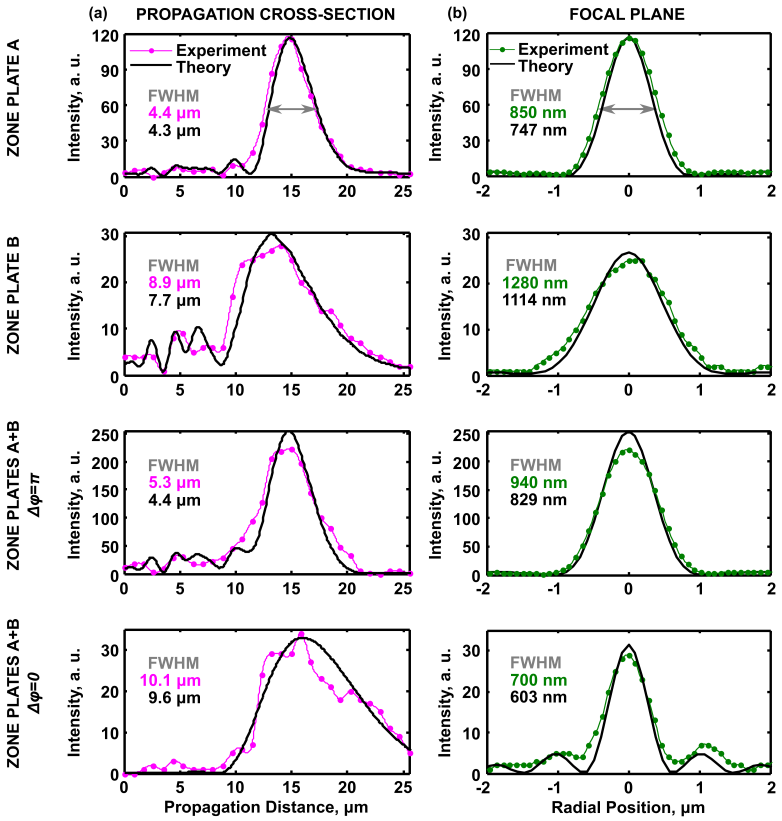


**Figure 5.9: Focal depth and diameter for different Fresnel zone plate patterns**, A (row 1) and B (row 2) projected onto opposite sides of the metasurface. Coherent interaction of patterns A and B on the metasurface leads to a short, high-intensity focus for $\Delta\varphi = \pi$ (row 3), while $\Delta\varphi = 0$ (row 4) leads to a dimmer, narrower Bessel-beam-like focus with a large focal depth. Column (**a**): Calculated (black solid lines) and measured (pink lines with data points) intensity distribution along the optical axis (indicated by pink dotted lines in Figs. 5.7 and 5.8). Column (**b**): Calculated (black solid lines) and measured (green lines with data points) radial intensity distribution in the focal plane at $z = 15$ $\mu$m, obtained by averaging cross-sections along $x$ and $y$ (indicated by green dotted lines in Figs. 5.7 and 5.8).

### 5.3.4 Theoretical description of continuous control over focal properties

In Sections 5.3.2 and 5.3.3, the all-optical dynamic control of focusing intensity, focal depth and diameter has been presented both theoretically and experimentally in the context of the states of *coherent perfect transparency* and *coherent perfect absorption* for relative beam phase differences of $\pi$ and 0, respectively. However, the presented scheme can provide continuous control of the targeted focusing properties through continuous phase alteration. Fig. 5.10 shows the modelled phase-dependence of focal intensity, depth and diameter for identical zone plates (as in Figs. 5.4 - 5.6) and for zone plates

with a different number of rings (as in Figs. 5.7 - 5.9), illustrating that phase modulation can indeed provide continuous control over focusing characteristics between the experimentally observed extremes. A normalized intensity scale was used in Fig. 5.10 as explained in the figure caption.

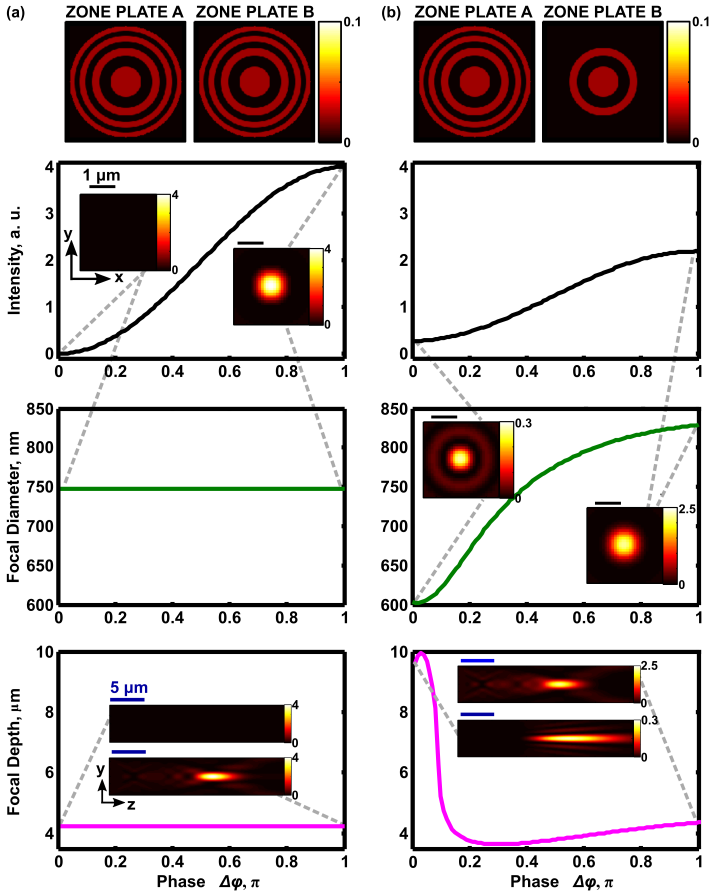


**Figure 5.10: Simulated phase-dependence of focal properties** for interaction of (**a**) identical Fresnel zone plate patterns (as in Figs. 5.4 - 5.6) and (**b**) Fresnel zone plate patterns of different size (as in Figs. 5.7 - 5.9) on an *ideal thin absorber*. The intensity is normalized by the focal intensity produced by lens pattern A alone. Row 1 shows the intensity distribution for each zone plate pattern alone, rows 2 and 3 show the peak intensity and FWHM focal diameter at the nominal focal distance of $z = 15$ $\mu$m, respectively. Row 4 shows the FWHM focal depth. All color scales show intensity.

### 5.3.5 Effective switching between a lens and a diffracting aperture

Following the demonstrations of all-optical control of focal intensity, depth and diameter, dynamic focusing may also be controlled by effectively removing the lens and replacing it with a lens-sized clear aperture without moving parts. This is achieved by projecting

inverted zone plate patterns onto the metasurface as illustrated by rows 1 and 2 in Figs. 5.11 - 5.13. Depending on the phase difference between the projected inverse zone plate patterns, their superposition on the metasurface forms an intensity distribution corresponding to that of a homogeneously illuminated circular disk for $\Delta\varphi = \pi$ (row 3 in Figs. 5.11 - 5.13) or rings of equal intensity but opposite phase for $\Delta\varphi = 0$ (row 4 in Figs. 5.11 - 5.13).

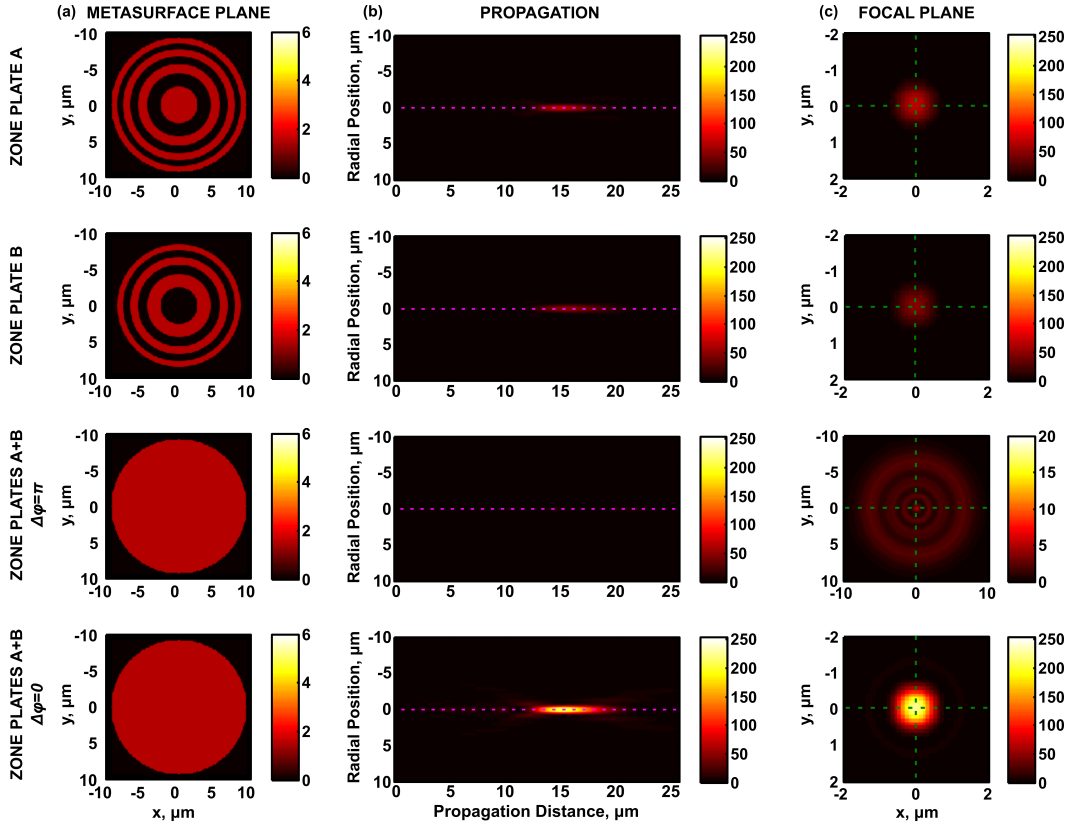


**Figure 5.11: Simulated results for turning a focusing zone plate into a diffracting aperture** by projecting inverted Fresnel zone plate patterns, A (row 1) and B (row 2) onto opposite sides of the metasurface. Coherent addition of patterns A and B on the metasurface results in the formation of an effective aperture for $\Delta\varphi = \pi$ (row 3), while an effective phase zone plate with a high intensity focal spot results from $\Delta\varphi = 0$ (row 4). (**a**) Simulated intensity on the metamaterial plane. (**b**) Simulated light distribution at different distances $z$ from the metasurface ($yz$-plane). The pink dotted line indicates the optical axis along which the focal depth is defined. (**c**) Simulated intensity distribution in the focal plane at $z = 15$ $\mu$m. Green dotted lines indicate the intensity cross-sections used to determine the focal diameter. All color scales show intensity.

To further clarify the underlying physics in this case it should be underlined that the coherent addition of zone patterns A and B does not arise from the spatial overlap

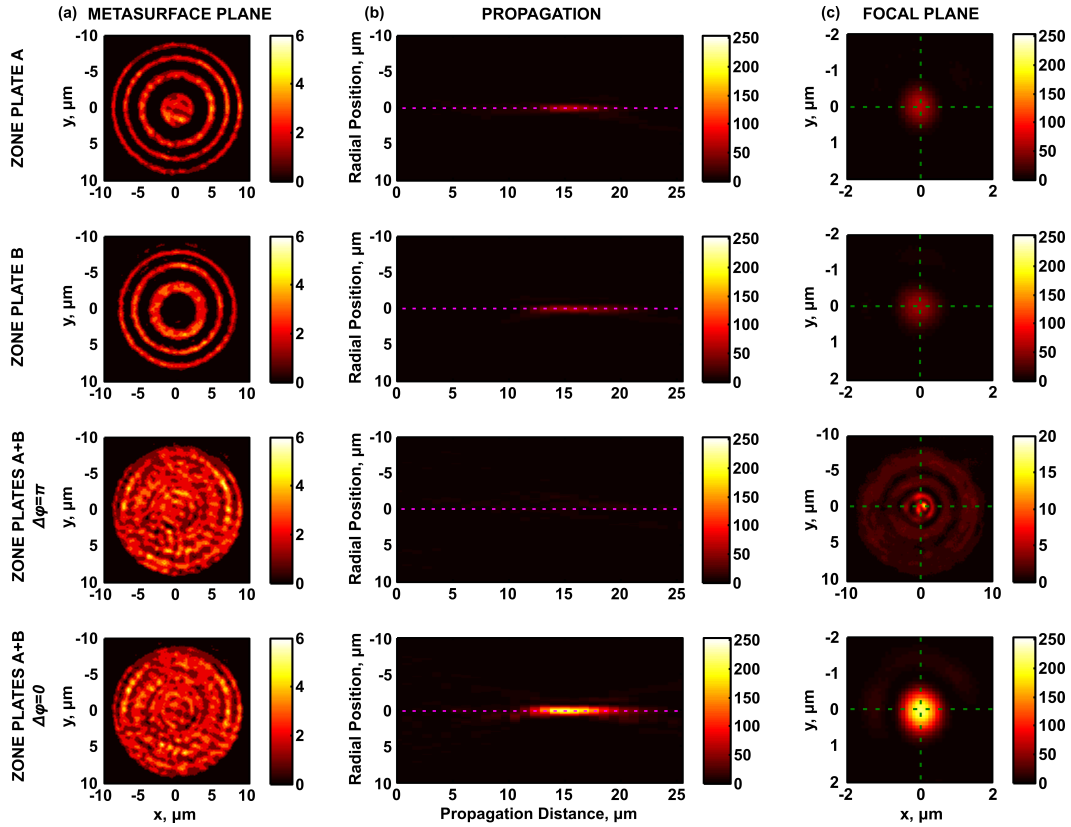


**Figure 5.12: Experimental results for turning a focusing zone plate into a diffracting aperture** by projecting inverted Fresnel zone plate patterns, A (row 1) and B (row 2) onto opposite sides of the metasurface. Coherent addition of patterns A and B on the metasurface results in the formation of an effective aperture for $\Delta\varphi = \pi$ (row 3), while an effective phase zone plate with a high intensity focal spot results from $\Delta\varphi = 0$ (row 4). Column (**a**): Images of the metamaterial plane taken with a camera. Column (**b**): Measured light distribution at different distances $z$ from the metasurface ($yz$-plane). The pink dotted line indicates the optical axis along which the focal depth is defined. Column (**c**): Measured intensity distribution in the focal plane at $z = 15$ $\mu$m. Green dotted lines indicated the intensity cross-sections used to determine the focal diameter. All color scales show intensity.

of zones on the metasurface, since the patterns are inverted. However, for coherent illumination, the resulting focusing behaviour in the system's output still depends on the relative phase difference of beams A and B since the focal spot creation by Fresnel zone plate patterns is a purely interference-based effect. In particular, the resulting focal spot is created by the transmission of structured zones of beam A and the reflection of zones of beam B (with a $\pi$ phase change). Therefore, for $\Delta\varphi = \pi$ all beam A and B light zones are directed in-phase towards the output, which is equivalent to the formation of a lens-sized aperture on the metasurface plane (row 3 in Figs. 5.11 - 5.13). On the contrary, for $\Delta\varphi = 0$ all the inverted plate pattern light zones are directed to the output

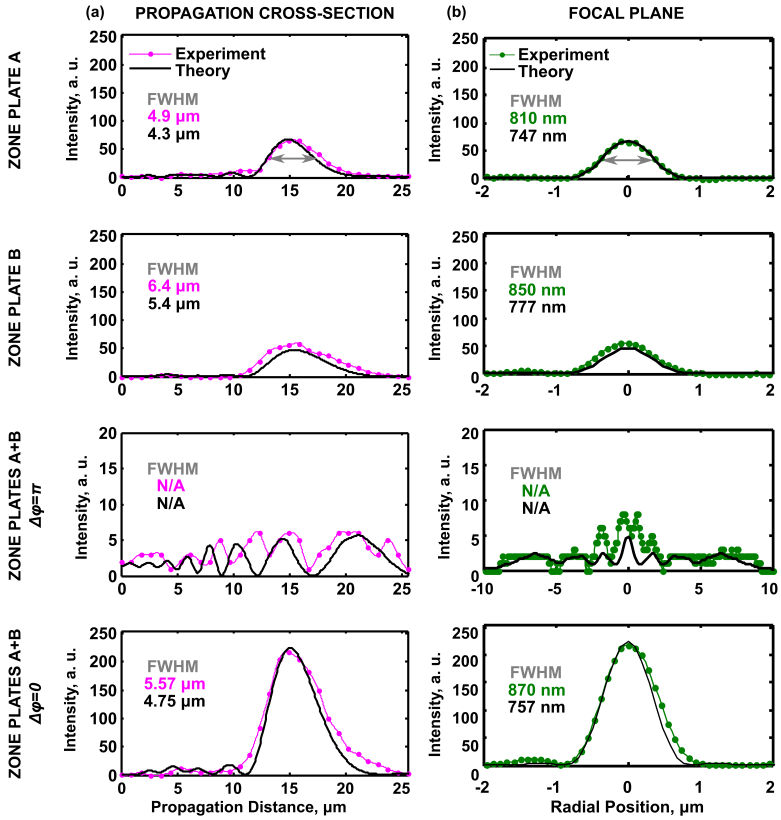


**Figure 5.13: Focal depth and diameter for inverted Fresnel zone plate patterns**, A (row 1) and B (row 2) projected onto opposite sides of the metasurface. Coherent addition of patterns A and B on the metasurface results in the formation of an effective aperture for $\Delta\varphi = \pi$ (row 3), while an effective phase zone plate with a high intensity focal spot results from $\Delta\varphi = 0$ (row 4). Column (**a**): Calculated (black solid lines) and measured (pink lines with data points) intensity distribution along the optical axis (indicated by pink dotted lines in Figs. 5.11 and 5.12). Column (**b**): Calculated (black solid lines) and measured (green lines with data points) radial intensity distribution in the focal plane at $z = 15$ $\mu$m, obtained by averaging cross-sections along $x$ and $y$ (indicated by green dotted lines in Figs. 5.11 and 5.12).

in anti-phase which is equivalent to the formation of a phase Fresnel zone plate on the metasurface (row 4 in Figs. 5.11 - 5.13).

It is worth comparing the coherent effects that arise from gradual coherent control of focal intensity as described in Section 5.3.2 with the coherent addition of inverted zone plates, see Fig. 5.14. As illustrated by Figs. 5.4 - 5.6, projection of identical zone plate patterns onto the metasurface allows control over the focal intensity in a way that corresponds to gradually interchanging the lens with a perfect absorber. This changes the intensity of the focal spot from "on" to "off" without affecting the structure of the spatial light distribution. On the other hand, projection of inverted zone plates on the

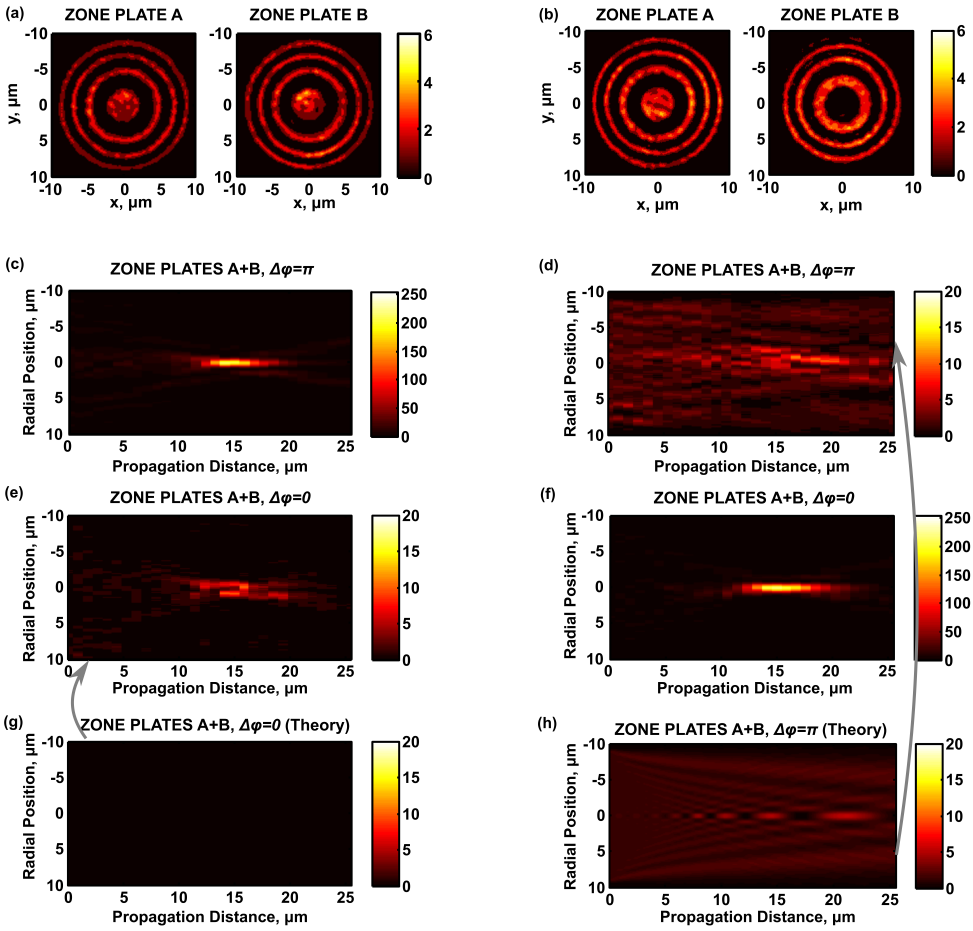


**Figure 5.14: From a focusing zone plate to a diffracting aperture or darkness.** Interaction of (**a**) identical and (**b**) inverted Fresnel zone plate patterns A and B on the metasurface (experimental results). When the transmitted lens pattern A and the reflected lens pattern B are in phase (which results from anti-phase impinging beams $\Delta\varphi = \pi$), identical zone plates yield a bright focal spot (**c**), while inverse zone plates add up to a diffracting circular aperture (**d**) and (**h**). When the transmitted and reflected zone plate patterns are out-of-phase (arising from $\Delta\varphi = 0$), identical zone plates block almost all light (**e**) and (**g**), while inverted zone plates focus (**f**). Panels **a** - **f** show experimental results, while **g** - **h** show simulations. For clarity, measured and simulated light propagation are shown on a reduced intensity scale for the effective aperture and absorber cases. All color scales show intensity.

metasurface as presented in Figs. 5.11 - 5.13 enables the effective transformation of an intensity Fresnel zone plate into a lens-sized clear aperture or a Fresnel phase zone plate. Comparison of the two cases reveals the creation of a similar focal spot from identical zone plates when $\Delta\varphi = \pi$ (Fig. 5.14 c) and inverted zone plates when $\Delta\varphi = 0$ (Fig. 5.14 f). However, Figs. 5.14 e, g and d, h clearly demonstrate different coherent behaviour between the intensity distributions created by identical zone plates for $\Delta\varphi = 0$ and

inverted zone plates for $\Delta\varphi = \pi$, respectively. It is clearly revealed numerically that in the first case (Fig. 5.14 g), all light is absorbed, whereas in the latter (Fig. 5.14 h) a lens is transformed into a lens-sized aperture illuminated by a plane wave, hence turning the intensity distribution of a focal spot into an aperture diffraction pattern. In the experimental measurements, the theoretically predicted 0 intensity in the "off" state ($\Delta\varphi = 0$ for identical zone plates), is on the order of a few percent (as explained above) as shown by Fig. 5.14 e using a different color scale for the low intensity light distribution. This response is still distinct from the clear aperture state illustrated by Fig. 5.14 d which has a different spatial intensity distribution that is consistent with the theoretically predicted clear aperture diffraction pattern (Fig. 5.14 h).

### 5.3.6 Theoretical description of all-optical tuning of the focal distance

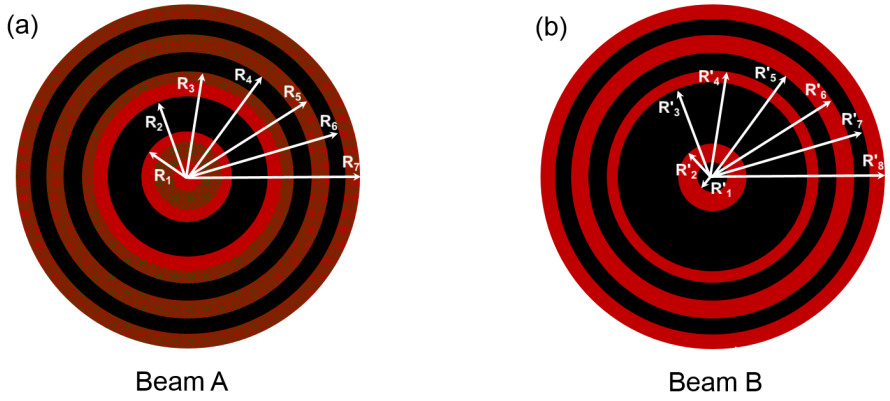


**Figure 5.15: Fresnel zone plate designs for dynamic control of the focal distance.** (**a**) Beam A Fresnel zone plate pattern design including 7 individual zones with radii given in Table 5.1. The shaded areas of beam A are coherently addressed by beam B Fresnel zone plate (**b**) which consists of zones that partially or fully overlap with beam A zones. Beam B zone radii are given in Table 5.2 and were calculated via variation of radii and zone combinations based on the zone plate in beam A in order to create distinctive focal lengths between nodes and anti-nodes of the standing wave. For both designs, transmissive and opaque design zones are represented by red and black, respectively.

Up to this point, experimental and theoretical demonstrations targeted dynamic tuning of focal intensity, depth and diameter based on two-dimensional coherent control for combinations of Fresnel zone plates designed to focus at a fixed common focal distance. This was achieved by coherent addition of Fresnel zone plates comprised of zones acquired from the same set of design radii given in Table 5.1. As a result, interesting

**Table 5.2:** Beam B Fresnel zone plate design radii for dynamic control of the focal distance calculated via optimizations of radii and zone combinations based on the zone plate design used for beam A (Table 5.1) in order to create distinct focal points at nodes and anti-nodes of the standing wave.

Fresnel zone plate design radii in $\mu$m

| $R'_1$ | $R'_2$ | $R'_3$ | $R'_4$ | $R'_5$ | $R'_6$ | $R'_7$ | $R'_8$ |
|---|---|---|---|---|---|---|---|
| 0.8 | 1.08 | 4.9 | 5.53 | 6.58 | 7.52 | 8.36 | 9.14 |

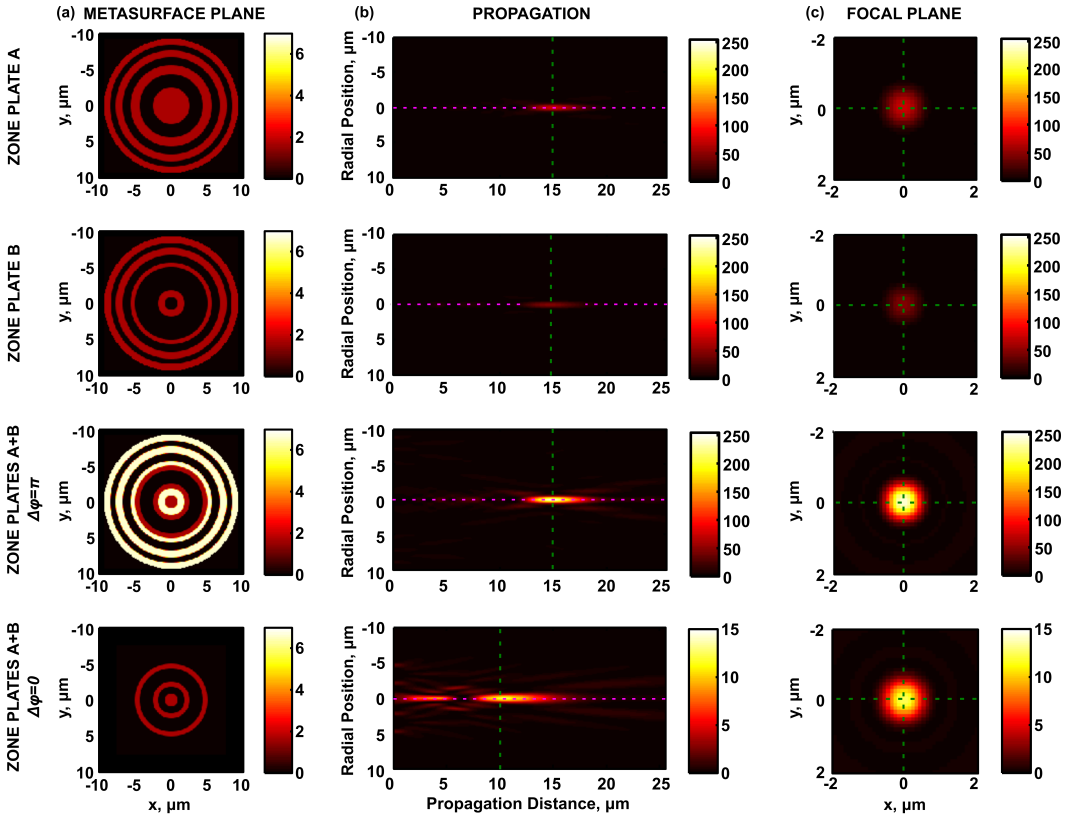


**Figure 5.16: Simulation results for controlling the focal distance** by projecting different Fresnel zone plate patterns, A (row 1) and B (row 2) onto opposite sides of the metasurface. Coherent interaction of patterns A and B on the metasurface leads to a high-intensity focus at $z = 15$ $\mu$m for $\Delta\varphi = \pi$ (row 3), while $\Delta\varphi = 0$ (row 4) results in a dimmer focus at $z = 10.3$ $\mu$m with a slightly increased focal depth and diameter. (**a**) Simulated intensity on the metamaterial plane. (**b**) Simulated light distribution at different distances $z$ from the metasurface ($yz$-plane). The pink dotted line indicates the optical axis along which the focal depth is defined. The green dotted line indicates the focal plane in each case. (**c**) Simulated intensity distribution in the focal plane at $z = 15$ $\mu$m for rows 1, 2 and 3 and at $z = 10.3$ $\mu$m for row 4. Green dotted lines indicate the intensity cross-sections used to determine the focal diameter. All color scales show intensity.

possibilities arose from alternating illumination and absorption of different zone combinations leading to adjustable intensity, depth and diameter of the created focal spot, see Figs. 5.4 - 5.13.

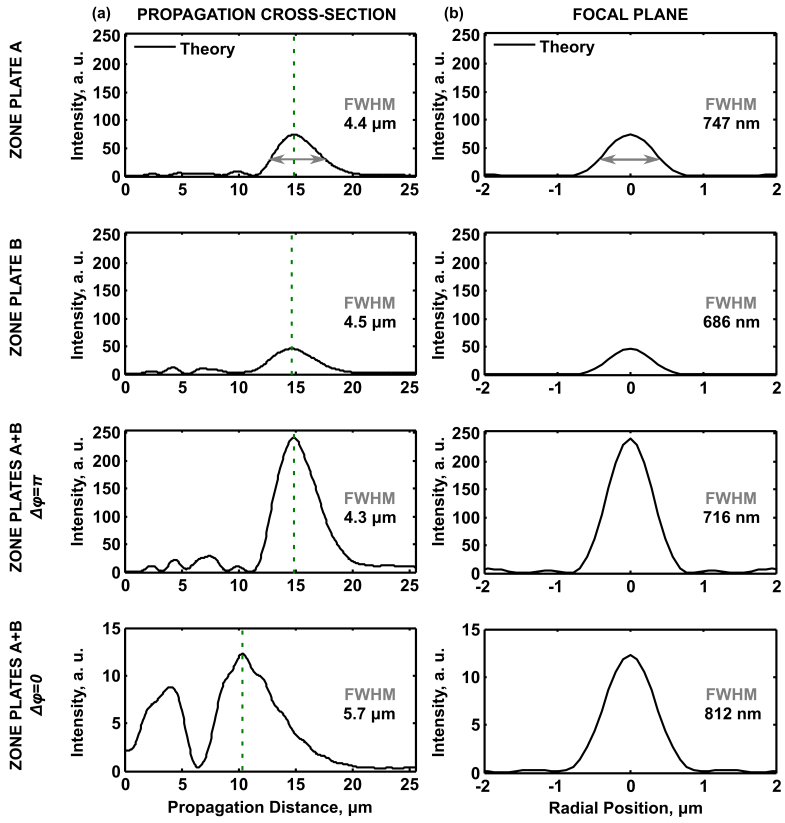


**Figure 5.17: Focal depth and diameter for different zone plate patterns targeting tuning of the focal distance.** Zone plate A (row 1) and B (row 2) projected onto opposite sides of the metasurface. Coherent interaction of patterns A and B on the metasurface leads to a high-intensity focus at $z = 15$ $\mu$m for $\Delta\varphi = \pi$ (row 3), while $\Delta\varphi = 0$ (row 4) results in a dimmer focus at $z = 10.3$ $\mu$m with a slightly increased fodal depth and diameter. Column (**a**): Calculated intensity distribution along the optical axis (indicated by pink dotted lines in Fig. 5.16. The green dotted line indicates the focal distance in each case. Column (**b**): Calculated radial intensity distribution in the focal plane at $z = 15$ $\mu$m for rows 1, 2 and 3 and at $z = 10.3$ $\mu$m for row 4, obtained by averaging cross-sections along $x$ and $y$ (indicated by green dotted lines in Figs. 5.16.

Interestingly, the presented approach can in principle provide control over the targeted focal distance and therefore constitute a fully flexible all-optical dynamic focusing device. In particular, an additional degree of freedom can be introduced in the system if partial zone overlap between beam A and beam B designs is considered. In this way, coherent addition of beam A and beam B can alter the central zone radii, on which the focal distance depends strongly, as well as the total number of resulting zones and their radii (based on Eq. 5.1).

A simple example of all-optical dynamic tuning of the focal distance is theoretically presented here by addressing parts of the same Fresnel zone plate design in beam A

that was used in previous demonstrations (see Fig. 5.2 and Table 5.1) via a beam B pattern including zones that partially overlap with those of beam A as well as some identical to beam A zones, see Fig. 5.15. The zone radii of the zone plate for beam B were chosen by varying the radii of the initial design for beam A as given by Table 5.1 aiming to create two distinct focal points at the states of *coherent perfect transparency* and *coherent perfect absorption* via coherent addition of beam A and B on the *ideal thin absorber*. Zone radii were varied such that pattern zone widths to be projected via the conventional imaging optics of the current experimental setup do not exceed the spatial resolution limit of the system (see Section 4.6). Radical change of the radius of the central zone as well as variation of the total number of illuminated zones that contribute to focusing can induce noticeable changes in the focal distance $f$ based on Eq. 5.1.

Figs. 5.16 - 5.17 clearly show tuning of the resulting focal distance between the states of *coherent perfect transparency* ($\Delta\varphi = \pi$) and *coherent perfect absorption* ($\Delta\varphi = 0$) for the zone plate designs of Fig. 5.15 a and b. Zone plates A and B create similar focal spots around the initial design focal distance of $z = 15$ $\mu$m (row 1 and 2 in Figs. 5.16 - 5.17). Their coherent interaction on an *ideal thin absorber* results in a focal spot at $z = 15$ $\mu$m for $\Delta\varphi = \pi$ and at $z = 10.3$ $\mu$m for $\Delta\varphi = 0$. This translation of the focal distance by $\Delta f = 4.7$ $\mu$m corresponds to a 31% change in $f$. It should be noted that the focal spot at $z = 10.3$ $\mu$m is much dimmer as it is created from a reduced total area of bright zones. It has 96 nm wider focal diameter, 1.4 $\mu$m longer focal depth and its intensity is about 5% of the peak intensity of the focal spot created at $z = 15$ $\mu$m when $\Delta\varphi = \pi$. The difference in focal intensities could be compensated by modulating the laser intensity or reduced by zone plate design.

The simple theoretical demonstration of Figs. 5.16 - 5.17 is targeting dynamic tuning of the focal distance using the same Fresnel zone plate in beam A that was previously used to control other focal properties and was subject to experimental limitations of the existing experimental setup (e.g. spatial resolution, design wavelength, imaging optics, scanning range). Dynamic tuning of the focal distance by 31% is obtained by straightforward empirical tuning of pattern B radii. In theory, beam A and beam B designs could be meticulously optimized to provide larger changes in the focal distance and more balanced intensity levels of the resulting focal spot between standing wave node and anti-node extremes. Moreover, complex intensity distributions including multiple

focal spots along the optical axis could be accessed by optimizing pattern combinations with a larger number of zones. Such optimization processes could be investigated further in the future. In all cases, the alteration between focal spots could be ultrafast (10s of GHz bandwidth of commercial phase modulators, up to 100 THz coherent absorption bandwidth) [108, 109] and operated at arbitrarily low intensity levels [107].

## 5.4 Summary

In summary, dynamic control over optical focusing is demonstrated by projecting Fresnel zone plate patterns onto opposite sides of a metasurface using coherent light. Control of focal intensity from "on" to "off", focal depth with a dynamic range of 100%, focal diameter by 35%, focal distance by 31% and effective replacement of a lens by an aperture is reported based on an all-optical platform without moving parts. Experimental demonstrations include the tuning of focal intensity, depth and diameter as well as the transition from a lens to a lens-sized aperture for the cases of a metasurface absorber placed at a standing wave node and anti-node. Continuous control of focal intensity, depth and diameter as well as dynamic tuning of the focal distance are theoretically described. Throughout all experiments, experimental results closely match theoretical predictions that were based on the angular spectrum method [201, 202]. Focusing is controlled by an optical phase modulator, implying that tens of GHz modulation bandwidth can be accessed with telecommunications phase modulators, while the underlying light-matter interaction could deliver femtosecond-scale switching times [108, 109].

Although Fresnel zone plate patterns written in metal films are employed, it does not matter how the light fields that are imaged onto the metasurface are created. Conventional lenses, lens arrays, gratings, holograms or other optical elements may be imaged onto the metasurface instead. Therefore, this approach may be applied to achieve fast modulation of various optical functionalities. By imaging the metasurface itself onto a different plane — such as the camera in the presented experiments — the dynamic focusing or other functionality can be applied outside of the interferometer.

As already discussed in previous Chapters, although the current demonstrations are underpinned by coherent control of metasurface absorption, similar schemes could be established based on coherent control of state of polarization [113] or refraction [104] of light. Moreover, the presented configuration is compatible with arbitrarily low

intensities [107]. Combined with the system's compatibility with ultrafast switching times [108, 109], this proof-of-principle demonstration of metasurface-based all-optical dynamic focusing could add a multi-functional, all-optical, ultrafast component to next generation, coherent focusing, imaging and microscopy platforms that can operate with minimum intensity requirements and without moving parts.

# Chapter 6

# Conclusions

## 6.1 Summary

This thesis studies two-dimensional coherent control of light with light on absorptive metasurfaces and its potential applications in a diverse range of fields theoretically and experimentally. Coherent control of metasurface functionalities has been previously reported as a means of all-optical tuning of manifestations of absorption, refraction, anisotropy and optical activity without nonlinearity. Moreover, it was proven to be operable at modulation rates of up to 100 THz and single photon intensities.

In this thesis, the main advancement is *spatially addressable* coherent switching between *coherent perfect trasparency* and *coherent perfect absorption* on an absorptive metasurface, which led to a number of diverse application examples that were theoretically described and experimentally demonstrated for the first time in this work:

- **All-optical logical operations XOR, XNOR, AND, OR between coherent two-dimensional light distributions** were demonstrated in a proof-of-principle experiment based on spatially distributed *coherent perfect transparency* and *coherent perfect absorption* in a nanostructured plasmonic metasurface. On this basis, potential applications of two-dimensional control of light with light for **multichannel logic in future coherent photonic and telecommunications networks** were suggested and explored. It was demonstrated how two-dimensional coherent control of absorption of light can be used to perform Boolean logic (XOR, XNOR, AND, OR) as well as demultiplexing functions between simple representations of spatially multiplexed channels carrying phase- and/or intensity-encoded

information. Up to 17 dB contrast between logical "1" and "0" was achieved experimentally.

- A theoretical framework for performing optical **set operations between binary images** was introduced and experimentally demonstrated on the first metasurface-based platform that performs all-optical **pattern recognition** and **image analysis** using coherent light. The comparison of pairs of patterns or images under the regimes of *coherent perfect transparency* and *coherent perfect absoprption* in a plasmonic metasurface provided real time and software-free **qualitative and quantitative** analysis of the degree of pattern or image agreement, thus revealing similarities and differences between pairs. Quantitative results were extracted based on three power values of electronic data acquired by a single photodetector. Simple system calibration can guarantee high experimental accuracy both qualitatively and quantitatively as long as any experimental deficiencies arising from misaligned components are smaller than the feature size of the images or patterns to be examined.

- **All-optical control of focusing of light** based on coherent interaction of light with light on a plasmonic metasurface absorber was demonstrated for the first time. By projecting Fresnel zone plate patterns onto opposite sides of the metasurface using coherent light, an effective dynamic zone plate controlled by a light modulator was created on the metasurface plane. Simulations and experiments reveal continuous control of the **focal intensity** from "on" to "off", the **focal depth** by 100%, the **focal diameter** by 35% and the **focal distance** by 31%. Furthermore, an intensity Fresnel zone plate can be effectively transformed to a phase Fresnel zone plate or a lens-sized clear aperture which removes any focusing characteristics from the system. The employed experimental platform did not rely on any moving components or inherent material nonlinearities and therefore can in principle provide dynamic switching of focal properties on femtosecond timescales defined by the response time of the underlying coherent absorption effect. In practice, the system's response time will always be determined by the employed phase modulator and can therefore reach tens of GHz modulation bandwidths accessible by telecommunications phase modulators. The technique would work for any diffracting element, lens, hologram or other optical element, thus paving the way to the modulation of various functionalities. The presented application

essentially proved the capability of metasurface-based two-dimensional coherent control to manipulate light in three dimensions.

- The first **metasurface-based imaging interferometer** for manipulation of coherent light with light in two dimensions was designed and built for the purposes of this thesis. The fundamental components of this device were a standing wave interferometer combined with conventional imaging optics projecting two-dimensional light distributions (inputs) on either side of a free-standing gold absorptive metasurface of deep sub-wavelength thickness. The system was tuned between the extremes of *coherent perfect transparency* and *coherent perfect absorption* by varying the relative phase difference between the input beams leading to the spatially selective transmission and absorption of inputs, respectively. The coherent interaction result (output) was monitored by an imaging detector. The minimum feature to be resolved by the optical platform was theoretically discussed and experimentally measured to be $1.14\lambda$ for $\lambda = 790$ nm. A slight deterioration relative to a theoretical diffraction-limited spot is attributed to system aberrations as well as surface roughness and flatness imperfections of the fabricated absorbing metasurface.

In conclusion, the versatility of metasurface-based two-dimensional coherent control of light with light was theoretically established and experimentally proven for a diverse range of functionalities throughout this thesis. The accessibility of various optical functionalities at a vast range of wavelengths via metasurface design in conjunction with theory and applications of two-dimensional coherent control of light with light presented in this work renders metasurfaces, metadevices and 2D coherent control relevant to research on future coherent photonic and telecommunication systems as well as computing, imaging and focusing elements and devices.

## 6.2 Outlook

The theoretical and experimental demonstrations of this thesis established the framework of coherent all-optical manipulations of two-dimensional binary light intensity distributions on absorptive metasurfaces with applications in all-optical logic, spatial channel demultiplexing, image processing, pattern recognition and dynamic focusing. The versatility of these "proof of concept" demonstrations can be diversified further by making use of additional degrees of freedom in the system.

Although metasurface absorption was spatially addressed in the coherent control regime in all of the presented schemes, any metasurface functionality could be coherently addressed with spatial resolution. For instance, an anisotropic low-loss metamaterial could be employed in a similar configuration in order to access polarization-based logical operations between two-dimensional signals with negligible loss. This alternative expression of the system's functionality would provide a more realistic solution for future telecommunications and photonic networks where any source of loss is undesirable and polarization-encoded signals are commonly used. Furthermore, the very nature of metamaterial science lies in the fact that appropriate engineering of the metamaterial design could transfer the desirable functionality to any wavelength range or a combination of wavelengths. Therefore, meticulous design of the coherently addressed metasurface could provide a selective expression of the metamaterial functionality throughout a desirable wavelength range. Consequently, two-dimensional coherent control of metasurface functionalities could operate with wavelength division multiplexed signals. Taking into account the ultrafast speed and single photon intensity compatibility of the underpinning effect, such a proof-of-principle experiment could be evolved to match the requirements of spatially multiplexed signal manipulation in future coherent photonic devices, networks and telecommunications systems. Considering that the approach relies on the phase difference between input signals and therefore phase stability, its application to local systems and on-chip integrated photonic implementations will be more favourable than in large-scale fibre network applications.

The possibility of performing massively parallel Boolean logic optically without relying on slow and energy-demanding nonlinearities unlocks opportunities for all-optical computing. Notably, the presented experimental realization of all-optical logical operations has the main characteristics of a Turing machine operating on analogue inputs represented by two-dimensional distributions of light intensities. The computational potential of the presented scheme could be further evaluated in future work targeting parallel lossless all-optical computations based on spatially addressable coherent control of the expression of metasurface anisotropy. Such computations can in principle form an ultra-fast, energy-efficient, transparent coherent optical logic device that will be free from pre- and post-processing software. However, phase stability throughout the network will be challenging depending on network dimensions and cascadability of the presented single-step logical functions may require signal regeneration/amplification for

the output of one logical operation to form an input of the next.

Apart from all-optical coherent telecommunications- and computing-oriented applications, two-dimensional coherent control of light with light on metasurfaces could be the basis of functional components for imaging and microscopy systems operating with coherent light. For sample monitoring, the presented qualitative and quantitative pattern recognition and image analysis scheme could be in principle applied to the output of any microscope via the projection of the tested sample on a metasurface that is simultaneously illuminated by a second coherent structured beam that is controlled by a phase retarder. Depending on the application, the profile of the second coherent beam could be adapted to provide real-time mapping and quantification of sample similarities and differences in comparison to features of the structured reference beam. For instance, object classification could be achieved by comparing sample images of various shapes to a range of predefined shapes imposed on the structured reference beam in the regimes of *coherent perfect absorption* and *coherent perfect transparency*. Similarly, comparison of a set of biological cells to the structure of a healthy biological cell imprinted on the second coherent beam could reveal a qualitative and quantitative description of the healthy and unhealthy cell parts. Although the suggested configuration may appear complex to implement, it should be underlined that such a tool will not involve any image post-processing and can in principle be operated with up to 100 THz bandwidth and arbitrarily low intensities.

In a similar context, the all-optical control of focusing of light as demonstrated in this thesis, could enhance the performance of coherent focusing or imaging devices. In this case, the system's incoming illumination will be coherently modified on a metasurface by a second coherent two-dimensional beam profile that is controlled by a phase retarder before entering the focusing/imaging part of the device. As a result, focusing of incoming light can be controlled continuously between the extremes achieved in the *coherent perfect absorption* and *coherent perfect transparency* states. For instance, sample images can be acquired at different focal distances by varying the relative beam phase difference imposed by the phase retarder. Essentially, the output of the all-optical dynamic focusing scheme that was presented in Chapter 5 can form the input of a focusing or imaging device and can therefore provide modulation of its focusing characteristics without moving parts and in principle with sub-nanosecond response times based on commercially available phase modulators.

From a technical point of view, further advancements to the existing experimental imaging interferometer could enrich the capabilities of the presented schemes. Throughout this work, binary intensity masks were employed to structure the coherent interacting wavefronts and a variable liquid crystal was employed to uniformly vary the phase of one input beam, thus controlling the relative position of the standing wave with respect to the metasurface. A simple yet rather intriguing extension of these demonstrations would be unlocked by the use of phase masks and/or a spatial light modulator in either interferometer arm in order to simultaneously control the spatially distributed intensity and phase of the interacting two-dimensional light distributions. Such an advancement would considerably add to the system's potential application in demultiplexing complex combinations of spatially multiplexed telecommunications signals. Moreover, the use of gray-scale instead of binary intensity images could add an extra degree of freedom, especially in the area of image processing and dynamic focusing. The accessibility of different functionalities and multiple wavelength operation, as discussed above, could be achieved by metasurface design and is equally relevant to computing, imaging and focusing applications, where sample or data characterization also relies on the spectral and polarization characteristics of light. Given that *coherent perfect absorption* has been demonstrated with single as well as entangled photons [107, 152, 207], two-dimensional control of light with coherent light promises opportunities in quantum optics, for example for quantum imaging applications. Lastly, two-dimensional control of light with light on metasurfaces could be in principle applied in a fibre-based environment, thus permitting the introduced concepts to be translated to their fibre-based counterparts.

# Appendix A

# Ideal thin absorber

Here, the fundamental maximum of thin film absorption is derived as presented in [27, 116, 117] following the configuration depicted in Fig. A.1.

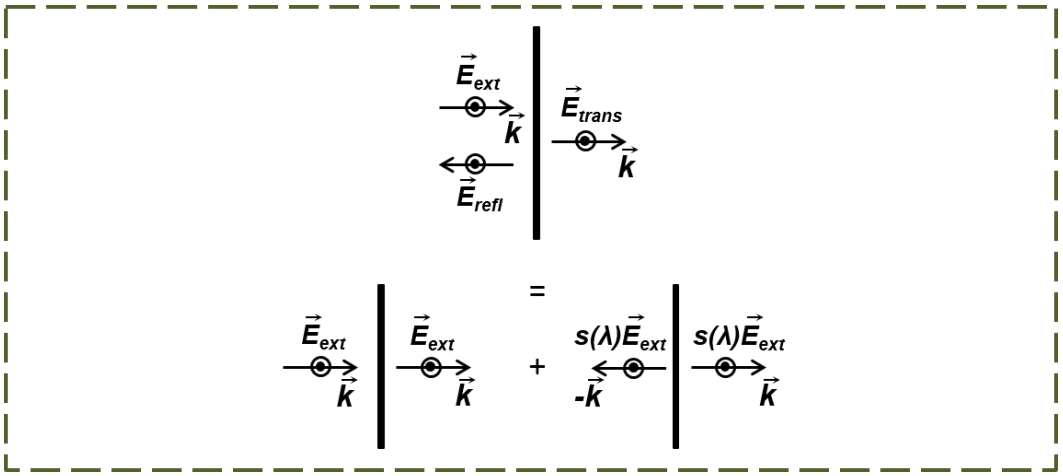


**Figure A.1: Field symmetry after scattering by a thin film.** The same medium is considered on both sides of the film.

In all cases, the experiments are conducted in free space, hence air is assumed on either side of the sample. Moreover, the sample is illuminated at normal incidence. As explained in the main text and in [208], single single layer films of deep sub-wavelength thickness will mainly couple to the electric field at normal incidence.

Considering only the thin film under single beam plane wave illumination at normal incidence, the impinging field phase accumulation within the film is minuscule (excluding high refractive index dielectrics). This results in symmetric field scattering as illustrated in Fig. A.1. The scattered field is of equal amplitude in the forward and backward

directions [116], wavelength dependent and is accordingly described by the complex $s(\lambda)$ coefficient. Therefore, reflection $r(\lambda)$ and transmission $t(\lambda)$ coefficients are

$$r(\lambda) = s(\lambda) \qquad \text{and} \qquad t(\lambda) = s(\lambda) + 1 = r(\lambda) + 1 \tag{A.1}$$

The level of absorption exhibited by incident light on such a film is:

$$A = 1 - |r|^2 - |t|^2 \tag{A.2}$$

Absorption can only be maximized if scattered and incident fields destructively interfere, which implies that absorption will be maximized by a real negative scattering coefficient. Therefore, the absorption maximum is accessed by the zeros of the derivative $\frac{\partial A}{\partial s(\lambda)}$ for which the second derivative is real and negative. This calculation yields:

$$s(\lambda) = -0.5 \qquad \text{for which} \qquad t(\lambda) = -r(\lambda) = 0.5 \tag{A.3}$$

For these values, the absolute maximum of thin film absorption in air under single beam illumination is:

$$A_{Thinfilm}^{Max} = 0.5 \tag{A.4}$$

which is the fundamental theoretical maximum of single beam absorption achievable by a thin film that can be well-approximated by a single planar scattering interface.

# Appendix B

# Publications and awards

## B.1 Journal publications

- M. Papaioannou, E. Plum, E. T. F. Rogers and N. I. Zheludev. "All-optical dynamic focusing of light via coherent absorption in a plasmonic metasurface". *Light Sci. Appl.*, (In press).

- M. Papaioannou, E. Plum and N. I. Zheludev. "All-optical pattern recognition and image processing on a metamaterial beam splitter". *ACS Photonics*, 4(2):217, 2017.

- M. Papaioannou, E. Plum, J. Valente, E. T. F. Rogers and N. I. Zheludev. "All-optical multichannel logic based on coherent perfect absorption in a plasmonic metamaterial". *APL Photonics*, 1:090801, 2016.

- M. Papaioannou, E. Plum, J. Valente, E. T. F. Rogers and N. I. Zheludev. "Two dimensional control of light with light on metasrfaces". *Light Sci. Appl.*, 5:e1670, 2016.

## B.2 Conference contributions

- (poster) E. Plum, M. Papaioannou, A. Xomalis, Y. Jung, I. Demirtzioglou, E. T. F. Rogers, K. F. MacDonald, P. Petropoulos, David J. Richardson and N. I. Zheludev. "Coherent all-optical information processing on metasurfaces". *META2017*, Seoul, South Korea, 25 - 28 Jul 2017

- (invited) E. Plum, M. Papaioannou, P. Cencillo-Abad, J. Y. Ou, A. Xomalis, E. T. F. Rogers, K. F. MacDonald, and N. I. Zheludev. "Active metasurfaces: Optical properties on demand". *Rank Prize Symposium on Electromagnetic Metasurfaces*, Grasmere, UK, 13 - 16 Mar 2017

- (Oral) M. Papaioannou, E. Plum, E. T. F. Rogers, J. Valente and N. I. Zheludev. "All-optical image recognition using metamaterials". *Frontiers in Optics/Laser Science 2016*, Rochester, NY, USA, 17 - 21 Oct 2016

- (Oral) M. Papaioannou, E. Plum, E. T. F. Rogers, J. Valente and N. I. Zheludev. "Metasystems for all-optical recognition and processing of images and data". *Metamaterials 2016*, Crete, Greece, 17 - 22 Sep 2016

- (poster) M. Papaioannou, E. Plum, E. T. F. Rogers, J. Valente, B. Gholipour, N. I. Zheludev. "All-optical image recognition and processing with plasmonic metasurfaces". *CLEO 2016*, San Jose, CA, USA, 5 - 10 June 2016

- (oral) M. Papaioannou, E. Plum, E. T. F. Rogers, J. Valente, N. I. Zheludev. "All-optical image recognition and processing with plasmonic metasurfaces". *New Horizons in Nanophotonics*, Chicheley, UK, 23 - 24 May 2016

- (oral) J. Valente, E. Plum, M. Papaioannou, P. Cencillo-Abad, V. Nalla, C. Altuzarra, S. Vezzoli, I. J. Youngs, and N. I. Zheludev. "Active control of light with metasurfaces". *Defence & Security Doctoral Symposium*, Cranfield, UK, 25 - 26 Nov 2015

- (oral) M. Papaioannou, E. Plum, J. Valente, E. T. F. Rogers and N. I. Zheludev. "Coherent image processing with plasmonic metasurfaces". *Metamaterials 2015*, Oxford, UK, 7 - 12 Sep 2015

- (oral) M. Papaioannou, E. Plum, J. Valente, E. T. F. Rogers and N. I. Zheludev. "Dynamic mode multiplexing with plasmonic metasurfaces". *CLEO/Europe-EQEC 2015*, Munich, Germany, 21 - 25 Jun 2015

- (poster) M. Papaioannou, E. Plum, E. T. F. Rogers and N. I. Zheludev. "Image processing using coherent absorption". *Nanometa 2015*, Seefeld, Austria, 5 - 8 Jan 2015

## B.3 Awards

- (Finalist) Emil Wolf Student Paper Competition. *Frontiers in Optics/Laser Science 2016*, Rochester, NY, USA, 17 - 21 Oct 2016
- ($3^{rd}$ Place) Student Poster Competition. *Future Photonics Hub Industry Day 2016*, Southampton, UK, 13 Sep 2016
- ($1^{st}$ Place) IOP Publishing Student Poster Award. *Nanometa 2015*, Seefeld, Austria, 5 - 8 Jan 2015

# Bibliography


[1] T. Feurer, J. C. Vaughan, and K. A. Nelson. "Spatiotemporal coherent control of lattice vibrational waves". *Science*, 299(5605):374–377, 2003.

[2] P. Brumer and M. Shapiro. "Coherence chemistry: Controlling chemical reactions with lasers". *Accounts of chemical Research*, 22(12):407–413, 1989.

[3] N. Dudovich, D. Oron, and Y. Silberberg. "Single-pulse coherently controlled nonlinear Raman spectroscopy and microscopy". *Nature*, 418:512–514, 2002.

[4] D. Goswami. "Optical pulse shaping approaches to coherent control". *Physics Reports*, 374(6):385–481, 2003.

[5] M. P. A. Branderhorst, P. Londero, P. Wasylczyk, C. Brif, R. L. Kosut, H. Rabitz, and I. A. Walmsley. "Coherent control of decoherence". *Science*, 320(5876):638–643, 2008.

[6] Y. Silberberg. "Quantum coherent control for nonlinear spectroscopy and microscopy". *Annual Review of Physical Chemistry*, 60(1):277–292, 2009.

[7] I. Barmes, S. Witte, and K. S. E. Eikema. "Spatial and spectral coherent control with frequency combs". *Nature Photonics*, 7:38–42, 2013.

[8] M. Soljačić and J. D. Joannopoulos. "Enhancement of nonlinear effects using photonic crystals". *Nature Materials*, 3:211–219, 2004.

[9] V. R. Almeida, C. A. Barrios, R. R. Panepucci, and M. Lipson. "All-optical control of light on a silicon chip". *Nature*, 431:1081–1084, 2004.

[10] M. Ren, B. Jia, J.-Y. Ou, E. Plum, J. Zhang, K. F. MacDonald, A. E. Nikolaenko, J. Xu, M. Gu, and N. I. Zheludev. "Nanostructured plasmonic medium for Terahertz bandwidth all-optical switching". *Advanced Materials*, 23(46):5540–5544, 2011.

[11] M. I. Stockman. "Ultrafast nanoplasmonics under coherent control". *New Journal of Physics*, 10:025031, 2008.

[12] M. Aeschlimann, M. Bauer, D. Bayer, T. Brixner, F. J. García de Abajo, W. Pfeiffer, M. Rohmer, C. Spindler, and F. Steeb. "Adaptive subwavelength control of nano-optical fields". *Nature*, 446:301–304, 2007.

[13] T. S. Kao, S. D. Jenkins, J. Ruostekoski, and N. I. Zheludev. "Coherent control of nanoscale light localization in metamaterial: Creating and positioning isolated subwavelength energy hot spots". *Physical Review Letters*, 106(8):085501, 2011.

[14] M. I. Stockman, S. Faleev, and D. J. Bergman. "Coherent control of femtosecond energy localization in nanosystems". *Physical Review Letters*, 88(6):067402, 2002.

[15] X. Li and M. I. Stockman. "Highly efficient spatiotemporal coherent control in nanoplasmonics on a nanometer-femtosecond scale by time reversal". *Physical Review B*, 77(19):195109, 2008.

[16] B. Gjonaj, J. Aulbach, P. M. Johnson, A. P. Mosk, L. Kuipers, and A. Lagendijk. "Active spatial control of plasmonic fields". *Nature Photonics*, 5:360–363, 2011.

[17] D. Brinks, M. Castro-Lopez, R. Hildner, and N. F. van Hulst. "Plasmonic antennas as design elements for coherent ultrafast nanophotonics.". *Proceedings of the National Academy of Sciences of the United States of America*, 110(46):18386–18390, 2013.

[18] S. Kosmeier, A. C. De Luca, S. Zolotovskaya, A. Di Falco, K. Dholakia, and M. Mazilu. "Coherent control of plasmonic nanoantennas using optical eigenmodes". *Scientific Reports*, 3:1808, 2013.

[19] M. Miyata and J. Takahara. "Excitation control of long-range surface plasmons by two incident beams.". *Optics Express*, 20(9):9493–9500, 2012.

[20] S. Longhi, Y. D. Chong, L. Ge, H. Cao, and A. D. Stone. "Backward lasing yields a perfect absorber". *Physics*, 3(105), 2010.

[21] S. Tuccio, M. Centini, A. Benedetti, and C. Sibilia. "Subwavelength coherent control and coupling of light in plasmonic nanoresonators on dielectric waveguides". *Journal of the Optical Society of America B*, 30(2):450–455, 2013.

[22] Y. D. Chong, L. Ge, H. Cao, and A. D. Stone. "Coherent perfect absorbers: Time-reversed lasers". *Physical Review Letters*, 105(5):053901, 2010.

[23] W. J. Wan, Y. D. Chong, L. Ge, H. Noh, A. D. Stone, and H. Cao. "Time-reversed lasing and interferometric control of absorption". *Science*, 331(6019):889–892, 2011.

[24] S. Dutta-Gupta, O. J. F. Martin, S. Dutta-Gupta, and G. S. Agarwal. "Controllable coherent perfect absorption in a composite film". *Optics Express*, 20(2):1330–1336, 2012.

[25] S. Zanotto, F. P. Mezzapesa, F. Bianco, G. Biasiol, L. Baldacci, M. S. Vitiello, L. Sorba, R. Colombelli, and A. Tredicucci. "Perfect energy-feeding into strongly coupled systems and interferometric control of polariton absorption". *Nature Photonics*, 10:830–834, 2014.

[26] R. Fleury, D. Sounas, A. Alù, A. D. Stone, and X. Zhang. "An invisible acoustic sensor based on parity-time symmetry". *Nature Communications*, 6:5905, 2015.

[27] J. Zhang, C. Guo, K. Liu, Z. Zhu, W. Ye, X. Yuan, and S. Qin. "Coherent perfect absorption and transparency in a nanostructured graphene film". *Optics Express*, 22(10):12524–12532, 2013.

[28] J. Zhang, K. F. MacDonald, and N. I. Zheludev. "Controlling light-with-light without nonlinearity". *Light: Science & Applications*, 1:e18, 2012.

[29] N. I. Zheludev. "What diffraction limit?". *Nature Materials*, 7:420–422, 2008.

[30] D. R. Smith, J. B. Pendry, and M. C. K. Wiltshire. "Metamaterials and negative refractive index". *Science*, 305(5685):788–792, 2004.

[31] D. R. Smith, Willie J. Padilla, D. C. Vier, S. C. Nemat-Nasser, and S. Schultz. "Composite medium with simultaneously negative permeability and permittivity". *Physical Review Letters*, 84(18):4184–4187, 2000.

[32] E. Plum, K. Tanaka, W. T. Chen, V. A. Fedotov, D. P. Tsai, and N. I. Zheludev. "A combinatorial approach to metamaterials discovery". *Journal of Optics*, 13:055102, 2011.

[33] N. Papasimakis, V. A. Fedotov, Y. H. Fu, D. P. Tsai, and N. I. Zheludev. "Coherent and incoherent metamaterials and the order-disorder transitions". *Physical Review B*, 80(4):041102, 2008.

[34] M. Shalaev, V. M. Cai. *Optical Metamaterials: Fundamentals and Applications*. New York: Springer, 2010.

[35] V. G. Veselago. "The electrodynamics of substances with simultaneously negative values of $\epsilon$ and $\mu$". *Soviet Physics Uspekhi*, 10(4):509–514, 1968.

[36] A. J. Pendry, J. B. Holden, D. J. Robbins, and W. J. Stewart. "Magnetism from conductors and enhanced nonlinear phenomena". *IEEE Transaction on Microwave Theory and Techniques*, 47(11):2075–2084, 1999.

[37] J. Brown. "Artificial dielectrics having refractive indices less than unity". *Proceedings of the IEE - Part IV: Institution Monographs*, 100(5):51–62, 1953.

[38] W. Rotman. "Plasma simulation by artificial dielectrics and parallel-plate media". *IRE Transactions on Antennas and Propagation*, 12(1):82–95, 1962.

[39] R. Shelby, D. Smith, and S. Schultz. "Experimental verification of a negative index of refraction". *Science*, 292(5514):77–79, 2001.

[40] J. B. Pendry. "Negative refraction makes a perfect lens". *Physical Review Letters*, 85(18):3966–3969, 2000.

[41] A. Grbic and G. Eleutheriades. "Overcoming the diffraction limit with a planar left-handed transmission-line lens". *Physical Review Letters*, 92(11):117403, 2004.

[42] J. B. Pendry, D. Schurig, and D. R. Smith. "Controlling electromagnetic fields". *Science*, 312(5781):1780–1782, 2006.

[43] C. M. Soukoulis and M. Wegener. "Past achievements and future challenges in the development of three-dimensional photonic metamaterials". *Nature Photonics*, 5:523–530, 2011.

[44] F. Capasso and N. Yu. "Flat optics with designer metasurfaces". *Nature Materials*, 13:139–150, 2014.

[45] V. M. Shalaev, W. Cai, U. K. Chettiar, H. Yuan, A. K. Sarychev, V. P. Drachev, and A. V. Kildishev. "Negative index of refraction in optical metamaterials". *Optics Letters*, 30(24):3356–3358, 2005.

[46] G. Dolling, C. Enkrich, M. Wegener, C. Soukoulis, and S. Linden. "Simultaneous negative phase and group velocity of light in a metamaterial". *Science*, 312(5775):892–894, 2006.

[47] J. Zhou, T. Koschny, M. Kafesaki, E. Economou, J. B. Pendry, and C. M. Soukoulis. "Saturation of the magnetic response of Split-Ring Resonators at optical frequencies". *Physical Review Letters*, 95(22):223902, 2005.

[48] V. M. Shalaev. "Optical negative-index metamaterials". *Nature Photonics*, 1:41–48, 2007.

[49] C. M. Soukoulis and M. Wegener. "Optical metamaterials: More bulky and less lossy". *Science*, 330(6011):1633–1634, 2010.

[50] A. V. Kildishev, A. Boltasseva, and V. M. Shalaev. "Planar photonics with metasurfaces". *Science*, 339(6125):1232009, 2013.

[51] A. V. Rogacheva, V. A. Fedotov, A. S. Schwanecke, and N. I. Zheludev. "Giant gyrotropy due to electromagnetic-field coupling in a bilayered chiral structure". *Physical Review Letters*, 97(17):177401, 2006.

[52] V. A. Fedotov, P. L. Mladyonov, S. L. Prosvirnin, A. V. Rogacheva, Y. Chen, and N. I. Zheludev. "Asymmetric propagation of electromagnetic waves through a planar chiral structure". *Physical Review Letters*, 97(16):167401, 2006.

[53] E. Plum, J. Zhou, J. Dong, V. A. Fedotov, T. Koschny, C. M. Soukoulis, and N. I. Zheludev. "Metamaterial with negative index due to chirality". *Physical Review B*, 79(3):035407, 2009.

[54] V. A. Fedotov, M. Rose, S. L. Prosvirnin, N. Papasimakis, and N. I. Zheludev. "Sharp trapped-mode resonances in planar metamaterials with a broken structural symmetry". *Physical Review Letters*, 99(14):147401, 2007.

[55] E. Plum, V. A. Fedotov, and N. I. Zheludev. "Extrinsic electromagnetic chirality in metamaterials". *Journal of Optics A*, 11(7):074009, 2009.

[56] E. Plum. "Extrinsic chirality: Tunable optically active reflectors and perfect absorbers". *Applied Physics Letters*, 108:241905, 2016.

[57] N. Papasimakis, V. A. Fedotov, N. I. Zheludev, and S. L. Prosvirnin. "Metamaterial analog of electromagnetically induced transparency". *Physical Review Letters*, 101(25):253903, 2008.

[58] W. Cao, R. Singh, C. Zhang, J. Han, M. Tonouchi, and W. Zhang. "Plasmon-induced transparency in metamaterials: Active near field coupling between bright superconducting and dark metallic mode resonators". *Applied Physics Letters*, 103:101106, 2013.

[59] N. I. Zheludev, S. L. Prosvirnin, N. Papasimakis, and V. A. Fedotov. "Lasing spaser". *Nature Photonics*, 2:351–354, 2008.

[60] R. Maas, J. Parsons, N. Engheta, and A. Polman. "Experimental realization of an epsilon-near-zero metamaterial at visible wavelengths". *Nature Photonics*, 7:907–912, 2013.

[61] N. Yu, P. Genevet, M. A. Kats, F. Aieta, J. P. Tetienne, F. Capasso, and Z. Gaburro. "Light propagation with phase discontinuities: generalized laws of reflection and refraction". *Science*, 334(6054):333–337, 2011.

[62] X. Ni, N. K. Emani, A. V. Kildishev, A. Boltasseva, and V. M. Shalaev. "Broadband light bending with plasmonic nanoantennas". *Science*, 335(6067):427, 2012.

[63] S. L. Sun, K. Y. Yang, C. M. Wang, T. K. Juan, W. T. Chen, C. Y. Liao, Q. He, S. Xiao, W. T. Kung, G. Y. Guo, L. Zhou, and D. P. Tsai. "High-efficiency broadband anomalous reflection by gradient meta-surfaces". *Nano Letters*, 12(12):6223–6229, 2012.

[64] A. Pors, O. Albrektsen, I. P. Radko, and S. I. Bozhevolnyi. "Gap plasmon-based metasurfaces for total control of reflected light". *Scientific Reports*, 3:2155, 2013.

[65] S. Sun, Q. He, S. Xiao, Q. Xu, X. Li, and L. Zhou. "Gradient-index meta-surfaces as a bridge linking propagating waves and surface waves". *Nature Materials*, 11:426–431, 2012.

[66] A. Pors, M. G. Nielsen, R. L. Eriksen, and S. I. Bozhevolnyi. "Broadband focusing flat mirrors based on plasmonic gradient metasurfaces". *Nano Letters*, 13(2):829–834, 2013.

[67] F. Aieta, P. Genevet, M. A. Kats, N. Yu, R. Blanchard, Z. Gaburro, and F. Capasso. "Aberration-free ultrathin flat lenses and axicons at telecom wavelengths based on plasmonic metasurfaces". *Nano Letters*, 12(9):4932–4936, 2012.

[68] S. Ishii, V. M. Shalaev, and A. V. Kildishev. "Holey-metal lenses: sieving single modes with proper phases". *Nano Letters*, 13(1):159–163, 2013.

[69] X. Ni, A. V. Kildishev, V. M. Shalaev, N. Antoniou, and F. Capasso. "Metasurface holograms for visible light". *Nature Communications*, 4:2807, 2013.

[70] D. Veksler, E. Maguid, N. Shitrit, D. Ozeri, and V. Kleiner. "Multiple wavefront shaping by metasurface based on mixed random antenna groups". *ACS Photonics*, 2(5):661–667, 2015.

[71] B. Walther, C. Helgert, C. Rockstuhl, F. Setzpfandt, and F. Eilenberger. "Spatial and spectral light shaping with metamaterials". *Advanced Materials*, 24(47):6300–6304, 2012.

[72] N. Lawrence, J. Trevino, and L. Dal Negro. "Aperiodic arrays of active nanopillars for radiation engineering". *Journal of Applied Physics*, 111:113101, 2012.

[73] V. A. Fedotov, P. L. Mladyonov, S. L. Prosvirnin, and N. I. Zheludev. "Planar electromagnetic metamaterial with a fish scale structure". *Physical Review E*, 72(5):056613, 2005.

[74] J. Zhao, C. Zhang, P. V. Braun, and H. Giessen. "Large-area low-cost plasmonic nanostructures in the NIR for Fano resonant sensing". *Advanced Materials*, 24(35):247–252, 2012.

[75] N. I. Landy, S. Sajuyigbe, J. J. Mock, D. R. Smith, and W. J. Padilla. "Perfect metamaterial absorber". *Physical Review Letters*, 100(20):207402, 2008.

[76] V. A. Fedotov, J. Wallauer, M. Walther, M. Perino, N. Papasimakis, and N. I. Zheludev. "Wavevector selective metasurfaces and tunnel vision filters". *Light: Science & Applications*, 4:e306, 2015.

[77] G. V. Naik, J. Kim, and A. Boltasseva. "Oxides and nitrides as alternative plasmonic materials in the optical range". *Optical Materials Express*, 1(6):1090–1099, 2011.

[78] G. V. Naik, J. Liu, A. V. Kildishev, V. M. Shalaev, and A. Boltasseva. "Demonstration of Al:ZnO as a plasmonic component for near-infrared metamaterials.". *Proceedings of the National Academy of Sciences of the United States of America*, 109(23):8834–8838, 2012.

[79] W. A. Murray and W. L. Barnes. "Plasmonic materials". *Advanced Materials*, 19(22):3771–3782, 2007.

[80] M.G. Blaber, M.D. Arnold, N. Harris, M.J. Ford, and M.B. Cortie. "Plasmon absorption in nanospheres: A comparison of sodium, potassium, aluminium, silver and gold". *Physica B: Condensed Matter*, 394(2):184–187, 2007.

[81] P. Cencillo-Abad, J.-Y. Ou, E. Plum, J. Valente, and N. I. Zheludev. "Random access actuation of nanowire grid metamaterial". *Nanotechnology*, 17(48):485206, 2016.

[82] Z. L. Samson, K. F. MacDonald, F. De Angelis, B. Gholipour, K. Knight, C. C. Huang, E. Di Fabrizio, and N. I. Hewak, D. W. Zheludev. "Metamaterial electro-optic switch of nanoscale thickness". *Applied Physics Letters*, 96:143105, 2010.

[83] A. Minovich, J. Farnell, D. N. Neshev, I. McKerracher, F. Karouta, J. Tian, D. A. Powell, I. V. Shadrivov, T. H. Hoe, C. Jagadish, and Y. S. Kivshar. "Liquid crystal based nonlinear fishnet metamaterials". *Applied Physics Letters*, 100:121113, 2012.

[84] Y. S. Kivshar and N. I. Zheludev. "From metamaterials to metadevices". *Nature Materials*, 11:917–924, 2012.

[85] J. Y. Ou, E. Plum, L. Jiang, and N. I. Zheludev. "Reconfigurable photonic metamaterials". *Nano Letters*, 11(5):2142–2144, 2011.

[86] I. M. Pryce, K. Aydin, Y. A. Kelaita, R. M. Briggs, and H. A. Atwater. "Highly strained compliant optical metamaterials with large frequency tunability". *Nano Letters*, 10(10):4222–4227, 2010.

[87] T. Hand and S. Cummer. "Characterization of tunable metamaterial elements using MEMS switches". *Antennas and Wireless Propagation Letters*, 6(11):401–404, 2007.

[88] B. Ozbey and O. Aktas. "Continuously tunable terahertz metamaterial employing magnetically actuated cantilevers". *Optics Express*, 19(7):5741–5752, 2011.

[89] J. Valente, J.-Y. Ou, E. Plum, I. J. Youngs, and N. I. Zheludev. "Reconfiguring photonic metamaterials with currents and magnetic fields". *Applied Physics Letters*, 106:111905, 2015.

[90] J. Valente, E. Plum, I. J. Youngs, and N. I. Zheludev. "Nano- and micro-auxetic plasmonic materials". *Advanced Materials*, 28(26):5176–5180, 2016.

[91] H.-T. Chen, W. J. Padilla, J. M. O. Zide, A. C. Gossard, A. J. Taylor, and R. D. Averitt. "Active Terahertz metamaterial devices". *Nature*, 444:597–600, 2006.

[92] E. Feigenbaum, K. Diest, and H. A. Atwater. "Unity-order index change in transparent conducting oxides at visible frequencies". *Nano Letters*, 10(6):2111–2116, 2010.

[93] M. Gil, C. Damm, A. Giere, M. Sazegar, J. Bonache, R. Jakoby, and F. Martin. "Electrically tunable split-ring resonators at microwave frequencies based on barium-strontium-titanate thick films". *Electronics Letters*, 45(8):417–418, 2009.

[94] N. Papasimakis, Z. Luo, Z. X. Shen, F. De Angelis, E. Di Fabrizio, A. E. Nikolaenko, and N. I. Zheludev. "Graphene in a photonic metamaterial". *Optics Express*, 18(8):8353–8359, 2010.

[95] H. Yan, X. Li, B. Chandra, G. Tulevski, Y. Wu, M. Freitag, W. Zhu, P. Avouris, and F. Xia. "Tunable infrared plasmonic devices using graphene/insulator stacks". *Nature Nanotechnology*, 7:330–334, 2012.

[96] M. Ricci, N. Orloff, and S. M. Anlage. "Superconducting metamaterials". *Applied Physics Letters*, 87:034102, 2005.

[97] F. Gmry, M. Solovyov, J. Souc, C. Navau, J. Prat-Camps, and A. Sanchez. "Experimental realization of a magnetic cloak". *Science*, 335(6075):1466–1468, 2012.

[98] T. Driscoll, S. Palit, M. M. Qazilbash, M. Brehm, F. Keilmann, B.-G. Chae, Su.-Ji. Yun, H.-T. Kim, S. Y. Cho, N. M. Jokerst, D. R. Smith, and D. N. Basov. "Dynamic tuning of an infrared hybrid-metamaterial resonance using vanadium dioxide". *Applied Physics Letters*, 93:024101, 2008.

[99] T. Driscoll, H.-T. Kim, B.-G. Chae, B.-Ju. Kim, Y.-W. Lee, N. M. Jokerst, S. Palit, D. R. Smith, M. Di Ventra, and D. N. Basov. "Memory metamaterials". *Science*, 325(5947):1518–1521, 2009.

[100] K. Appavoo and R. F. Haglund. "Detecting nanoscale size dependence in VO 2 phase transition using a Split-Ring Resonator metamaterial". *Nano Letters*, 11(3):1025–1031, 2011.

[101] A. Karvounis, B. Gholipour, K. F. MacDonald, and N. I. Zheludev. "All-dielectric phase-change reconfigurable metasurface". *Applied Physics Letters*, 109:051103, 2016.

[102] Q. Zhao, L. Kang, Bo. Du, Bo. Li, J. Zhou, H. Tang, X. Liang, and B. Zhang. "Electrically tunable negative permeability metamaterials based on nematic liquid crystals". *Applied Physics Letters*, 90:011112, 2007.

[103] M. L. Tseng, X. Fang, V. Savinov, P. C. Wu, J.-Y. Ou, N. I. Zheludev, and D. P. Tsai. "Coherent selection of invisible high-order electromagnetic excitations". *Scientific Reports*, 7:44488, 2017.

[104] J. Shi, X. Fang, E. T. F. Rogers, E. Plum, and K. F. MacDonald. "Coherent control of Snell's law at metasurfaces". *Optics Express*, 22(17):21051–21060, 2014.

[105] X. Fang, K. F. MacDonald, E. Plum, and N. I. Zheludev. "Coherent control of light-matter interactions in polarization standing waves". *Scientific Reports*, 6:31141, 2016.

[106] M. B. Pu, Q. Feng, M. Wang, C. G. Hu, C. Huang, X. Ma, Z. Zhao, C. Wang, and X. Luo. "Ultrathin broadband nearly perfect absorber with symmetrical coherent illumination". *Optics Express*, 20(3):2246–2254, 2012.

[107] T. Roger, S. Vezzoli, E. Bolduc, J. Valente, J. J. F. Heitz, J. Jeffers, C. Soci, J. Leach, C. Couteau, N. I. Zheludev, and D. Faccio. "Coherent perfect absorption

in deeply subwavelength films in the single-photon regime". *Nature Communications*, 6:7031, 2015.

[108] X. Fang, M. Lun Tseng, J.-Y. Ou, K. F. MacDonald, D. Ping Tsai, and N. I. Zheludev. "Ultrafast all-optical switching via coherent modulation of metamaterial absorption". *Applied Physics Letters*, 104:141102, 2014.

[109] V. Nalla, S. Vezzoli, J. Valente, S. Handong, and N. I. Zheludev. "100 THz optical switching with plasmonic metamaterial". *CLEO/Europe-EQEC, Munich, Germany*, 2015.

[110] R. W. Boyd. *Nonlinear Optics*. Academic Press, San Diego, California, USA, third edition edition, 2008.

[111] X. Fang, M. L. Tseng, and N. I. Tsai, D. P. Zheludev. "Coherent excitation-selective spectroscopy of multipole resonances". *Physical Review Applied*, 5(1):014010, 2016.

[112] S. A. Mousavi, E. Plum, J. Shi, and N. I. Zheludev. "Coherent control of birefringence and optical activity". *Applied Physics Letters*, 105:011906, 2014.

[113] S. A. Mousavi, E. Plum, J. Shi, and N. I. Zheludev. "Coherent control of optical polarization effects in metamaterials". *Scientific Reports*, 5:8977, 2015.

[114] Y. P. Svirko and N. I. Zheludev. *Polarization of light in nonlinear optics*. Wiley, Chichester, 1998.

[115] X. Fang, K. F. MacDonald, and N. I. Zheludev. "Controlling light with light using coherent metadevices: all-optical transistor, summator and invertor". *Light: Science & Applications*, 4:e292, 2015.

[116] S. Thongrattanasiri, F. H. L. Koppens, and F. J. García de Abajo. "Complete optical absorption in periodically patterned graphene". *Physical Review Letters*, 108(4):047401, 2012.

[117] C. Hagglund, S. P. Apell, and B. Kasemo. "Maximized optical absorption in ultrathin films and its application to plasmon-based two-dimensional photovoltaics". *Nano Letters*, 11(2):915–916, 2011.

[118] U. Fano. "Effects of configuration interaction on intensities and phase shifts". *Physical Review*, 124(6):1866–1878, 1961.

[119] S. Lyk'yanchuk, N. I. Zheludev, S. A. Maier, N. J. Halas, P. Nordlander, H. Giessen, and C. T. Chong. "The Fano resonance in plasmonic nanostructures and metamaterials". *Nature Materials*, 9:707–715, 2010.

[120] A. E. Miroshnichenko, S. Flach, and Y. S. Kivshar. "Fano resonances in nanoscale structures". *Reviews of Modern Physics*, 82(3):2257–2298, 2010.

[121] J. D. Jackson. *Classical Electrodynamics*. Wiley, New York, 1999.

[122] C. Rockstuhl, T. Zentgraf, T. P. Meyrath, H. Giessen, and F. Lederer. "Resonances in complementary metamaterials and nanoapertures". *Optics Express*, 16(3):2080–2090, 2008.

[123] V. A. Fedotov, N. Papasimakis, E. Plum, A. Bitzer, M. Walther, P. Kuo, D. P. Tsai, and N. I. Zheludev. "Spectral collapse in ensembles of metamolecules". *Physical Review Letters*, 104(22):223901, 2010.

[124] M. Papaioannou, E. Plum, J. Valente, E. T. F. Rogers, and N. I. Zheludev. "Two-dimensional control of light with light on metasurfaces". *Light: Science & Applications*, 5:e16070, 2016.

[125] M. Papaioannou, E. Plum, J. Valente, E. T. F. Rogers, and N. I. Zheludev. "All-optical multichannel logic based on coherent perfect absorption in a plasmonic metamaterial". *APL Photonics*, 1:090801, 2016.

[126] D. J. Richardson, J. M. Fini, and L. E. Nelson. "Space-division multiplexing in optical fibres". *Nature Photonics*, 7:354–362, 2013.

[127] P. J. Winzer. "Making spatial multiplexing a reality". *Nature Photonics*, 8:345–348, 2014.

[128] U. Leonhardt. "Optical conformal mapping". *Science*, 312(5781):1777–1780, 2006.

[129] D. Schurig, J. J. Mock, B. J. Justice, S. A. Cummer, J. B. Pendry, A. F. Starr, and D. R. Smith. "Metamaterial electromagnetic cloak at microwave frequencies". *Science*, 314(5801):977–980, 2006.

[130] W. S. Cai, U. K. Chettiar, A. V. Kildishev, and V. M. Shalaev. "Optical cloaking with metamaterials". *Nature Photonics*, 1:224–227, 2007.

[131] J. Valentine, J. Li, T. Zentgraf, G. Bartal, and X. Zhang. "An optical cloak made of dielectrics". *Nature Materials*, 8:568–571, 2009.

[132] A. Papakostas, A. Potts, D. M. Bagnall, S. L. Prosvirnin, and H. J. Coles. "Optical manifestations of planar chirality". *Physical Review Letters*, 90(10):107404, 2003.

[133] T. Roy, A. E. Nikolaenko, and E. T. F. Rogers. "A meta-diffraction-grating for visible light". *Journal of Optics*, 15:085101, 2013.

[134] X. J. Ni, S. Ishii, A. V. Kildishev, and V. M. Shalaev. "Ultra-thin, planar, Babinet-inverted plasmonic metalenses". *Light: Science & Applications*, 2:e72, 2013.

[135] D. M. Lin, P. Y. Fan, E. Hasman, and M. L. Brongersma. "Dielectric gradient metasurface optical elements". *Science*, 345(6194):298–302, 2014.

[136] U. Efron. *Spatial Light Modulator: Materials, Devices, and Applications.* CRC Press, 1994.

[137] G. Lazarev, A. Hermerschmidt, S. Krger, and S. Osten. *LCOS Spatial LIght Modulators: Trends and Applications, in Optical Imaging and Metrology: Advanced Technologies.* Wiley-VCH Verlag GmbH & Co. KGaA, Weinheim, Germany, 2012.

[138] H. Yu, J. Park, K. Lee, J. Yoon, and K. Kim. "Recent advances in wavefront shaping techniques for biomedical applications". *Current Applied Physics*, 15(5):632–641, 2015.

[139] P. Gunter. "Holography, coherent light amplification and optical phase conjugation with photorefractive materials". *Physics Reports*, 93(4):199–299, 1982.

[140] X. Xu, H. Liu, and L. V. Wang. "Time-reversed ultrasonically encoded optical focusing into scattering media". *Nature Photonics*, 5:154–157, 2011.

[141] G. Jenkins. "All optical logic gates". *US Patent 6,990,281*, 2006.

[142] L. B. Ceipidor, A. Bosco, and E. Fazio. "Logic Functions, Devices, and Circuits Based on Parametric Nonlinear Processes". *Journal of Lightwave Technology*, 26(3):373–378, 2008.

[143] P. Singh, D. Kr. Tripathi, S. Jaiswal, and H. K. Dixit. "All-optical logic gates: Designs, classification, and comparison". *Advances in Optical Technologies*, 2014:275083, 2014.

[144] C. Wang and Z. Li. "Ultracompact linear on-chip silicon optical logic gates with phase insensitivity". *EPL (Europhysics Letters)*, 103(6):64001, 2013.

[145] Y.-P. Yang, K.-C. Lin, I-C. Yang, K.-Y. Lee, Y.J. Lin, W.-Y. Lee, and Y.-T. Tsai. "All-optical photonic crystal AND gate with multiple operating wavelengths". *Optics Communications*, 297:165–168, 2013.

[146] Y. Fu, X. Hu, and Q. Gong. "Silicon photonic crystal all-optical logic gates". *Physics Letters A*, 377(3):329–333, 2013.

[147] K. Singh and G. Kaur. "Interferometric architectures based all-optical logic design methods and their implementations". *Optics & Laser Technology*, 69:122–132, 2015.

[148] Y. Fu, X. Hu, C. Lu, S. Yue, H. Yang, and Q. Gong. "All-optical logic gates based on nanoscale plasmonic slot waveguides". *Nano Letters*, 12(11):5784–5790, 2012.

[149] E. Knill, R. Laflamme, and G. J. Milburn. "A scheme for efficient quantum computation with linear optics". *Nature*, 409:46–52, 2001.

[150] J. P. Dowling. "Quantum optical metrology - the lowdown on high-N00N states". *Contemporary Physics*, 49(2):125–143, 2008.

[151] S. M. Barnett, J. Jeffers, A. Gatti, and R. Loudon. "Quantum optics of lossy beam splitters". *Physical Review A*, 57(3):2134–2145, 1998.

[152] T. Roger, S. Restuccia, A. Lyons, D. Giovannini, J. Romero, J. Jeffers, M. Padgett, and D. Faccio. "Coherent absorption of N00N states". *Physical Review Letters*, 117(2):023601, 2016.

[153] R.-J. Essiambre, R. Ryf, N. K. Fontaine, and S. Randel. "Breakthroughs in photonics 2012: Space-Division Multiplexing in multimode and multicore fibers for high-capacity optical communication". *IEEE Photonics Journal*, 5(2):0701307–0701307, 2013.

[154] T. Mizuno, H. Takara, K. Shibahara, A. Sano, and Y. Miyamoto. "Dense Space Division Multiplexed transmission over multicore and multimode fiber for long-haul transport systems". *Journal of Lightwave Technology*, 34(6):1484–1493, 2016.

[155] T. Hayashi, T. Taru, T. Nagashima, O. Shimakawa, T. Sasaki, and E. Sasaoka. "Multi-core fiber for high-capacity long-haul spatially-multiplexed transmission". *SEI Technical Review*, 77:14–22, 2013.

[156] J. Sakaguchi, Y. Awaji, N. Wada, A. Kanno, T. Kawanishi, T. Hayashi, T. Taru, T. Kobayashi, and M. Watanabe. "Space Division Multiplexed transmission of 109-Tb/s sata signals using homogeneous seven-core fiber". *Journal of Lightwave Technology*, 30(4):658–665, 2012.

[157] W. L. Chan, H.-T. Chen, A. J. Taylor, I. Brener, M. J. Cich, and D. M. Mittleman. "A spatial light modulator for terahertz beams". *Applied Physics Letters*, 94:213511, 2009.

[158] C. M. Watts, C. C. Nadell, J. Montoya, S. Krishna, and W. J. Padilla. "Frequency-division-multiplexed single-pixel imaging with metamaterials". *Optica*, 3(2):133–138, 2016.

[159] P. Cencillo-Abad, E. Plum, E. T. F. Rogers, and N. I. Zheludev. "Spatial optical phase-modulating metadevice with subwavelength pixelation". *Optics Express*, 24(16):18790–18798, 2016.

[160] Q. Wang, E. T. F. Rogers, B. Gholipour, C.-M. Wang, Gu. Yuan, J. Teng, and N. I. Zheludev. "Optically reconfigurable metasurfaces and photonic devices based on phase change materials". *Nature Photonics*, 10:60–65, 2015.

[161] W. Klaus, J. Sakaguchi, B. J. Puttnam, Y. Awaji, N. Wada, T. Kobayashi, and M. Watanabe. "Free-space coupling optics for multicore fibers". *IEEE Photonics Technology Letters*, 24(21):1902–1905, 2012.

[162] S. Gross, N. Riesen, J. D. Love, and M. J. Withford. "Three-dimensional ultra-broadband integrated tapered mode multiplexers". *Laser & Photonics Reviews*, 8(5):81–85, 2014.

[163] N. Riesen, S. Gross, J. D. Love, and M. J. Withford. "Femtosecond direct-written integrated mode couplers". *Optics Express*, 22(24):29855–29861, 2014.

[164] S. G. Leon-Saval, N. K. Fontaine, J. R. Salazar-Gil, B. Ercan, R. Ryf, and J. Bland-Hawthorn. "Mode-selective photonic lanterns for space-division multiplexing". *Optics Express*, 22(1):1036–1044, 2014.

[165] R. G. H. Van Uden, R. A. Correa, E. A. Lopez, F. M. Huijskens, C. Xia, G. Li, A. Schülzgen, H. De Waardt, A. M. J. Koonen, and C. M. Okonkwo. "Ultra-high-density spatial division multiplexing with a few-mode multicore fibre". *Nature Photonics*, 8:865–870, 2014.

[166] H. Chen, R. van Uden, C. Okonkwo, and T. Koonen. "Compact spatial multiplexers for mode division multiplexing". *Optics Express*, 22(26):31582–31594, 2014.

[167] M. Heinrich, S. Miri, M.-A.and Stützer, R. El-Ganainy, S. Nolte, A. Szameit, and D. N. Christodoulides. "Supersymmetric mode converters". *Nature Communications*, 5:3698, 2014.

[168] X. Zhang, W. Li, H. Hu, and N. K. Dutta. "High-speed all-optical encryption and decryption based on two-photon absorption in semiconductor optical amplifiers". *Journal of Optical Communications and Networking*, 7(4):276–285, 2015.

[169] W.-H. Chang, Gu.-C. Yang, C.-Yu. Chang, and W.C. Kwong. "Enhancing Optical-CDMA confidentiality with multicode-keying encryption". *Journal of Lightwave Technology*, 33(9):1708–1718, 2015.

[170] M. Papaioannou, E. Plum, and N. I. Zheludev. "All-Optical pattern recognition and image processing on a metamaterial beam splitter". *ACS Photonics*, 4(2):217–222, 2017.

[171] C. S. Yelleswarapu, S.-R. Kothapalli, and D.V.G.L.N. Rao. "Optical Fourier techniques for medical image processing and phase contrast imaging". *Optics Communications*, 281(7):1876–1888, 2008.

[172] B. L. Volodin, B. Kippelen, K. Meerholz, B. Javidi, and N. Peyghambarian. "A polymeric optical pattern-recognition system for security verification". *Nature*, 383:58–60, 1996.

[173] X. Yang, C. Wu, and W. Hu. "High-speed optical binary data pattern recognition for network security applications". *Frontiers of Optoelectronics*, 5(3):271–278, 2012.

[174] P. Boffi, D. Piccinin, M. C. Ubaldi, and M. Martinelli. "All-optical pattern recognition for digital real-time information processing". *Applied Optics*, 42(23):4670–4680, 2003.

[175] D. Ishikawa, A. Okamoto, S. Honma, T. Ito, K. Shimayabu, and K. Sato. "All-optical multifunctional logic gates for image information using photorefractive two-wave mixing". *Optical Review*, 14(4):246–251, 2007.

[176] J. B. Norman. "Phase conjugate Michelson Intereferometers for all-optical image processing and computing". *American Journal of Physics*, 60:212, 1992.

[177] P. Scotto, P. Colet, and M. San Miguel. "All-optical image processing with cavity type II second-harmonic generation". *Optics Letters*, 28(18):1695–1697, 2003.

[178] I. Biaggio, J. P. Partanen, B. Ai, R. J. Knize, and R. W. Hellwarth. "Optical image processing by an atomic vapour". *Nature*, 371:318–320, 1994.

[179] S. H. Kim, K. Goda, A. Fard, and B. Jalali. "Optical time-domain analog pattern correlator for high-speed real-time image recognition". *Optics Letters*, 36(2):220–222, 2011.

[180] C. Mesaritakis, A. Bogris, A. Kapsalis, and D. Syvridis. "High-speed all-optical pattern recognition of dispersive Fourier images through a photonic reservoir computing subsystem.". *Optics Letters*, 40(14):3416–3419, 2015.

[181] A. Silva, F. Monticone, G. Castaldi, V. Galdi, A. Alu, and N. Engheta. "Performing mathematical operations with metamaterials". *Science*, 343(6167):160–163, 2014.

[182] G. Lipworth, A. Mrozack, J. Hunt, Da. L. Marks, T. Driscoll, D. Brady, and D. R. Smith. "Metamaterial apertures for coherent computational imaging on the physical layer". *JOSA A*, 30(8):1603–1612, 2013.

[183] M. Molerón and C. Daraio. "Acoustic metamaterial for subwavelength edge detection". *Nature Communications, Published online: 25 August 2015; — doi:10.1038/ncomms9037*, 6:8037, 2015.

[184] A. Arbabi, E. Arbabi, S. M. Kamali, Y. Horie, S. Han, and A. Faraon. "Miniature optical planar camera based on a wide-angle metasurface doublet corrected for monochromatic aberrations". *Nature Communications*, 7:13682, 2016.

[185] C. M. Watts, D. Shrekenhamer, J. Montoya, G. Lipworth, T. Hunt, J.and Sleasman, S. Krishna, D. R. Smith, and W. J. Padilla. "Terahertz compressive imaging with metamaterial spatial light modulators". *Nature Photonics*, 8:605–609, 2014.

[186] National Snow and Ice Data Center (USA), http://nsidc.org/.

[187] E. Born and E. Wolf. *Principles of Optics.* Cambridge University Press, 1999.

[188] G. Ulf. *Probability and Statistics: The Harald Cramer Volume.* Wiley, 1959.

[189] M. Papaioannou, E. Plum, E. T. F. Rogers, and N. I. Zheludev. "All-optical dynamic focusing of light via coherent absorption in a plasmonic metasurface". *Light: Science & Applications*, In Press.

[190] S. Ray. *Applied Photographic Optics: Lenses and Optical Systems for Photography, Film, Video and Digital Imaging.* Focal Press, 3rd edition, 2002.

[191] H.-S. Ee and R. Agarwal. "Tunable metasurface and flat optical zoom lens on a stretchable substrate". *Nano Letters*, 16(4):2818–2823, 2016.

[192] N. Chronis, G. L. Liu, K.-H. Jeong, and L. P. Lee. "Tunable liquid-filled microlens array integrated with microfluidic network". *Optics Express*, 11(19):2370–2378, 2003.

[193] J. Chen, W. Wang, J. Fang, and K. Varahramyan. "Variable-focusing microlens with microfluidic chip". *Journal of Micromechanical Microengineering*, 14(5):675, 2004.

[194] H.-C. Yeh, Y.-C. Kuo, S.-H. Lin, J.-D. Lin, T.-S. Mo, and S.-Y. Huang. "Optically controllable and focus-tunable Fresnel lens in azo-dye-doped liquid crystals using a Sagnac interferometer". *Optics Letters*, 36(8):1311–1313, 2011.

[195] V. Nikolenko, B. O. Watson, R. Araya, A. Woodruff, D. S. Peterka, and R. Yuste. "SLM microscopy: scanless two-photon imaging and photostimulation with spatial light modulators". *Frontiers of Neural Circuits*, 2:5, 2008.

[196] C. Maurer, A. Jesacher, S. Bernet, and M. Ritsch-Marte. "What spatial light modulators can do for optical microscopy". *Laser & Photonics Reviews*, 5(1):81–101, 2010.

[197] P. L. Kelley. "Self-focusing of optical beams". *Physical Review Letters*, 15(26):1005, 1965.

[198] P. Lallemand and N. Bloembergen. "Self-focusing of laser beams and stimulated Raman gain in liquids". *Physical Review Letters*, 15(26):1010–1012, 1965.

[199] C. E. Max, J. Arons, and A. B. Langdon. "Self-modulation and self-focusing of electromagnetic waves in plasmas". *Physical Review Letters*, 33(4):209–212, 1974.

[200] I. V. Minin and O. V. Minin. "Reference phase in diffractive lens antennas: A review". *Journal of Infrared, Millimeter, and Terahertz Waves*, 32(6):801–822, 2011.

[201] O. K. Esroy. *Diffraction, Fourier optics and imaging.* John Wiley & Sons, 2006.

[202] J. W. Goodman. *Introduction to Fourier Optics.* Roberts and Company Publishers, 3rd edition, 2016.

[203] J. E. Greivenkamp. *Field Guide to Geometrical Optics.* SPIE Press, Bellingham, WA, 2004.

[204] E. T. F. Rogers, S. Savo, J. Lindberg, T. Roy, M. R. Dennis, and N. I. Zheludev. "Super-oscillatory optical needle". *Applied Physics Letters*, 102:031108, 2013.

[205] J. Durnin, J. J. Miceli Jr., and J. H. Eberly. "Diffraction-free beams". *Physical Review Letters*, 58(15):1499–1501, 1987.

[206] T. Čižmár and K. Dholakia. "Tunable Bessel light modes: engineering the axial propagation". *Optics Express*, 17(18):15558–15570, 2009.

[207] C. Altuzarra, S. Vezzoli, J. Valente, W. Gao, D. Soci, C.and Faccio, and C. Couteau. "Nonlocal control of dissipation with entangled photons". *arxiv [physics.optics]*, 701.05357, 2017.

[208] E. Plum. *Chirality and Metamaterials.* PhD thesis, University of Southampton, 2010.